The Pennsylvania State University
The Graduate School

EXAMINING CORRELATIONS BETWEEN PLANETARY AND STELLAR PROPERTIES USING A BAYESIAN FRAMEWORK

A Dissertation in
Astronomy & Astrophysics
by
Emily Safsten

Submitted in Partial Fulfillment
of the Requirements
for the Degree of

Doctor of Philosophy

August 2023

The dissertation of Emily Safsten was reviewed and approved by the following:

Rebekah Dawson
Associate Professor of Astronomy & Astrophysics
Dissertation Advisor, Chair of Committee, Graduate Program Head

Jason Wright
Professor of Astronomy & Astrophysics

Eric B. Ford
Distinguished Professor of Astronomy & Astrophysics

Robin Ciardullo
Professor of Astronomy & Astrophysics

G. Jogesh Babu
Distinguished Professor of Statistics

Abstract

The thousands of exoplanets discovered to date have revealed a variety of worlds and orbital architectures. Observed correlations of planetary properties with other stellar or planetary parameters can offer clues about planets' origins and evolution. However, it can be difficult to distinguish the true underlying cause of an observed trend because stellar parameters are often interrelated. In particular, it is often unknown whether a planetary property is due to the age of the system – meaning it evolves over time – or other parameters that may be related to the age – meaning it is determined by formation conditions. Additionally, small sample sizes and large measurement uncertainties can cast doubt on whether a supposed trend actually exists.

To address this problem, we develop a Bayesian statistical framework that uses odds ratios to compare hypotheses for the source of an observed trend of a planetary property. We define three types of hypotheses: Nurture, in which the property is due to the system age; Nature, in which the property is due to some other observed system parameter; and Chance, in which the property is unrelated to any observed parameters. We apply this framework to the proposed age trends of 2:1 orbital resonances, stellar obliquities of hot Jupiter hosts, and eccentricities of hot Jupiters. We find that stellar obliquities of stars with hot Jupiters are most likely driven by stellar temperature, not age. We find that the data very strongly support a trend of hot Jupiter orbital eccentricities due to stellar age over a trend due to semimajor axis. We do not find enough evidence to support that 2:1 orbital resonances are disrupted over time.

We next examine the impact on our results of formally incorporating measurement uncertainties. In each case we analyze, while uncertainties do affect the numerical value of the odds ratio, our overall conclusions remain the same. We also use updated samples for the 2:1 resonances and stellar obliquities cases and again find our conclusions unchanged. Through simulated 2:1 resonance data, we show that sample size may be more important than measurement precision for drawing a firm conclusion in this case.

Finally, we apply our framework to the small planet radius valley. The most favored theories for the formation of the valley are core-powered mass loss and photoevaporation. We compare these hypotheses using the data from the California-*Kepler* Survey (CKS) and data from the *Gaia-Kepler-TESS*-Host Stellar Properties (GKTH) catalog. The results from the CKS data depend on the assumptions regarding core mass and initial atmospheric mass fraction, but strongly favor core-powered mass loss when we follow the respective prescriptions from studies on each process. The GKTH data strongly support core-powered mass loss regardless of these assumptions. We do see a dependence of our results on period and stellar temperature, which we will investigate further in the future.

Table of Contents

List of Figures

List of Tables

Acknowledgments

First and foremost, I must thank and acknowledge my advisor, Rebekah Dawson. Her patience, flexibility, expertise, and helpful advice – both in terms of research and professional development – have been most valuable. Thanks also to the other professors, researchers, and fellow graduate students that have supported, assisted, and accommodated me in various ways, including, but not limited to, Sarah Morrison, Angie Wolfgang, Randy McEntaffer, Don Schneider, Mike Eracleous, and the other members of my committee.

This thesis would not have happened without the support of Penn State's Math department, for which I am grateful. In particular, it was the persuasion and negotiating of Dr. Svetlana Katok, who wanted my husband to come to Penn State, that moved me from the waitlist to being admitted to the astronomy PhD program.

Finally, I am grateful to my husband for his support, and to him, wonderful daycare workers, and friends for helping take care of our kids.

This work has been supported by federal funding as indicated in the acknowledgments of each main chapter. The findings and conclusions of this work do not necessarily reflect the views of the funding agencies.

Chapter 1
Introduction

1.1 A Wide Variety of Planets

The census of planets known to orbit stars other than the Sun now numbers in the thousands. These discoveries have greatly expanded our understanding of what sorts of planets and orbital configurations can exist, because most of them do not have a close analogue in our solar system. There are planets that travel on orbits that are highly eccentric or highly tilted. Giant gaseous worlds, once thought to only exist far enough from a star where water can freeze into ice, whirl around their stars in a matter of days. And there is a large population of exoplanets with sizes between Earth and Neptune, bridging the gap between the seemingly distinct classes of small, rocky worlds and large, gaseous worlds found in the solar system.

We now face the challenge of explaining how these planetary systems came to be. In many cases, individual systems can be studied in great detail. But we lack the resources to do this for every single planet. Additionally, many systems are too difficult to perform detailed characterization on with our current level of technology. But with such a large sample size, we can study the population of planets as a whole and uncover statistical trends that offer clues about planetary formation and evolution.

One useful avenue is studying how planetary properties change with age. The lifetimes of planetary systems and most of the timescales over which they evolve are orders of magnitude longer than the length of time we have been able to observe them. But a population of planets around stars with a range of ages shows planetary systems at different stages of evolution. Trends of planetary properties with stellar age suggest that those properties change over time, and the timescales over which they evolve are important for understanding what processes may be driving the evolution. Interpreting such proposed trends can be tricky, however, because stellar age is related to other stellar

parameters (for example, higher-mass stars have shorter lifetimes, and stars change temperature as they age). Additionally, age measurements often have large uncertainties, which can leave doubt about whether a trend truly exists, especially in a small sample.

In this work, we examine several proposed trends of planetary properties with stellar age. These include 2:1 orbital resonances of pairs of planets, in which one planet has twice the orbital period of the other. Various dynamical processes, acting on different timescales, could potentially disrupt such resonances, but it is unknown how prevalent such processes are and thus how long resonances persist. Understanding how the occurrence of 2:1 resonances changes with age could shed some light on this question. We also look at stellar obliquities, or the spin-orbit misalignments, of stars hosting hot Jupiters. Some stars are greatly misaligned compared to their planet's orbit, and it is not fully understood what causes the alignment in the first place or what may cause the star to realign (see the review by Albrecht et al. 2022). Observed relationships between stellar obliquities and age or other properties offer clues about the dominant mechanisms at work.

Another trend is that of the orbital eccentricities of hot Jupiters, which have been observed to decrease with stellar age. This suggests that these planets are undergoing tidal circularization. A Jupiter-size planet can form far away from its star, then, through some gravitational interaction with another massive object, be sent inward on a highly eccentric orbit that takes it very close to its star. Over time, tidal interactions between the star and the planet can dampen the eccentricity, until the planet is left in a tight circular orbit as a hot Jupiter. A trend of decreasing eccentricity with age would support this scenario for the formation of hot Jupiters (see Dawson & Johnson 2018 for a review).

Among the unexpected finds from the *Kepler* mission is the large population of super-Earths and sub-Neptunes, a type of planet not seen in our own solar system. These planets have a bimodal radius distribution, with a gap around $\sim$1.5-2 $R_\oplus$ (e.g. Fulton et al. 2017), which is thought to separate rocky super-Earths from gaseous sub-Neptunes. Popular theories for the formation of this gap involve the loss of sub-Neptune atmospheres, turning them into super-Earths over time. The ratio of super-Earths to sub-Neptunes has been observed to increase with age (Berger et al., 2020a; Sandoval et al., 2021), supporting the idea that some mass-loss mechanism is at work, but it is not known which one is the most likely sculptor of the radius valley.

1.1.1 Planet Discovery Techniques

Although the very first exoplanets were found via pulsar timing (Wolszczan & Frail, 1992), radial velocity was the dominant exoplanet discovery method until the *Kepler*

mission. Radial velocity works by observing the Doppler shift of a star's spectral lines, caused by the gravitational tug of a planet on the star as it orbits, which causes the star to move back and forth. The signal is strongest for massive planets close to their stars, so many of the first exoplanets found were hot Jupiters (such as 51 Pegasi b, the first exoplanet found around a Sun-like star; Mayor & Queloz 1995). The improvements in instrumentation and data processing over the subsequent decades have pushed the limits of observable exoplanets to lower and lower masses.

After the launch of the *Kepler* space telescope (Borucki et al., 2010), transit photometry quickly became the most prolific exoplanet discovery technique. This method works by monitoring a star's brightness over time and looking for a small, periodic decrease in luminosity that could be caused by a planet passing in front of the star and blocking a small amount of its light. Staring at the same patch of sky for four years, *Kepler* provided long-baseline photometry for stars in its field of view that yielded thousands of exoplanet candidates. Even after the failure of reaction wheels that were responsible for keeping the spacecraft pointed correctly, *Kepler* was still used to hunt for planets in other parts of the sky. The candidates, once identified, need to be followed up with additional observations to rule out false positive signals (such as an eclipsing binary that happens to be right behind the target star, such that the luminosity of the target dilutes the eclipse signal and makes it look more planet-like). This work has led to the discovery and confirmation of thousands of exoplanets, from Jupiter-size to Earth-like. Most of the planets we use in this thesis were discovered by *Kepler*.

Other discovery techniques exist, such as microlensing, direct imaging, and astrometry, and each is valuable in its own right. But so far, transit photometry and radial velocity have provided the bulk of the exoplanet sample.

One important point to note is that in the vast majority of cases, we do not observe an exoplanet directly. Rather, we observe the planet's effect on its host star. This means that, to a large extent, the degree to which we can characterize a planet depends on the degree to which we can characterize its star. For example, the ratio of the planet's radius to the star's radius is easily determined by measuring the depth of a transit. But unless the actual radius for the star is known, all we have is a relative radius for the planet.

1.2 Stellar Ages

One significant hurdle to understanding planetary evolution is measuring the ages of their stars. This is a historically difficult task that has been aided in recent years by

surveys such as *Gaia* that provide precise stellar parameters. We describe a couple of the most-used methods here, which were used to derive the majority of the ages in the samples we use.

One of the most common methods of determining stellar ages is the use of isochrones. From Greek words meaning "same" and "time", isochrones show positions on an H-R diagram of stars of the same age. An equivalent approach is evolutionary tracks, which track a star's journey across the H-R diagram throughout its life. With measurements of a star's temperature and intrinsic luminosity, the isochrone closest to the star's position on the H-R diagram can be found and thus the star's age determined.

However, it can be difficult to do this with sufficient precision because a star's position on the H-R diagram does not change much during its main-sequence life (which, for most stars, lasts billions of years). This means most isochrones are very close together, especially for very young main-sequence stars (Soderblom, 2010). The typical measurement uncertainties in stellar temperature and luminosity thus translate to large uncertainties in stellar age. Several earlier studies found it difficult to determine ages to better than 20-50% (e.g. Pont & Eyer 2004; Jørgensen & Lindegren 2005; Takeda et al. 2007; see Soderblom 2010 for a review).

The use of isochrones has been greatly aided in recent years by data from the *Gaia* spacecraft. *Gaia* has measured precise parallaxes for thousands of stars. With the precise distances derived from those parallaxes, precise intrinsic luminosities can be found. Surveys such as Fulton & Petigura (2018) and Berger et al. (2018, 2020b, 2023a) have made use of this data to determine homogeneous ages and other properties for hundreds of stars.

Another common method for finding stellar ages that is more suited to younger stars is measuring activity levels. Younger stars are more active in various non-thermal emission processes across a range of wavelengths due to their stronger magnetic fields (Soderblom, 2010). A widely-used measure is the ratios of the calcium II H and K lines. Absorption of these lines occurs in the photosphere, while the chromosphere of an active star produces noticeable emission in these lines, and what is measured is the ratio of the line flux to the star's bolometric luminosity (Soderblom, 2010). This quantity can then be related to the age (e.g. Mamajek & Hillenbrand 2008).

1.3 Statistical Background

Here, we give an overview of some basic statistical concepts relevant to later chapters.

1.3.1 Probability Basics

The probability of an event A occurring is expressed as $p(A)$. The joint probability of two events A and B is $p(A \cap B)$ and represents the likelihood that both events occur. Sometimes, A and B are independent of each other, and the joint probability is simply the product of their individual probabilities: $p(A \cap B) = p(A)p(B)$. A classic example is flipping a coin. A fair coin has a 50% chance of landing heads-up and a 50% chance of landing tails-up, so $p(heads) = 0.5$ and $p(tails) = 0.5$. If the coin is flipped two times, the probability of getting heads first and tails second is $p(first = heads \cap second = tails) = p(heads)p(tails) = 0.5 \times 0.5 = 0.25$, because the outcome of the first flip has no influence on the outcome of the second flip; the two events are independent.

In other cases, A and B are not independent. If the probability of event A depends on event B occurring, we can express the joint probability of A and B as a conditional probability:

$$p(A \cap B) = p(A|B)p(B). \tag{1.1}$$

In this equation, the | means "given", so the term $p(A|B)$ can be read as "the probability of A, given B." As an example, consider a bag with three red marbles and three purple marbles. If you reach in (without looking) and pick one at random, there would be a 50% chance of picking a red marble and a 50% chance of picking a purple marble. Now say you pick a second marble, without putting the first back in the bag. If the first marble was purple, what is the likelihood that the second marble is red? With five marbles left in the bag and three of them red, the probability that the second marble is red is 3/5. We can then express the joint probability of selecting one purple marble and then one red marble as follows:

$$\begin{aligned} p(first = purple \cap second = red) &= p(red|purple)p(purple) \\ &= 0.6 \times 0.5 \\ &= 0.3. \end{aligned} \tag{1.2}$$

To get the overall probability of A when A is dependent on B, we must marginalize over B. This means to integrate $p(A, B)$ over all values of B, as follows:

$$\begin{aligned} p(A) &= \int p(A \cap B)dB \\ &= \int p(A|B)p(B)dB. \end{aligned} \tag{1.3}$$

This integral becomes a sum if B can only take on discrete values, such as 0 and 1:

$$p(A) = p(A|B=0)p(B=0) + p(A|B=1)p(B=1). \tag{1.4}$$

In the marble example, consider the overall probability of getting a red marble on the second draw, regardless of the color of the first marble. We need to consider the probabilities that the second marble is red if the first marble is purple, and that the second marble is red if the first marble is red:

$$\begin{aligned} p(second = red) &= p(second = red|first = purple)p(first = purple) \\ &\quad + p(second = red|first = red)p(first = red) \\ &= (0.6 \times 0.5) + (0.4 \times 0.5) \\ &= 0.3 + 0.2 = 0.5. \end{aligned} \tag{1.5}$$

1.3.2 Bayes' Theorem

Bayes' theorem is derived from the definition of conditional probability:

$$\begin{aligned} p(A \cap B) &= p(A|B)p(B) = p(B|A)p(A) \\ p(A|B) &= \frac{p(B|A)p(A)}{p(B)}. \end{aligned} \tag{1.6}$$

It is typically applied when assessing the suitability of a model to a set of data. If we call the set of data D and the proposed model M, we can rewrite Eqn. 1.6 as

$$p(M|D) = \frac{p(D|M)p(M)}{p(D)}. \tag{1.7}$$

The term $p(M|D)$ is the probability of the model given the data and is called the posterior. It represents the degree to which we believe the model to be a good representation of the data. This interpretation is distinct from a frequentist approach, which looks at the frequency with which an event occurs over many trials. The term $p(D|M)$ is the likelihood, the probability of the observed data existing or occurring under the proposed model. The term $p(M)$ is called the prior on M. It represents how much we believe a model to be true before performing any analysis. If a given model provides a good fit to the data, then the likelihood $p(D|M)$ will be high compared to the likelihood for a model that provides a poor fit. But if the model itself does not seem very plausible –

for example, it could have variables that need to be very finely-tuned or precise for the model to work – then we can assign it a low prior $p(M)$. This acts as a penalty on the likelihood to reduce the overall probability of the model in the posterior. Finally, $p(D)$ is the called the evidence. In practice, it can be difficult to calculate. However, some applications of Bayes' theorem, such as odds ratios and Markhov Chain Monte Carlo algorithms, look at the ratio of the posteriors for competing models, so $p(D)$ cancels out.

1.4 Outline of Dissertation

In Chapter 2, we develop a framework based on Bayes' theorem in order to assess observed correlations between planetary properties and stellar properties. The aim is to be able to understand the true, underlying source of an observed trend. We then apply this framework to the cases of 2:1 orbital resonances, stellar obliquities of stars with hot Jupiters, and eccentricities of hot Jupiters. In Chapter 3, we improve upon this framework by formally incorporating measurement uncertainties. We then reanalyze the same cases we look at in Chapter 2 to see how accounting for measurement uncertainties affects the results, and also apply the improved framework to updated samples for 2:1 resonances and stellar obliquities. In the case of 2:1 resonances, we always get inconclusive results, so we also explore why this may be and what we would need to detect an age trend, if such a trend exists. Finally, we use our framework in Chapter 4 to investigate which of two mechanisms – photoevaporation and core-powered mass loss – is more likely to be the primary sculptor of the radius valley in the sub-Neptunes and super-Earths. We conclude in Chapter 5.

Chapter 2
Nature vs. nurture: a Bayesian framework for assessing apparent correlations between planetary orbital properties and stellar ages

The text in this chapter is slightly modified from E. D. Safsten, R. I. Dawson, and A. Wolfgang, 2020, AJ, 160, 5. I developed the framework and performed the calculations described in this work and wrote the manuscript. R. I. Dawson advised on the project. R. I. Dawson and A. Wolfgang provided significant comments that were incorporated into the paper.

Many exoplanets have orbital characteristics quite different from those seen in our own solar system, including planets locked in orbital resonances and planets on orbits that are elliptical or highly inclined from their host star's spin axis. It is debated whether the wide variety in system architecture is primarily due to differences in formation conditions (nature) or due to evolution over time (nurture). Identifying trends between planetary and stellar properties, including stellar age, can help distinguish between these competing theories and offer insights as to how planets form and evolve. However, it can be challenging to determine whether observed trends between planetary properties and stellar age are driven by the age of the system – pointing to evolution over time being an important factor – or other parameters to which the age may be related, such as stellar mass or stellar temperature. The situation is complicated further by the possibilities of selection biases, small number statistics, uncertainties in stellar age, and orbital

evolution timescales that are typically much shorter than the range of observed ages. Here we develop a Bayesian statistical framework to assess the robustness of such observed correlations and to determine whether they are indeed due to evolutionary processes, are more likely to reflect different formation scenarios, or are merely coincidental. We apply this framework to reported trends between stellar age and 2:1 orbital resonances, spin-orbit misalignments, and hot Jupiters' orbital eccentricities. We find strong support for the nurture hypothesis only in the final case.

2.1 Introduction

Many exoplanets have orbital characteristics quite different from those seen in our own solar system, including planets locked in orbital resonances, planets on orbits that are elliptical or highly inclined from their host star's spin axis, planets parked close to their stars, and compact multi-planet systems (see Winn & Fabrycky 2015 and references therein). It is debated whether the wide variation in system architecture is primarily due to differences in formation conditions (nature) or due to evolution over time (nurture). Identifying trends between planetary and stellar properties, including stellar age (see, e.g., Christiansen et al. 2019b), can help distinguish between these competing theories and offer insights as to how planets form and evolve. As our sample of known exoplanets have grown, some apparent correlations between planetary orbital properties and stellar age have started to emerge. However, we face two major problems in interpreting such correlations.

First, the true underlying source of such correlations can be unclear because stellar age is interrelated with other stellar properties. For example, Winn et al. (2010) found that hot Jupiters orbiting stars warmer than 6250 K are preferentially misaligned with their host star's spin axis, compared to those orbiting cooler stars. However, Triaud (2011) argued that the trend with temperature noted by Winn et al. (2010) could instead be a trend with stellar age. The difficulty in distinguishing between nature vs. nurture is complicated further by the possibilities of selection biases, small number statistics, and uncertainties in stellar age (e.g., Mamajek & Hillenbrand 2008; Skumanich 1972).

Second, orbital evolution timescales tend to be strongly dependent on system properties such as semimajor axis, meaning that the distribution of such timescales can easily span many orders of magnitude (e.g., Dawson & Johnson 2018; Socrates et al. 2012; Winn et al. 2010). Therefore a typical observed sample of main sequence stars typically probes only a sliver of orbital evolution timescales – those which are comparable to the

stellar ages in the sample – casting suspicion on the nurture hypothesis as the explanation for an observed correlation. For example, Koriski & Zucker (2011) reported that systems with 2:1 period commensurabilities are younger than those without, suggesting that some 2:1 resonances are eventually disrupted. However, Dong & Dawson (2016) argued that the fine tuning of the disruption timescale necessary to account for the trend suggests that the difference in ages could be due to chance. In another case, Quinn et al. (2014) found evidence that hot Jupiters younger than their circularization timescales are more eccentric than ones older than their circularization timescales, which supports high-eccentricity migration as the primary hot Jupiter formation mechanism. However, the strong dependence of circularization timescale on semimajor axis, combined with the relatively small age range, raises the possibility that the eccentricity may primarily depend on semimajor axis rather than age.

Despite these challenges, disentangling the underlying sources of proposed trends is essential for understanding how these planetary properties came to be. Furthermore, as a larger sample of planets with well-characterized stellar hosts becomes available with data from *Gaia*, *TESS*, and *PLATO* (e.g., Veras et al. 2015), being able to distinguish the true driving factor will be essential for interpreting the data.

To address this problem, we develop a Bayesian statistical framework to assess the robustness of observed correlations of planetary properties with age. We define three hypotheses that represent possible sources for a correlation:

1. Nurture: The planetary property is due to the age of the system.

2. Nature: The planetary property is due to an observed system parameter other than age, but which may be connected to the age.

3. Chance: The planetary property is independent of observed system parameters, and any apparent correlation between them is merely a coincidence.

Here we lay out an approach for testing relative strengths of these three hypotheses using the available data and apply the approach to several reported trends. In the next section, we derive general equations for comparing the three hypotheses. We then apply our approach to reported trends with stellar age for 2:1 orbital resonances (Section 2.3), stellar obliquities (Section 2.4), and hot Jupiter eccentricities (Section 2.5). We end in Section 2.6 with our conclusions and a brief discussion of future work.

2.2 Generalized Hypotheses

Here we present a general framework for comparing Nurture, Nature, and Chance. To compare the strengths of two hypotheses, we need to compute their odds ratio. The odds ratio for two hypotheses of interest, $H_{\rm A}$ and $H_{\rm B}$, as explanations for an observed correlation between a planetary property and stellar age is:

$$\frac{p(H_{\rm A}|\{X_{\rm p,i}, t_{\star,{\rm i}}, \mathbf{X}_{\rm ob,i}\})}{p(H_{\rm B}|\{X_{\rm p,i}, t_{\star,{\rm i}}, \mathbf{X}_{\rm ob,i}\})} = \frac{\int[\prod_{\rm i} p(X_{\rm p,i}, t_{\star,{\rm i}}, \mathbf{X}_{\rm ob,i}|\mathbf{Y}, H_{\rm A})]p(\mathbf{Y})d\mathbf{Y}}{\int[\prod_{\rm i} p(X_{\rm p,i}, t_{\star,{\rm i}}, \mathbf{X}_{\rm ob,i}|\mathbf{Y}, H_{\rm B})]p(\mathbf{Y})d\mathbf{Y}} \frac{p(H_{\rm A})}{p(H_{\rm B})} \tag{2.1}$$

where $X_{\rm p}$ is the observed property of interest of the planet, $t_\star$ is the age of the star, and $\mathbf{X}_{\rm ob}$ contains other observed system quantities relevant to the problem (e.g., stellar mass, stellar temperature, planetary semimajor axis). $\{X_{\rm p,i}, t_{\star,{\rm i}}, \mathbf{X}_{\rm ob,i}\}$ represents the set of observed properties for a collection of planetary systems and their host stars, with the i subscript denoting an individual planet, star, or system. $\mathbf{Y}$ represents hyperparameters, population-wide variables that describe the distributions from which the individual system properties are drawn; these hyperparameters are marginalized over outside the product of individual system likelihoods. We give equal weight to each hypothesis a priori, so $p(H_{\rm A})/p(H_{\rm B}) = 1$. For each system and each hypothesis, we need to find $p(X_{\rm p,i}, t_{\star,{\rm i}}, \mathbf{X}_{\rm ob,i}|\mathbf{Y})$, the probability of a system existing with a certain configuration given the hyperparameter(s).

In general, $t_\star$, $X_{\rm p}$, and other relevant data may depend on stellar and planetary properties that have not been observed and that will thus need to be marginalized over. We lump these into a vector of non-observed quantities $\mathbf{X}_{\rm nob}$. Additionally, from here on out, we do not explicitly indicate the dependence on a particular hypothesis with $|H$ in the equations, and we omit the i subscript, with the understanding that all variables except $\mathbf{Y}$ denote individual system, planet, or stellar properties. The following equation is the general form of the likelihood from which we derive equations for each hypothesis (Sections 2.2.2, 2.2.3, and 2.2.4) and, later, each specific application (Sections 2.3, 2.4, and 2.5):

$$p(X_{\rm p}, t_\star, \mathbf{X}_{\rm ob}|\mathbf{Y}) = \int p(X_{\rm p}, t_\star, \mathbf{X}_{\rm ob}, \mathbf{X}_{\rm nob}|\mathbf{Y})d\mathbf{X}_{\rm nob}. \tag{2.2}$$

We will first consider, in Section 2.2.1, an oversimplified version of the model before deriving the full model we will actually use in the subsequent sections.

2.2.1 Simplified model of the three hypotheses

To further clarify what each hypothesis proposes, first we will consider more closely the relationships between $X_{\rm p}$, $t_\star$, and $\mathbf{X}_{\rm ob}$ under each hypothesis. We will ignore $\mathbf{X}_{\rm nob}$ and $\mathbf{Y}$ for now and consider how $p(X_{\rm p}, t_\star, \mathbf{X}_{\rm ob})$ differs among hypotheses. The relationships are depicted in Figure 2.1. Note that this is a simplification for the purposes of clarification, and does not fully represent the full model we use.

Under the Nurture hypothesis, the age of the system drives the planetary property of interest; in other words, $X_{\rm p}$ evolves over time. Thus $X_{\rm p}$ only depends directly on $t_\star$:

$$p(X_{\rm p}, t_\star, \mathbf{X}_{\rm ob}) = p(X_{\rm p}|t_\star)p(\mathbf{X}_{\rm ob}|t_\star)p(t_\star). \tag{2.3}$$

Note that $\mathbf{X}_{\rm ob}$ may have some dependence on $t_\star$, or vice versa, (e.g., stars changing temperature as they age) so that $X_{\rm p}$ appears correlated $\mathbf{X}_{\rm ob}$, but $\mathbf{X}_{\rm ob}$ is not the fundamental driver of $X_{\rm p}$. Such a relationship makes it challenging to distinguish whether the underlying source of observed correlations is Nature (i.e., $\mathbf{X}_{\rm ob}$ is the driver of $X_{\rm p}$) or Nurture (i.e., $t_\star$ is the driver of $X_{\rm p}$).

Under the Nature hypothesis, a component of $\mathbf{X}_{\rm ob}$ – a system parameter other than the age – is directly responsible for $X_{\rm p}$; in other words, $X_{\rm p}$ does not evolve with time but is instead determined by the conditions of the system's formation. So we can write:

$$p(X_{\rm p}, t_\star, \mathbf{X}_{\rm ob}) = p(X_{\rm p}|\mathbf{X}_{\rm ob}(t_\star))p(\mathbf{X}_{\rm ob}|t_\star)p(t_\star). \tag{2.4}$$

Note that $X_{\rm p}$ may still appear correlated with the system age because of the relationship between $\mathbf{X}_{\rm ob}$ and $t_\star$, but in the Nature hypothesis, $X_{\rm p}$ is only directly connected to $\mathbf{X}_{\rm ob}$.

Under the Chance hypothesis, $X_{\rm p}$ is a random process, so it is not related to $\mathbf{X}_{\rm ob}$ or $t_\star$ at all. There still may be a relationship between $\mathbf{X}_{\rm ob}$ and $t_\star$. So we can write:

$$p(X_{\rm p}, t_\star, \mathbf{X}_{\rm ob}) = p(X_{\rm p})p(\mathbf{X}_{\rm ob}|t_\star)p(t_\star). \tag{2.5}$$

In this subsection we have rewritten $p(X_{\rm p}, \mathbf{X}_{\rm ob}, t_\star)$ for each hypothesis as a chain of dependencies. For the rest of the paper, we will continue to separate out $p(X_{\rm p})$ as appropriate for each hypothesis, but instead of expressing the rest as a series of conditional probabilities, we will use the joint probability for $t_\star$, $\mathbf{X}_{\rm ob}$, and $\mathbf{X}_{\rm nob}$ (which we have excluded in this subsection): $p(t_\star, \mathbf{X}_{\rm ob}, \mathbf{X}_{\rm nob})$. Due to the definition of conditional probability, this is equivalent to a chain of dependencies like those expressed above but allows for more flexibility in how the chain is constructed (i.e. in expressing which

parameters are dependent upon which).

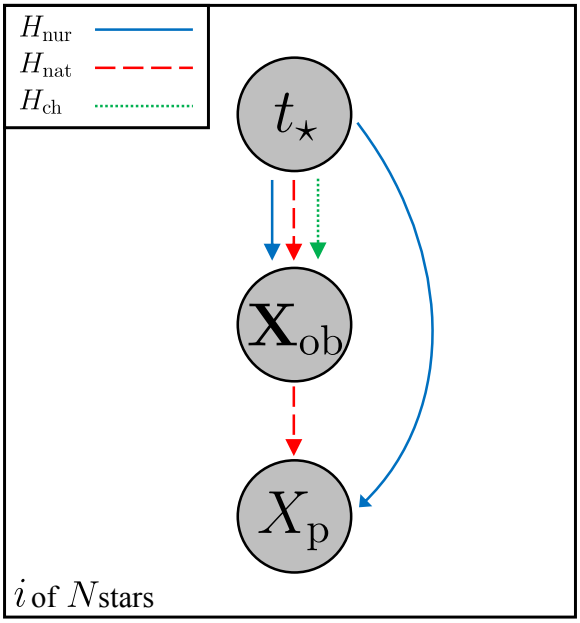

Figure 2.1. Graphical representation of the relationships between $X_{\rm p}$, $t_\star$, and $\mathbf{X}_{\rm ob}$ under the three hypotheses. Relations under the Nurture hypothesis are shown with a solid blue line, those under the Nature hypothesis with a dashed red line, and those under the Chance hypothesis with a dotted green line. The "i of N stars" indicates that the plate is iterated over each of the N systems in the sample. Gray circles represent observed parameters: the planetary property of interest ($X_{\rm p}$), the stellar age ($t_\star$), and other observed parameters ($\mathbf{X}_{\rm ob}$).

2.2.2 Hypothesis 1: Nurture (Age-driven)

In the Nurture hypothesis, the observed planetary property is driven by the age of the star. Since this hypothesis involves evolution over time, the current configuration depends on the configuration in which the system was formed, which we represent as $X_{\rm p0}$, and an evolutionary timescale $t_{\rm e}$, which in general may depend on $\mathbf{X}_{\rm ob}$, $\mathbf{X}_{\rm nob}$, and $X_{\rm p0}$. This timescale represents the time it takes for a planetary system to attain some value of $X_{\rm p}$ that is different from $X_{\rm p0}$ (e.g., the disruption of an orbital resonance, the orbital realignment with a host star's spin axis). $X_{\rm p0}$ and $t_{\rm e}$ are members of $\mathbf{X}_{\rm nob}$, but here we write them out explicitly, along with $\mathbf{X}_{\rm nob}$, because of their importance in this hypothesis. We also separate out the integrand in Eqn. 2.2 according to the rules of conditional probability for this hypothesis, where $X_{\rm p}$ depends on $t_\star$ but not explicitly on $\mathbf{X}_{\rm ob}$ or anything in $\mathbf{X}_{\rm nob}$ except $t_{\rm e}$ and $X_{\rm p0}$. Finally, we note that $t_\star$ may also correlate with other parameters contained within $\mathbf{X}_{\rm ob}$ and $\mathbf{X}_{\rm nob}$; such a dependence can be responsible

for apparent correlations of $X_{\rm p}$ with $\mathbf{X}_{\rm ob}$, as explained in Section 2.2.1.

In this time-dependent hypothesis, the initial configuration $X_{\rm p0}$ is independent of all parameters in $\mathbf{X}_{\rm ob}$ or $\mathbf{X}_{\rm nob}$. There could, in theory, be a situation in which the probability of some value of $X_{\rm p0}$ depends on other properties of the system, and then that value evolves over time. This would represent a sort of hybrid between the Nurture and Nature hypotheses, as both evolution over time and dependence on other system properties would play an important role. For our framework, however, we are considering whether a system's $X_{\rm p}$ is *primarily* driven by evolution over time or *primarily* driven by other system properties. So in this hypothesis, where time is the important factor, we can separate $X_{\rm p0}$ from other observed and non-observed parameters. Putting this all together yields a probability

$$\begin{aligned} p(X_{\rm p}, t_\star, \mathbf{X}_{\rm ob}|\mathbf{Y}) &= \iiint p(X_{\rm p}|t_\star, t_{\rm e}, X_{\rm p0}, \mathbf{X}_{\rm ob}, \mathbf{X}_{\rm nob}, \mathbf{Y}) \\ &\qquad \times p(t_\star, t_{\rm e}, X_{\rm p0}, \mathbf{X}_{\rm ob}, \mathbf{X}_{\rm nob}|\mathbf{Y}) dt_{\rm e} dX_{\rm p0} d\mathbf{X}_{\rm nob} \\ &= \iiint p(X_{\rm p}|t_\star, t_{\rm e}, X_{\rm p0}, \mathbf{Y}) p(t_{\rm e}|\mathbf{X}_{\rm ob}, \mathbf{X}_{\rm nob}, X_{\rm p0}, \mathbf{Y}) \\ &\qquad \times p(t_\star, \mathbf{X}_{\rm ob}, \mathbf{X}_{\rm nob}|\mathbf{Y}) p(X_{\rm p0}|\mathbf{Y}) dt_{\rm e} dX_{\rm p0} d\mathbf{X}_{\rm nob}. \end{aligned} \tag{2.6}$$

where we have assumed that $t_{\rm e}$ does not depend on $t_\star$ and that $X_{\rm p0}$ is independent of $t_\star$, $\mathbf{X}_{\rm ob}$, and $\mathbf{X}_{\rm nob}$, and vice versa. While $X_{\rm p}$ does not explicitly depend on $\mathbf{X}_{\rm ob}$ and $\mathbf{X}_{\rm nob}$, it is related through $t_{\rm e}$, as discussed above.

In general, $X_{\rm p}$ may be a continuous quantity spanning a range of possible values, so $p(X_{\rm p})$ and $p(X_{\rm p0})$ would be continuous distributions that may depend on general population hyperparameters, $\mathbf{Y}$, and/or system-specific properties, $t_\star$, $\mathbf{X}_{\rm ob}$, and $\mathbf{X}_{\rm nob}$. However, in some applications of these equations, the planetary property of interest may be a binary parameter, e.g., a system either has a 2:1 resonance or does not. When $X_{\rm p}$ is a binary parameter, $p(X_{\rm p0})$ is a Bernoulli distribution set by an overall, population-wide fraction of systems, f_0, that start out with said property – e.g., the overall fraction of systems that begin with a 2:1 resonance. This fraction will not necessarily be known a priori, so we treat it as a hyperparameter over which we marginalize outside the product of the likelihoods of individual systems.

Furthermore, the discrete nature of $X_{\rm p}$ and $X_{\rm p0}$ in this binary scenario means that we can change the integral over $X_{\rm p0}$ in Eqn. 2.6 to a sum instead. $X_{\rm p} = 1$ if the system possesses the property of interest and 0 if it does not, and similarly for $X_{\rm p0}$. The initial fraction f_0 then represents the proportion of systems with $X_{\rm p0} = 1$. Thus, when $X_{\rm p}$ is a binary parameter, the general system likelihood equation we use for the Nurture

hypothesis, modified from Eqn. 2.6, is:

$$p(X_{\rm p}, t_\star, \mathbf{X}_{\rm ob}|f_0, \mathbf{Y}) = \iint \sum_{X_{\rm p0}=0}^{1} p(X_{\rm p}|t_\star, t_{\rm e}, X_{\rm p0}, \mathbf{Y}) p(t_{\rm e}|X_{\rm p0}, \mathbf{X}_{\rm ob}, \mathbf{X}_{\rm nob}, \mathbf{Y}) \times p(t_\star, \mathbf{X}_{\rm ob}, \mathbf{X}_{\rm nob}|\mathbf{Y}) p(X_{\rm p0}|f_0) dt_{\rm e} d\mathbf{X}_{\rm nob}. \tag{2.7}$$

where $p(X_{\rm p0}|f_0) = 1 - f_0$ for $X_{\rm p0} = 0$ and $p(X_{\rm p0}|f_0) = f_0$ for $X_{\rm p0} = 1$.

In many applications, including all applications we consider in this paper, $X_{\rm p}$ can only evolve in a single direction; for example, we can consider a host star realigning with its planet's orbital axis without subsequently becoming misaligned again. In such cases, when both $X_{\rm p}$ and $X_{\rm p0}$ are discrete binary parameters, let the evolutionary timescale $t_{\rm e}$ represent the time it takes a system to attain $X_{\rm p} = 0$ from $X_{\rm p0} = 1$. We separate out Eqn. 2.7 into specific instances for each possible combination of $X_{\rm p}$ and $X_{\rm p0}$. In such a scenario, a system with $X_{\rm p0} = 1$ and $X_{\rm p} = 0$ must be older than its evolutionary timescale; a system with $X_{\rm p0} = 1$ and $X_{\rm p} = 1$ must be younger than its evolutionary timescale; and a system with $X_{\rm p0} = 0$ must have $X_{\rm p} = 0$ and has no evolutionary timescale. We can thus adjust the limits of integration for $t_{\rm e}$ in Eqn. 2.7 for each case, yielding (see Appendix 2.6 for full derivation):

$$p(X_{\rm p}, t_\star, \mathbf{X}_{\rm ob}|f_0, \mathbf{Y}) = \begin{cases} \int \left[1 - f_0 + f_0 \int_0^{t_\star} p(t_{\rm e}|X_{\rm p0}, \mathbf{X}_{\rm ob}, \mathbf{X}_{\rm nob}, \mathbf{Y}) dt_{\rm e}\right] & \\ \quad \times p(t_\star, \mathbf{X}_{\rm ob}, \mathbf{X}_{\rm nob}|\mathbf{Y}) d\mathbf{X}_{\rm nob} & , X_{\rm p} = 0 \\ f_0 \iint_{t_\star}^{\infty} p(t_{\rm e}|X_{\rm p0}, \mathbf{X}_{\rm ob}, \mathbf{X}_{\rm nob}, \mathbf{Y}) dt_{\rm e} & \\ \quad \times p(t_\star, \mathbf{X}_{\rm ob}, \mathbf{X}_{\rm nob}|\mathbf{Y}) d\mathbf{X}_{\rm nob} & , X_{\rm p} = 1. \end{cases} \tag{2.8}$$

Note that the above equations are only valid for a binary $X_{\rm p}$ when the system can go from $X_{\rm p0} = 1$ to $X_{\rm p} = 0$ but cannot go from $X_{\rm p0} = 0$ to $X_{\rm p} = 1$. If the system is better described as going from $X_{\rm p0} = 0$ to $X_{\rm p} = 1$ but not from $X_{\rm p0} = 1$ to $X_{\rm p} = 0$, one only need switch the values of $X_{\rm p}$ in Eqn. 2.8 to get the correct equations.

2.2.3 Hypothesis 2: Nature (Driven by inherent system properties)

In this scenario, the planet property of interest does not change with time but instead depends deterministically on one or more system properties which are included in $\mathbf{X}_{\rm ob}$. In this hypothesis, a relation between $\mathbf{X}_{\rm ob}$ and $t_\star$ may make $X_{\rm p}$ appear to be correlated with age, but $\mathbf{X}_{\rm ob}$ is the true driving force behind $X_{\rm p}$. Furthermore, because it depends directly on $\mathbf{X}_{\rm ob}$, we will assume $X_{\rm p}$ is also independent of $\mathbf{X}_{\rm nob}$. This means the integrand

in Eq. 2.2 can be separated into two probabilities to give the following:

$$p(X_{\rm p}, t_\star, \mathbf{X}_{\rm ob}|\mathbf{Y}) = \int p(X_{\rm p}|\mathbf{X}_{\rm ob}, \mathbf{Y}) p(t_\star, \mathbf{X}_{\rm ob}, \mathbf{X}_{\rm nob}|\mathbf{Y}) d\mathbf{X}_{\rm nob}. \tag{2.9}$$

Note that there is no overall fraction here when $X_{\rm p}$ is a binary parameter because $X_{\rm p}$ does not evolve over time and so the fraction of the sample with $X_{\rm p}$ is set by the sample's distribution of $\mathbf{X}_{\rm ob}$. However, there may be some applications in which the dependence of $X_{\rm p}$ on $\mathbf{X}_{\rm ob}$ is stochastic, rather than deterministic. In such cases, a fraction may be introduced, as a hyperparameter if it is unknown, to describe the distribution of $X_{\rm p}$.

We note that stellar metallicity is an important system parameter that has a great influence on planetary system formation and is also connected to stellar age. While several aspects of the connection between metallicity and planets have been documented (see, for example, Fischer & Valenti 2005; Dawson & Murray-Clay 2013; Buchhave et al. 2014; Wang & Fischer 2015; Dawson et al. 2015), stellar metallicity has not been proposed as an explanation for the observed trends we examine in this particular work. There may be future applications where an observed trend with age could actually be due to metallicity, or vice versa. These could be assessed with a Nature vs. Nurture odds ratio by including the metallicity parameter in $\mathbf{X}_{\rm ob}$.

2.2.4 Hypothesis 3: Chance

Here, the planet property of interest is not related to any observed system parameters. Therefore we can separate $X_{\rm p}$ from $t_\star$, $\mathbf{X}_{\rm ob}$, and $\mathbf{X}_{\rm nob}$, and Eqn. 2.2 becomes

$$p(X_{\rm p}, t_\star, \mathbf{X}_{\rm ob}|\mathbf{Y}) = \int p(X_{\rm p}|\mathbf{Y}) p(t_\star, \mathbf{X}_{\rm ob}, \mathbf{X}_{\rm nob}|\mathbf{Y}) d\mathbf{X}_{\rm nob}. \tag{2.10}$$

In the case of a binary $X_{\rm p}$, we can again use an overall fraction f, representing the proportion of systems with $X_{\rm p} = 1$. Under the Chance hypothesis, this fraction is independent of $\mathbf{X}_{\rm ob}$ and $\mathbf{X}_{\rm nob}$. The discrete nature of $X_{\rm p}$ in the binary scenario allows us to write separate expressions for the cases of $X_{\rm p} = 0$ and $X_{\rm p} = 1$:

$$p(X_{\rm p}, t_\star, \mathbf{X}_{\rm ob}|f, \mathbf{Y}) = \begin{cases} (1-f) \int p(t_\star, \mathbf{X}_{\rm ob}, \mathbf{X}_{\rm nob}|\mathbf{Y}) d\mathbf{X}_{\rm nob} & , X_{\rm p} = 0 \\ f \int p(t_\star, \mathbf{X}_{\rm ob}, \mathbf{X}_{\rm nob}|\mathbf{Y}) d\mathbf{X}_{\rm nob} & , X_{\rm p} = 1 \end{cases} \tag{2.11}$$

where we use $p(X_{\rm p}|f) = (1-f)$ for $X_{\rm p} = 0$ and $p(X_{\rm p}|f) = f$ for $X_{\rm p} = 1$.

2.2.5 Odds Ratios

In the previous three subsections, we have derived equations for $p(X_{\rm p}, t_\star, \mathbf{X}_{\rm ob})$ for three different explanations for the observed distribution of $X_{\rm p}$. Each quantity in the parentheses – $X_{\rm p}$, $t_\star$, and $\mathbf{X}_{\rm ob}$ – represents the driving force behind $X_{\rm p}$ in one hypothesis. In the Nurture hypothesis, $t_\star$ is the driver: the planetary property evolves with time and is thus caused by the age of the system. In the Nature hypothesis, $\mathbf{X}_{\rm ob}$ is the driver: the planetary property does not evolve with time, but instead depends on some other characteristic of its formation environment. In the Chance hypothesis, since the planetary property does not evolve with time and does not depend on the formation environment, the only determining factor is the chance values of $X_{\rm p}$.

In Figure 2.2, we present a graphical representation of possible relationships between parameters in Eqn. 2.2 under different hypotheses. For simplicity, we do not show every possible relationship, but rather focus on those that most often become relevant in the applications we examine.

Ultimately we are interested in the odds ratios for pairs of hypotheses to determine which hypothesis is most favored by the data. The odds ratios are obtained by applying the equations in the previous subsections to the observational data according to Eqn. 2.1. For the purposes of this paper, we will consider odds ratios of $\sim 1-10$ to be inconclusive, $\sim 10-100$ to be moderately supportive but not decisive, and ~ 100 and above to be strong, similar to the scale given by Jeffreys (1961) and Kass & Raftery (1995).

The calculation of the ratios may result in quantities cancelling out in some cases, reducing the need to determine suitable priors for and relationships between some parameters. In particular, if there are no parameters of interest in $\mathbf{X}_{\rm nob}$ to consider and if $p(t_\star, \mathbf{X}_{\rm ob})$ is independent of $\mathbf{Y}$, then we can write, from Eqns. 2.6, 2.9, and 2.10:

$$H_{\rm nur} : p(X_{\rm p}, t_\star, \mathbf{X}_{\rm ob}|\mathbf{Y}) = \iint p(X_{\rm p}|t_\star, t_{\rm e}, X_{\rm p0}, \mathbf{Y}) p(t_{\rm e}|\mathbf{X}_{\rm ob}, X_{\rm p0}, \mathbf{Y}) \times p(X_{\rm p0}|\mathbf{Y}) dt_{\rm e} dX_{\rm p0} p(t_\star, \mathbf{X}_{\rm ob}) \tag{2.12}$$

$$H_{\rm nat} : p(X_{\rm p}, t_\star, \mathbf{X}_{\rm ob}|\mathbf{Y}) = p(X_{\rm p}|\mathbf{X}_{\rm ob}, \mathbf{Y}) p(t_\star, \mathbf{X}_{\rm ob}) \tag{2.13}$$

$$H_{\rm ch} : p(X_{\rm p}, t_\star, \mathbf{X}_{\rm ob}|\mathbf{Y}) = p(X_{\rm p}|\mathbf{Y}) p(t_\star, \mathbf{X}_{\rm ob}). \tag{2.14}$$

The common term between these three equations, $p(t_\star, \mathbf{X}_{\rm ob})$, will cancel when the odds ratios are calculated, eliminating the need to specify the exact relationship between $t_\star$ and $\mathbf{X}_{\rm ob}$ or the underlying distribution of these parameters.

Finally, we note that our framework does not account for measurement uncertainties

on $X_{\rm p}$, $t_\star$, or $\mathbf{X}_{\rm ob}$. This is an additional complicating factor and we recognize its omission makes our framework less general. We plan to address this in a future paper and incorporate measurement uncertainties in our general framework as well as the applications we investigate here.

2.3 Are systems with 2:1 resonances younger than those without?

Mean motion resonances are important tracers of planetary systems' formation and evolution. Dissipative processes – including tides (e.g.,Yoder 1979) and planet-disk interactions (e.g., Lee & Peale 2002; MacDonald & Dawson 2018) – can capture planets into resonance. The initial frequency of resonances informs us about the planets' formation environment and early evolution (e.g., Malhotra 1993; Goldreich & Schlichting 2014), but resonances can be broken by later dynamical interactions among planets (e.g., Thommes et al. 2008; Izidoro et al. 2017). Investigating if and how the occurrence of orbital resonances changes with system age can help us trace back the initial fraction and also better understand the processes that subsequently destabilize resonances.

Koriski & Zucker (2011) examined the ages and resonance states of a sample of multiplanet systems. For the sake of homogeneity, they limited their sample to 30 systems of planets discovered via radial velocity around F, G, and K stars with stellar ages derived from chromospheric activity calcium H and K lines (averaging when a target had multiple age estimates from different studies). As described in the review by Soderblom (2010), measuring stellar activity levels is one of the most widely used methods of age determination, but it is subject to systematics that are not fully understood, and activity levels for stars of the same age can vary considerably. With calcium H and K lines, the age is calculated from an index $R'_{\rm HK}$ derived from the H and K line ratios. While individual stellar age uncertainties were not reported, several of the sources cited by Koriski & Zucker (2011) calculated stellar age with a fit for $R'_{\rm HK}$ versus age determined by Mamajek & Hillenbrand (2008), who estimated a 60% uncertainty on ages derived from their relation when taking into account calibration and observational uncertainties as well as astrophysical scatter.

To determine those systems that were in resonance, they defined a "normalized

commensurability proximity" score as follows:

$$\delta = 2\frac{|r - r_c|}{r + r_c} \tag{2.15}$$

where r is the measured period ratio and r_c is the period commensurability ratio – 2:1 in this case – against which r is compared. They defined a system to have a period commensurability if it had $\delta < 0.1$. With this criteria, the dataset consists of five systems with 2:1 resonances and 25 systems without 2:1 resonances.

Koriski & Zucker (2011) found that the planetary systems in their sample that exhibit 2:1 period ratios tended to be younger than those that do not, with a median age difference of 2.15 Gyr (Figure 2.3). The authors ran a series of random permutation tests on the sample and found that only about 0.4% of the randomized samples yielded a median age difference between systems with and without a 2:1 resonance that is greater than the measured value. While acknowledging the small sample size and uncertainties in stellar ages, the authors suggested this finding is indicative of such commensurabilities having only a finite lifetime.

Random permutation tests reveal the probability of a trend emerging by chance, but in the framework of Bayesian hypothesis testing, we need to compare this probability to that expected from some competing model. Dong & Dawson (2016) took the first step toward such a comparison by exploring the initial fraction of resonant systems and resonant disruption timescale needed to account for the observed trend. They found that their model could account for the data only if all systems begin in resonance and are disrupted on a timescale very similar to the age difference between the 2:1 resonant and nonresonant samples. Their results implied that the model parameters may need to be quite fine-tuned, which would penalize the resonance disruption hypothesis when assessed within a Bayesian hypothesis testing framework.

Here we use the same dataset as Koriski & Zucker (2011) with the framework from Section 2.2 to compare the evidence for the Nurture and Chance hypotheses: that 2:1 resonances are systematically disrupted (Nurture); and that there is no astrophysical correlation between 2:1 resonances and age, so that the perceived trend is merely due to chance. We show a graphical representation of these two hypotheses in Figure 2.4. Since we are unaware of any proposed correlations between the presence of 2:1 resonances and system parameters other than age, we do not test the Nature hypothesis for this case in this work, though we may investigate it in the future. In Section 2.3.1, we adapt the general equations derived in Section 2.2 to this specific case. We present the results

of our analysis in Section 2.3.2, show and discuss contour plots of hyperparameters in Section 2.3.3, and briefly summarize in Section 2.3.4.

2.3.1 Equations for each hypothesis

2.3.1.1 Hypothesis 1: Nurture (Age-driven)

Under the Nurture hypothesis applied to the 2:1 resonance case, the planetary property of interest, $X_{\rm p}$, is the resonance state of the system. We represent this state by the binary parameter R, which is 1 when a system has a 2:1 resonance and 0 when it does not. The initial state $X_{\rm p0}$ is the initial resonance state of the system, R_0, which is defined in the same way as R. The evolutionary timescale in this case is a resonance disruption timescale, which we represent with $t_{\rm d}$. There are no other observational data we consider, so we drop $\mathbf{X}_{\rm ob}$. Substituting these variables into the general Nurture hypothesis equation for a binary parameter with one-directional evolution (Eqn. 2.8) gives:

$$p(R, t_\star | f_0) = \begin{cases} \int \left[(1-f_0) + f_0 \int_0^{t_\star} p(t_{\rm d}|R_0, \mathbf{X}_{\rm nob}) dt_{\rm d}\right] p(t_\star, \mathbf{X}_{\rm nob}) d\mathbf{X}_{\rm nob} & , R = 0 \\ f_0 \iint_{t_\star}^{\infty} p(t_{\rm d}|R_0, \mathbf{X}_{\rm nob}) p(t_\star, \mathbf{X}_{\rm nob}) dt_{\rm d} d\mathbf{X}_{\rm nob} & , R = 1 \end{cases} \tag{2.16}$$

where f_0 represents the fraction of systems that begin with a 2:1 resonance.

We assume the underlying distribution of disruption timescales is log-normal – and note that a system with $R_0 = 0$ must have $R = 0$ and has no timescale – and that it is independent of anything in $\mathbf{X}_{\rm nob}$:

$$p(\log_{10}(t_{\rm d})|\mu, \sigma) = \frac{1}{\sqrt{2\pi\sigma^2}} \exp\left(\frac{-(\log_{10}(t_{\rm d}) - \mu)^2}{2\sigma^2}\right). \tag{2.17}$$

This choice is appropriate because orbital evolution processes can happen on timescales that span many orders of magnitude, making a logarithmic form suitable. Resonance systems close to the stability limit might break apart quickly, while others may be stable for longer than the current age of the universe. A wide log-normal prior is an uninformative way to capture this range of behavior.

This formulation introduces two unknown parameters, namely the mean μ and standard deviation σ of the prior of $\log_{10}(t_{\rm d})$. Both μ and σ are population-wide variables; thus, they are hyperparameters that are marginalized over outside the product of individual likelihoods of each system. We impose uniform hyperpriors on these variables

with the following ranges, given in $\log_{10}([\text{yr}])$ space:

$$p(\mu) = \text{U}(6, 16) \tag{2.18}$$

$$p(\sigma) = \text{U}(0, 20). \tag{2.19}$$

These wide ranges are to account for our relative lack of knowledge about resonance disruption timescales and encompass timescales ranging from roughly right after planet formation – the earliest conceivable time that a resonance could be broken, which is roughly 10^6 years after system formation – to many orders of magnitude beyond the current age of the universe. We note that the uniform hyperprior on μ is nearly uninformative, but the uniform hyperprior on σ is not. The true uninformative hyperprior for σ, as a scale parameter, would be $1/\sigma^2$. The uniform hyperprior is more weighted to large values of σ. However, as we expect resonance disruption timescales to span many orders of magnitude, such a weighting is appropriate for this case and we stick with the uniform hyperprior.

For simplicity, we will assume that $p(t_\star)$ does not depend on anything in $\mathbf{X}_{\text{nob}}$. Since, then, neither $t_\star$ nor t_d depends explicitly on other system properties, we can remove $\mathbf{X}_{\text{nob}}$ in Eqn. 2.16, and the $p(t_\star)$ term will cancel out when the odds ratio is calculated, as described in Section 2.2.5.

We give f_0 a uniform hyperprior from 0 to 1:

$$p(f_0) = \text{U}(0, 1). \tag{2.20}$$

We note that since f_0 is a Bernoulli distribution parameter, a uniform hyperprior is not actually uninformative. For such a variable, the uninformative hyperprior is a Beta distribution with both parameters set to 1/2, Beta(1/2,1/2). We will also calculate the odds ratios using the Beta distribution on f_0 and compare to the results from a uniform hyperprior.

With the above assumptions, Eqn. 2.16 becomes:

$$p(R, t_\star|\mu, \sigma, f_0) = \begin{cases} \left[(1 - f_0) + f_0 \int_0^{t_\star} p(t_\text{d}|\mu, \sigma) dt_\text{d}\right] p(t_\star) & , R = 0 \\ f_0 \int_{t_\star}^{\infty} p(t_\text{d}|\mu, \sigma) dt_\text{d} p(t_\star) & , R = 1. \end{cases} \tag{2.21}$$

2.3.1.2 Hypothesis 2: Nature (Driven by inherent system properties)

We are not aware of any proposed correlations between the presence of 2:1 resonances and system parameters other than age, so we do not test this hypothesis for the resonances case at this time. If a possible relationship does emerge, such as with stellar mass $M_\star$, Eqn. 2.9 could be applied to give

$$p(R, t_\star, M_\star) = \int p(R|M_\star)p(t_\star, M_\star, \mathbf{X}_{\rm nob})d\mathbf{X}_{\rm nob}, \tag{2.22}$$

where we have set $\mathbf{X}_{\rm ob} = M_\star$. $\mathbf{X}_{\rm nob}$ could be, for example, a property of the initial proto-planetary disk thought to affect capture into resonance.

2.3.1.3 Hypothesis 3: Chance

Again, we do not consider any other observational data or unobserved parameters. Thus under the Chance hypothesis, the general equation for a binary $X_{\rm p}$ (Eqn. 2.11) applied to the resonance case gives

$$p(R, t_\star|f) = \begin{cases} p(t_\star)(1-f) & , R = 0 \\ p(t_\star)f & , R = 1. \end{cases} \tag{2.23}$$

We give f, the fraction of systems with a 2:1 resonance, a uniform distribution from 0 to 1, but will also compare the odds ratios to those obtained when f is given the uninformative hyperprior of Beta(1/2,1/2).

2.3.2 Results

To calculate the odds ratio, we compute the individual system likelihoods from Eqn. 2.21 (Nurture hypothesis) and Eqn. 2.23 (Chance hypothesis). For each hypothesis, we multiply those individual likelihoods and then marginalize over the hyperparameters f_0, as well as μ and σ for the Nurture hypothesis, according to Eqn. 2.1. The complete equations for each hypothesis are

$$\begin{aligned} p(H_{\rm nur}) = \iiint \prod_{R=0} \left[p(t_\star)(1-f_0) + p(t_\star)f_0 \int_0^{t_\star} p(t_{\rm d}|\mu,\sigma)dt_{\rm d}\right] \\ \times \prod_{R=1} \left[p(t_\star)f_0 \int_{t_\star}^{\infty} p(t_{\rm d}|\mu,\sigma)dt_{\rm d}\right] p(\mu)p(\sigma)p(f_0)d\mu d\sigma df_0 \end{aligned} \tag{2.24}$$

$$p(H_{\rm ch}) = \int \prod_{R=0} \left[p(t_\star)(1-f)\right] \prod_{R=1} \left[p(t_\star)f\right] p(f)df. \tag{2.25}$$

Parameter	Prior
Disruption timescale $(\log_{10}(t_{\rm d})\|\mu,\sigma)$	$\frac{1}{\sqrt{2\pi\sigma^2}}\exp\left(\frac{-(\log_{10}(t_{\rm d})-\mu)^2}{2\sigma^2}\right)$
Mean of $\log_{10}(t_{\rm d})$ (μ)	U(6,16)
Standard deviation of $\log_{10}(t_{\rm d})$ (σ)	U(0,20)
Initial 2:1 resonance fraction (f_0)	U(0,1)
2:1 resonance fraction (f)	U(0,1)

Table 2.1. Priors of relevant parameters for the resonance case. The ranges for μ and σ are given in $\log_{10}([\rm yr])$.

The priors of relevant parameters are summarized in Table 2.1, where we have written out the complete equations for the Nurture and Chance hypotheses, where the ranges for μ and σ are given in $\log_{10}([\rm yr])$.

The integrations are performed using the Python package scipy.integrate.nquad with default settings, which uses techniques from the Fortran library QUADPACK. Specifically, it uses a Clenshaw-Curtis method with Chebyshev moments if the integration limits are finite, and it uses a Fourier integral in the case of an infinite limit. For comparison we also compute integrals using the numerical integrator NIntegrate in Mathematica, which by default uses an adaptive Genz–Malik algorithm, and find excellent agreement with the results from Python.

We find that the odds ratio of the Nurture hypothesis to the Chance hypothesis is 2.2. This result only weakly supports the Nurture scenario, and we cannot favor one hypothesis over the other with the current information. We can say that according to this approach, there is not enough evidence in the Koriski & Zucker (2011) dataset to support systematic resonance disruption. To get a better idea of whether 2:1 resonances do eventually get disrupted, we would need to use a larger sample of 2:1 resonant systems, ideally with a wider age range.

We also compute the odds ratio with f_0 and f both assigned uninformative hyperpriors of Beta(1/2,1/2). We obtain an odds ratio of the Nurture hypothesis to the Chance hypothesis of 2.0. This is not a significant change from before and still does not allow us to favor one hypothesis over the other.

In Appendix 2.6, we perform additional variations in our calculations by removing systems with highly-uncertain ages, bootstrapping the data, and marginalizing over the threshold for a system having a 2:1 resonance. In each of these treatments, we obtain odds ratios of Nurture vs. Chance close to our original value of 2.2, and thus still cannot favor one hypothesis over the other.

2.3.3 Contour plots

In Figure 2.5 we display probability contour plots of hyperparameters f_0 vs. μ (top left), σ vs. μ (top right), and f_0 vs. σ (bottom left) from the equations for the Nurture hypothesis. Note that these are not plots of the posterior or the likelihood; rather, they are plots of the part of the posterior that does not get cancelled in the odds ratio. They are also relative, not absolute, probabilities that have been normalized such that the highest value is 1. The probabilities have been calculated on a grid for each value of f_0, μ, and σ. The contour plots indicate the values of those hyperparameters that contribute the most to the odds ratio under the Nurture hypothesis and can also give some insight into why we do not see enough evidence for the Nurture hypothesis to favor it strongly over the Chance hypothesis.

The structure in the Nurture contour plots suggests a continuous distribution of solutions that fit the data with relatively high probability ($\gtrsim 70\%$ of the highest probability solution) under the Nurture hypothesis. The highest probability region in the f_0 vs. μ plot indicates that under the Nurture explanation, somewhere between about 20% and 50% of systems would start out with a 2:1 resonance and would most likely get disrupted after a few Gyr, a timescale similar to the ages of the sample stars (see Figure 2.3). The high probability region then stretches to the right across much of the range of μ. At the high-μ end, this corresponds to a disruption timescale much longer than the current age of the universe, and an initial fraction similar to the observed current fraction. In this high-μ solution, roughly 20% of systems start out with a 2:1 resonance, and these configurations are stable on very long timescales, which means we would see the vast majority of them still in resonance today. Thus this solution is essentially equivalent to the Chance hypothesis.

The σ vs. μ plot indicates that there is very little variation in the disruption timescale of a few Gyr from system to system, as it exhibits a peak near $\sigma = 0$. This is supported by the very narrow high probability region at the far left of the f_0 vs. σ plot. Figure 2.6 shows close up views of the $\sigma = 0$ to $\sigma = 1$ region in both the f_0 vs. σ and σ vs. μ plots, which reveal that the peaks are near, but not exactly at, $\sigma = 0$. These peaks imply that in the solution where 2:1 resonance systems get disrupted after a few Gyr, there is very little variation in the timescale from system to system, so they would essentially get disrupted nearly all at the same age. However, the f_0 vs. σ plot also indicates a high probability for values of σ from about 2.5 to 5, indicating a range of solutions with disruption timescale variations of several orders of magnitude. This region also is at an initial 2:1 resonance fraction of roughly 20%, suggesting it corresponds to the

high-μ solution evident in the f_0 vs. μ plot. This implies that in the solution where 2:1 resonances are broken on timescales much longer than the age of the universe (the solution equivalent to the Chance hypothesis), there is some notable variation in those timescales from system to system, such that we may see a few of the initially-resonant systems already disrupted today. Most 2:1 resonances, though, will still be intact, so the observed 2:1 resonance fraction will be very close to the initial 2:1 resonance fraction.

The small islands in the upper right of the left panel of Figure 2.6 are low probability valleys caused by outlier systems. However, while their effect is seen in the contour plot, the outliers do not bias the overall result; their removal results in an odds ratio of Nurture to Chance of 2.3, again a result only barely different from the original odds ratio of 2.2.

Overall, the area of the high-probability region is small compared to the entire hyperparameter space for the Nurture hypothesis. Low-probability white space (i.e., outside the lowest probability contour) exists because of our lack of prior knowledge on resonance disruption timescales and is present in the upper right corners of the f_0 vs. μ and f_0 vs. σ plots and in the entire upper half of the σ vs. μ plot. This space is eventually marginalized over to compute the total probability for the Nurture hypothesis. Since the low-probability regions take up a large portion of hyperparameter space compared to the high-probability regions, they diminish support for the Nurture hypothesis. In other words, the high probability hyper-parameters are too fine-tuned and are naturally penalized in this framework.

To investigate the effect of the priors on our results, we recompute the odds ratio using smaller prior ranges on μ and σ. From the original priors of $p(\mu) = \mathrm{U}(6, 16)$ and $p(\sigma) = \mathrm{U}(0, 20)$, we first cut the ranges down to $p(\mu) = \mathrm{U}(6, 10)$ and $p(\sigma) = \mathrm{U}(0, 10)$, in $\log_{10}([\mathrm{yr}])$ space. These alternative priors give an odds ratio of the Nurture to Chance hypothesis of 3.7. This treatment lends more support to the Nurture hypothesis, but only a little bit; it is still not very strongly favored. As an extreme case, we further cut down the priors to $p(\mu) = \mathrm{U}(9, 10)$ and $p(\sigma) = \mathrm{U}(0, 1)$. Rather than being physically motivated, this cut is entirely based on the contour plots in Figure 2.5 and designed to exclude the lower probability regions. Even so, these priors only give an odds ratio of Nurture to Chance of 15. This ratio is only moderately, but not decisively, in favor of the Nurture hypothesis. Considering this particular calculation is contrived to result in high probability for the Nurture hypothesis anyway, we do not place much stock in this solution. These results suggest that the odds ratio in this case is not strongly sensitive to the priors on μ and σ used.

The bottom right panel of Figure 2.5 shows a probability histogram of f under the

Chance hypothesis in blue, and the initial 2:1 resonance fraction (f_0) under the Nurture hypothesis with original hyperprior ranges on μ and σ (orange), with the first reduction of μ and σ hyperprior ranges (green, labeled as "$H_{\rm nur}$ v. 2"), and with the second reduction of μ and σ hyperprior ranges (red, labeled as "$H_{\rm nur}$ v. 3"). The curves have been normalized to have the same area. The observed 2:1 resonance fraction is shown with a dashed line. The observational data of 5/30 systems having a 2:1 resonance is only slightly less than the best-fit initial 2:1 resonance fraction under the Nurture hypothesis, which is at about 25%, and it is right at the peak of the best-fit 2:1 resonance fraction under the Chance hypothesis.

2.3.4 Summary

In summary, we do not find enough evidence in the data we use to strongly support the hypothesis that 2:1 resonances are systematically disrupted. This conclusion is robust against variations in the priors used for hyperparameters.

2.4 Is Stellar Obliquity Realignment Primarily Driven by Age or by Stellar Temperature?

A star's obliquity angle, also referred to as the spin-orbit alignment angle, is the angle between the star's rotation axis and the orbital angular momentum vector of a planet around the star. Our own Sun has a small – though significant – obliquity angle with the planets in the solar system (Beck & Giles, 2005; Gomes et al., 2017), and many systems have been observed in which the star has a much more severe misalignment (e.g., HAT-P-6b, Hébrard et al. 2011; HAT-P-30b, Johnson et al. 2011). There are many factors and processes that may influence the excitation and damping of stellar obliquities, such as tidal interactions and Kozai-Lidov cycles, but the details as well as which factors play a dominant role remain unclear (e.g., Section 3.2 of Dawson & Johnson 2018 and references therein).

Winn et al. (2010) observed a trend of stellar obliquity with temperature for stars with hot Jupiters: hot stars are preferentially misaligned with their planets' orbits and cool stars are well aligned. They set the division between aligned and misaligned groups at $T_\star = 6250$ K (i.e. at the Kraft break; Kraft 1967) and noted that at approximately this temperature and below, stars have a sizable convective envelope. The authors suggested that if this envelope is decoupled enough from the stellar core, it may aid the cooler stars

in tidally realigning with their planets on relatively short timescales. This observation of temperature dependence has also been supported by concurrent (Schlaufman, 2010) and follow up (Albrecht et al., 2012) studies.

However, Triaud (2011) looked at hot Jupiters orbiting A stars and found a trend with stellar age, in which younger stars have high obliquities and older stars are well aligned, with the separation at about 2.5 Gyr. The ages of the stars were compiled from past studies and derived using stellar isochrones or evolutionary tracks, with the exception of WASP-17. The age of WASP-17 was re-estimated for that paper using previously published data and evolutionary tracks. Isochrone placement is a widely used age determination method and is based on well-understood physics, but uncertainties in temperature and other measured parameters can make precise age constraints difficult because the isochrones are often closely spaced (Soderblom, 2010). Most of the ages used in Triaud (2011) have uncertainties between 0.5 and 1 Gyr. Triaud (2011) restricted their sample to stars with masses greater than $1.2M_{\odot}$ and pointed out that such stars will cool by several hundred Kelvin over their main sequence lifetimes. Thus, they proposed, it could be that stars are gradually realigned by tidal interactions as they age and also cool as they age, and that the cool aligned stars seen by Winn et al. (2010) are the older versions of the hot misaligned stars that have had more time to realign with planetary orbits. Albrecht et al. (2012) later argued that the apparent trend with age may be due to a change in tidal realignment efficiency connected to temperature, rather than evolution of time.

Because these stars' temperatures change as they age, it is unclear whether the true source of the trend is age or stellar temperature. Here, we apply our framework to the Triaud (2011) sample, using the temperatures reported in the TEPCAT catalogue (Southworth, 2011), to see if the obliquities are better modeled by a relation with age or with temperature. This dataset consists of 22 systems, 10 of which have misaligned stars according to the criteria of Triaud (2011) that a star is misaligned if its measured obliquity angle is $> 20°$. Uncertainties in the measured obliquity angle are typically between about 5° and 10°. There are 15 stars with temperature at or above 6250 K and seven stars with temperature below 6250 K. All 10 misaligned stars have temperature at or above 6250 K. Uncertainties in the stellar temperature are generally between about 50 K and 100 K. We derive the relevant equations in Section 2.4.1, present the results we obtain in Section 2.4.2, show and display contour plots of hyperparameters in Section 2.4.3, then summarize in Section 2.4.4. We show a graphical representation of the model for this case in Figure 2.7.

2.4.1 Equations for each hypothesis

2.4.1.1 Hypothesis 1: Nurture (Age-driven)

In this case, the property of interest is whether or not a planet's orbital axis is observed to be aligned with the spin axis of its host star. For simplicity, we do not concern ourselves with the actual value of the measured obliquity angle, but rather merely whether that angle indicates that the system is aligned or misaligned. We represent this with the parameter A, which is 1 if the star is misaligned and 0 if it is aligned, and use the criteria of Triaud (2011) that a star is misaligned if the observed obliquity is $> 20°$. We designate the initial alignment state as A_0. We also include an alignment timescale t_a. The additional observed data $\mathbf{X}_\mathrm{ob}$ is the stellar temperature for each system, $T_\star$. Substituting the relevant parameters into the general Nurture hypothesis equations for a binary X_p that evolves in only one direction (Eqn. 2.8) gives:

$$p(A,t_\star,T_\star|f_0) = \begin{cases} \int \left[(1-f_0) + f_0 \int_0^{t_\star} p(t_\mathrm{a}|A_0,T_\star,\mathbf{X}_\mathrm{nob})dt_\mathrm{a}\right] p(t_\star,T_\star,\mathbf{X}_\mathrm{nob})d\mathbf{X}_\mathrm{nob} & ,A=0 \\ f_0 \iint_{t_\star}^{\infty} p(t_\mathrm{a}|A_0,T_\star,\mathbf{X}_\mathrm{nob})p(t_\star,T_\star,\mathbf{X}_\mathrm{nob})dt_\mathrm{a}d\mathbf{X}_\mathrm{nob} & ,A=1. \end{cases} \tag{2.26}$$

where the hyperparameter f_0 here represents the initial fraction of systems with stars observed to be misaligned from their planet's orbital axis.

In general, since realignment would occur via tidal interactions between the planet and the star, the alignment timescale would depend on properties like the stellar mass. However, for the data we are considering here, the planetary systems are similar enough (hot Jupiters orbiting stars between about $1.2M_\odot$ and $1.5M_\odot$) that we can approximate t_a as being independent of other variables. In order to cover a broad range of possible timescales spanning many orders of magnitude, we give t_a a log-normal distribution with unknown mean and standard deviation. We give the mean μ a log-uniform hyperprior of U(6,16) and the standard deviation σ a log-uniform hyperprior of U(0,20), both in $\log_{10}([\mathrm{yr}])$ space. We again note that while the uniform hyperprior on μ is uninformative, the true uninformative hyperprior for σ would be $1/\sigma^2$. However, as we expect alignment timescales to span many orders of magnitude, a uniform hyperprior, which is weighted towards larger values of σ, is suitable for this case.

For simplicity, we treat $t_\star$ and $T_\star$ as being independent of other system parameters, both observed and not observed. This means that the joint probability between them,

$p(t_\star, T_\star)$ will cancel out when the odds ratios are calculated, as described in Section 2.2.5.

With these assumptions, the equation becomes similar in form to that for the resonances case, with the inclusion of the temperature data. We thus obtain a result very similar to Eqn. 2.21:

$$p(A, t_\star, T_\star|\mu, \sigma, f_0) = \begin{cases} p(t_\star, T_\star)\left[(1-f_0) + f_0 \int_0^{t_\star} p(t_\mathrm{a}|\mu,\sigma)dt_\mathrm{a}\right] & , A = 0 \\ p(t_\star, T_\star) f_0 \int_{t_\star}^{\infty} p(t_\mathrm{a}|\mu,\sigma)dt_\mathrm{a} & , A = 1. \end{cases} \tag{2.27}$$

We give the initial fraction f_0 a uniform hyperprior from 0 to 1. We note that this is not the uninformative hyperprior, since f_0 is a Bernoulli distribution parameter. The uninformative hyperprior is Beta(1/2,1/2), and we will compare the odds ratios from the uniform hyperprior with those from the Beta hyperprior.

2.4.1.2 Hypothesis 2: Nature (Driven by inherent system properties)

In this case, the Nature hypothesis is that the stellar obliquity is driven by the stellar temperature. We do not concern ourselves with other unobserved system parameters here, so the integral over $\mathbf{X}_\mathrm{nob}$ disappears. Then, adapting the general equation for the Nature hypothesis (Eqn. 2.9) gives:

$$p(A, t_\star, T_\star) = p(A|T_\star)p(t_\star, T_\star). \tag{2.28}$$

We separate the sample into hot and cool stars, with the dividing line at $T_\star = 6250$ K (i.e., at the Kraft break), following Winn et al. (2010), and consider a system to be misaligned if its projected obliquity is $> 20°$, as did Triaud (2011). The idea behind the hypothesis of a trend driven by temperature is that stars start out with a range of obliquities and the cool stars are able to quickly realign with planetary orbits (Winn et al., 2010). So although technically the obliquities change with time under this hypothesis too, we assume that hot stars realign so slowly that the change in obliquity is negligible and cool stars realign so quickly that we always observe them aligned. Indeed, all the cool stars in our sample are aligned. So for cool stars, we use the following:

$$p(A|T_\star < 6250 \text{ K}) = \begin{cases} 1 & , A = 0 \\ 0 & , A = 1. \end{cases} \tag{2.29}$$

Hot stars, on the other hand, retain the range of obliquities with which they started out. Thus, we expect some of these stars to be well aligned, both as an expected occasional

outcome of whatever process produces the obliquities and because what we observe is the projected, not true, obliquity angle. Since we do not know the fraction of hot misaligned systems we would expect to see, we introduce the hyperparameter $f_{\rm h}$, the fraction of hot systems observed to be misaligned, which we give a uniform hyperprior from 0 to 1. So we use the following for hot stars:

$$p(A|T_\star \geq 6250 \text{ K}, f_{\rm h}) = \begin{cases} 1 - f_{\rm h} & , A = 0 \\ f_{\rm h} & , A = 1. \end{cases} \tag{2.30}$$

Since the uniform hyperprior is not actually uninformative, we will also compare our results to the odds ratio obtained with assigning $f_{\rm h}$ the hyperprior Beta(1/2,1/2). For comparison, in the dataset we use, there is an observed misaligned fraction of hot stars of 10/15.

2.4.1.3 Hypothesis 3: Chance

In the Chance hypothesis, as before, we are not concerned with any other unobserved parameters in $\mathbf{X}_{\rm nob}$. So from the general equation for the Chance hypothesis with a binary planetary property of interest $X_{\rm p}$ (Eqn. 2.11),

$$p(A, t_\star, T_\star|f) = \begin{cases} p(t_\star, T_\star)(1 - f) & , A = 0 \\ p(t_\star, T_\star) f & , A = 1 \end{cases} \tag{2.31}$$

where f is the fraction of systems observed to be misaligned. We give f a uniform hyperprior from 0 to 1, but will also compare to the results obtained with a hyperprior of Beta(1/2,1/2).

2.4.2 Results

To obtain the odds ratios, we apply Eqn. 2.27 for the Nurture hypothesis, Eqn. 2.28 for the Nature hypothesis, and Eqn. 2.31 for the Chance hypothesis to our sample data to obtain individual system likelihoods. For each hypothesis, we multiply those individual likelihoods and then marginalize over the hyperparameters to obtain the overall likelihood for each hypothesis, according to Eqn. 2.1. The complete equations for each hypothesis

Parameter		Prior or Probability Function
Alignment timescale $(\log_{10}(t_{\rm a})\|\mu,\sigma)$		$\frac{1}{\sqrt{2\pi\sigma^2}}\exp\left(\frac{-(\log_{10}(t_{\rm a})-\mu)^2}{2\sigma^2}\right)$
Mean of $\log_{10}(t_{\rm a})$ (μ)		U(6,16)
Standard deviation of $\log_{10}(t_{\rm a})$ (σ)		U(0,20)
Initial misaligned fraction (f_0)		U(0,1)
Misaligned fraction of hot stars $(f_{\rm h})$		U(0,1)
Misaligned fraction (f)		U(0,1)
Alignment state	$A=0\|T_\star<6250$ K	1
	$A=1\|T_\star<6250$ K	0
	$A=0\|T_\star\geq 6250$ K, $f_{\rm h}$	$1-f_{\rm h}$
	$A=1\|T_\star\geq 6250$ K, $f_{\rm h}$	$f_{\rm h}$

Table 2.2. Priors and probability functions of relevant parameters for the obliquities case, with the parameters in the left column and the corresponding priors in the right column. The ranges for μ and σ are given in $\log_{10}([\rm yr])$.

are

$$p(H_{\rm nur}) = \iiint \prod_{A=0}\left[p(t_\star,T_\star)\left(1-f_0+f_0\int_0^{t_\star}p(t_{\rm a}|\mu,\sigma)dt_{\rm a}\right)\right] \times \prod_{A=1}\left[p(t_\star,T_\star)f_0\int_{t_\star}^{\infty}p(t_{\rm a}|\mu,\sigma)dt_{\rm a}\right]p(\mu)p(\sigma)p(f_0)d\mu d\sigma df_0 \quad (2.32)$$

$$p(H_{\rm nat}) = \int \prod_{A=0}\left[p(A=0|T_\star,f_{\rm h})p(t_\star,T_\star)\right]\prod_{A=1}\left[p(A=1|T_\star,f_{\rm h})p(t_\star,T_\star)\right]p(f_{\rm h})df_{\rm h} \quad (2.33)$$

$$p(H_{\rm ch}) = \int \prod_{A=0}\left[p(t_\star,T_\star)(1-f)\right]\prod_{A=1}\left[p(t_\star,T_\star)f\right]p(f)df. \quad (2.34)$$

The priors and probability functions of relevant parameters are given in Table 2.2, where the ranges for μ and σ are given in $\log_{10}([\rm yr])$. Note that the joint prior of $t_\star$ and $T_\star$ will cancel out when we take the odds ratios, we do not include it in the table.

We obtain the following odds ratios:

$$\frac{p(H_{\rm nat})}{p(H_{\rm nur})} = 210$$
$$\frac{p(H_{\rm nur})}{p(H_{\rm ch})} = 1.4$$
$$\frac{p(H_{\rm nat})}{p(H_{\rm ch})} = 310.$$

where $H_{\rm nur}$, $H_{\rm nat}$, and $H_{\rm ch}$ refer to the Nurture, Nature, and Chance hypotheses, respectively. These odd ratios indicate that the Nature hypothesis, i.e., that stellar obliquity is caused by temperature, is strongly favored over the Nurture hypothesis, i.e., that stellar

obliquity is caused by age. The support for the Nature hypothesis compared to the Chance hypothesis is similarly strong. Regarding the Nurture and Chance hypotheses, there is no preference for one over the other.

We also compute the odds ratios for when f_0, $f_{\rm h}$, and f are each given the hyperprior Beta(1/2,1/2). In this case, we find increased support for the Nurture hypothesis relative to Nature and Chance, and slightly increased support for the Nature hypothesis relative to Chance. However, none of the odds ratios change by more than a factor of 1.5, and thus our general conclusions remain unchanged.

In Appendix 2.6, we perform additional variations in our calculations by removing systems whose alignment state is uncertain and by bootstrapping the data. In both treatments, we find strong evidence for the Nature hypothesis over Nurture and Chance.

2.4.3 Contour plots

In Figure 2.8 we display probability contours between hyperparameters from the equations for the Nurture hypothesis. These are are not plots of the posterior or the likelihood, but they are probabilities calculated from the part of the posterior that does not get cancelled in the odds ratios, and normalized relative to the highest value. The probabilities have been calculated on a grid for each value of f_0, μ, and σ. The plots indicate the values of those hyperparameters that contribute the most to the odds ratio under the Nurture hypothesis and can also give some insight into why the Nurture hypothesis does not have enough evidence to favor it strongly over the Nature and Chance hypotheses.

The structure in the Nurture contour plots shows a continuous distribution of solutions that fit the data with high probability ($\gtrsim 50\%$) relative to the best solution. The highest probability region in the f_0 vs. μ plot suggests that in the Nurture hypothesis, around 75% to 95% of systems start out with an observable misalignment and are realigned by a few Gyr, a timescale similar to the ages of stars in the sample. The f_0 vs. μ plot also shows a region of relatively high probability extending to high values of μ. On the high-μ end, this corresponds to a solution in which $\sim 50\%$ of systems start out misaligned and remain so on very long timescales, which means most of them would still be misaligned today (compare to the observed misaligned fraction of 10/22). Such a solution is equivalent to the Chance hypothesis.

The peaks near $\sigma = 0$ in the σ vs. μ and f_0 vs σ plots indicate a solution with little variation in alignment timescales from system to system. There is also a high probability region in the upper right of the f_0 vs σ plot, with high initial fraction and high σ, showing a solution where alignment timescales vary by many orders of magnitude; systems get

aligned on average after a few Gyr, but there is a lot of variation, and some do not get aligned at all.

The high probability regions in these plots are relatively small compared to the low probability regions. This fine-tuning serves to penalize the Nurture hypothesis when the hyperparameter space is marginalized over, so it does not win out over the Nature hypothesis and only barely has more support than the Chance hypothesis.

To see how much of an effect the large ranges for the hyperpriors of μ and σ in the alignment timescale $t_{\rm a}$ have on the odds ratios, we cut down the priors of μ and σ to $p(\mu)$ =U(6,10) and $p(\sigma)$ =U(0,10). This reduction represents a scenario in which most stars are realigned by 10 Gyr or less and in which there is less variation in the alignment timescale from system to system. The odds ratios then become $p(H_{\rm nat})/p(H_{\rm nur}) = 270$, $p(H_{\rm nur})/p(H_{\rm ch}) = 1.2$, and $p(H_{\rm nat})/p(H_{\rm ch}) = 310$. So this adjustment actually decreases the support for the Nurture hypothesis, but not by much. This suggests that other regions of the original hyperparameter space – such as the region in the top right in the f_0 vs. σ plot – have relatively high-probability solutions that are important to the Nurture hypothesis, and the restricted ranges do not describe the data as well.

The left panel of Figure 2.9 shows the probability histogram for the fraction of hot systems ($f_{\rm h}$) observed to be misaligned under the Nature hypothesis. The right panel of Figure 2.9 shows the fraction (f) of all systems, hot and cool, observed to be misaligned under the Chance hypothesis (blue) and the initial misaligned fraction (f_0) under the Nurture hypothesis with the original hyperprior ranges for μ and σ (orange) and with the reduced hyperprior ranges (green, labeled as "$H_{\rm nur}$ v. 2"), after marginalizing over μ and σ. The curves have been normalized to have the same area. 70% of hot stars are seen to be misaligned with their planets, and 45% of all systems are observed to be misaligned. Under the Nurture hypothesis, 80% of all systems start out misaligned.

2.4.4 Summary

Our calculations strongly favor the Nature hypothesis over both the Nurture hypothesis and the Chance hypothesis. We conclude that of these three possibilities, the obliquities of stars in the data we use are best explained by temperature being the underlying driver.

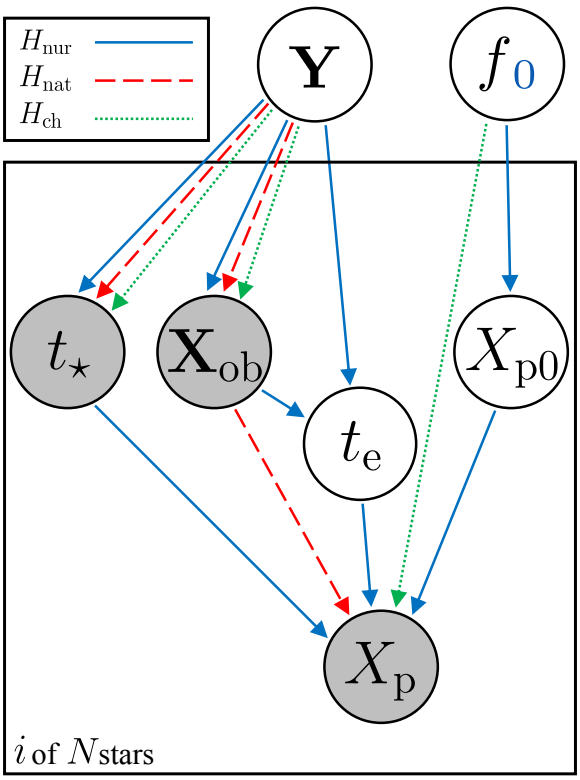

Figure 2.2. Graphical representation of the three hypotheses in the general model, showing possible relationships between parameters under different hypotheses. Rather than show every possible dependence that a model could have, we focus on those that most often become relevant in the applications we examine. Relations under the Nurture hypothesis are shown with a solid blue line, those under the Nature hypothesis with a dashed red line, and those under the Chance hypothesis with a dotted green line. The "i of N stars" indicates that the plate is iterated over each of the N systems in the sample. Gray circles represent observed parameters: the planetary property of interest ($X_{\rm p}$), the stellar age ($t_\star$), and other observed parameters ($\mathbf{X}_{\rm ob}$). White circles are unobserved individual parameters (on the plate) – the initial value of $X_{\rm p}$ ($X_{\rm p0}$) and the evolutionary timescale ($t_{\rm e}$) – and hyperparameters – the fraction of systems with a given value of $X_{\rm p}$ (f), the fraction of systems that start out with a given value of $X_{\rm p}$ (f_0) and other hyperparameters ($\mathbf{Y}$). The hyperparameters f and f_0 are in the same circle because mathematically, they behave the same way in each hypothesis; they are distinguished by the blue subscript, because f_0 occurs in the Nurture hypothesis while the Nature and Chance hypotheses use f. Note that we do not explicitly include the relevant non-observed quantities ($\mathbf{X}_{\rm nob}$), but if we did, it would be in a white circle; it would have each type of arrow pointing from $\mathbf{Y}$ to it and from it to $t_\star$ and $\mathbf{X}_{\rm ob}$, as well as a Nurture hypothesis arrow from it to $t_{\rm e}$.

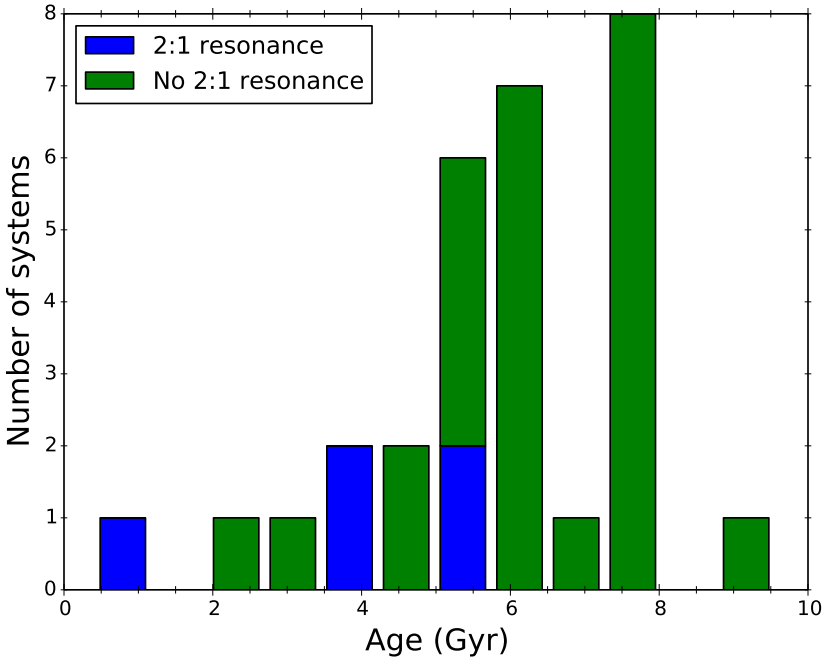

Figure 2.3. Histogram showing the ages of systems in the Koriski & Zucker (2011) sample with 2:1 resonances (blue) and without 2:1 resonances (green). This is the data we use in our analysis in Section 2.3.

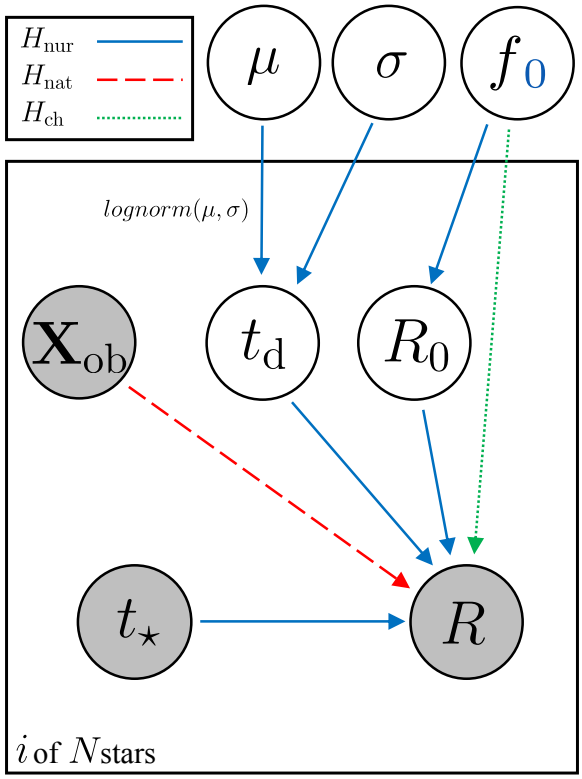

Figure 2.4. Graphical representation of the three hypotheses applied to the case of 2:1 resonances. Relations under the Nurture hypothesis are shown with a solid blue line, those under the Nature hypothesis with a dashed red line, and those under the Chance hypothesis with a dotted green line. The "i of N stars" indicates that the plate is iterated over each of the N systems in the sample. Gray circles represent observed parameters: the current 2:1 resonance state of the system (R), the stellar age ($t_\star$), and other observed parameters that may be used to test the Nature hypothesis ($\mathbf{X}_{\rm ob}$), which we do not test here. White circles are unobserved individual parameters (on the plate) – the initial 2:1 resonance state (R_0) and the 2:1 resonance disruption timescale ($t_{\rm d}$) – and hyperparameters – the mean (μ) and standard deviation (σ) of a log-normal prior for $t_{\rm d}$, the fraction of systems with a 2:1 resonance (f), and the fraction of systems that start out with a 2:1 resonance (f_0). The hyperparameters f and f_0 are in the same circle because mathematically, they behave the same way in each hypothesis; they are distinguished by the blue subscript, because f_0 occurs in the Nurture hypothesis while the Chance hypothesis uses f.

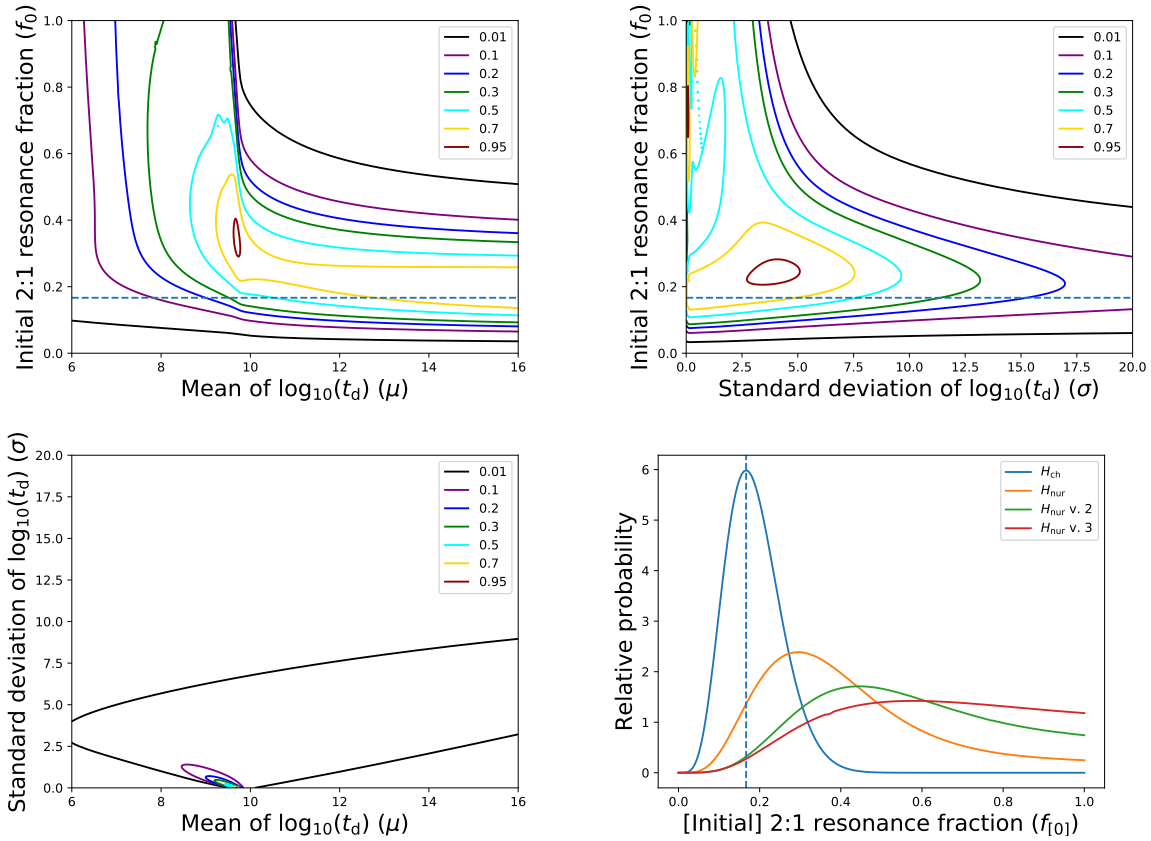

Figure 2.5. Top row and bottom left: Probability contour plots for the Nurture hypothesis for the 2:1 resonances application, showing f_0 vs. μ (top left), f_0 vs. σ (top right), and σ vs. μ (bottom left). Contour levels are 0.01, 0.05, 0.2, 0.5, 0.6, 0.7, 0.8, and 0.95. The observed fraction of systems with a 2:1 resonance (5/30) is shown with a dashed line. Bottom right: Probability histogram of the 2:1 resonance fraction (f) under the Chance hypothesis (blue), and the initial 2:1 resonance fraction (f_0) under the Nurture hypothesis with original hyperprior ranges on μ and σ (orange), with the first reduction of μ and σ hyperprior ranges (green, labeled as "$H_{\rm nur}$ v. 2"), and with the second reduction of μ and σ hyperprior ranges (red, labeled as "$H_{\rm nur}$ v. 3"). The curves have been normalized to have the same area. The observed 2:1 resonance fraction (5/30) is again shown with a dashed line. Note that because resonances are broken over time in the Nurture hypothesis, we do not expect f_0 to match up with the observed 2:1 resonance fraction.

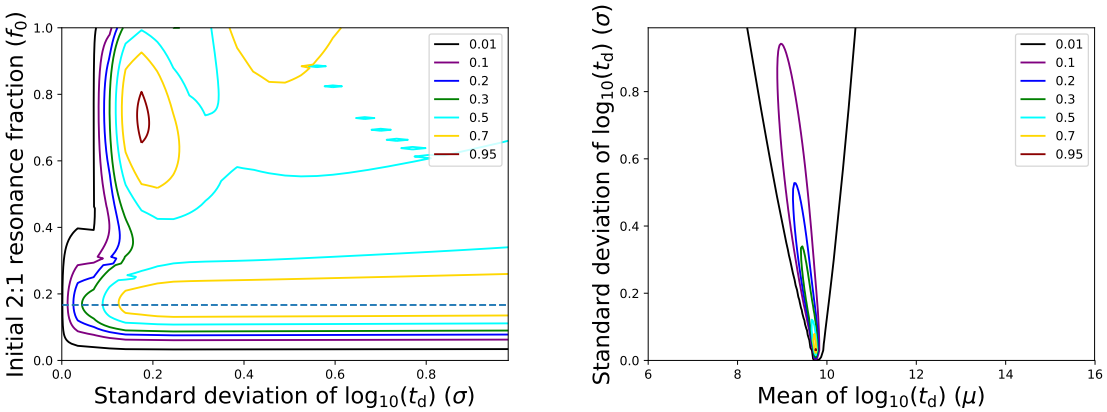

Figure 2.6. Close up views of the region from $\sigma = 0$ to $\sigma = 1$ in the f_0 vs. σ (left) and σ vs. μ (right) probability contour plots for the Nurture hypothesis for the 2:1 resonances application. Contour levels are 0.01, 0.05, 0.2, 0.5, 0.6, 0.7, 0.8, and 0.95. The observed fraction of systems with a 2:1 resonance (5/30) is shown with a dashed line.

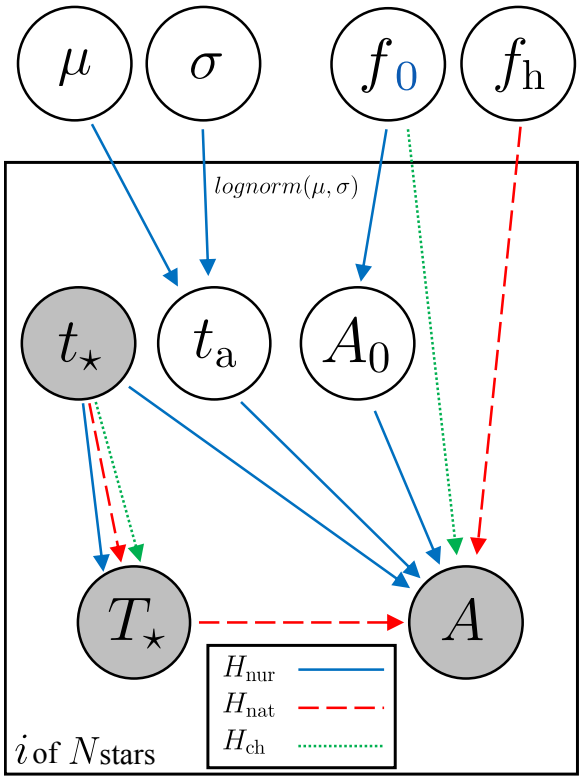

Figure 2.7. Graphical representation of the three hypotheses applied to the case of spin-orbit misalignment. Relations under the Nurture hypothesis are shown with a solid blue line, those under the Nature hypothesis with a dashed red line, and those under the Chance hypothesis with a dotted green line. The "i of N stars" indicates that the plate is iterated over each of the N systems in the sample. Gray circles represent observed parameters: the current alignment state of system (A), the stellar age ($t_\star$), and the stellar temperature ($T_\star$). White circles are unobserved individual parameters (on the plate) – the initial alignment state (A_0) and the alignment timescale (t_a) – and hyperparameters – the mean (μ) and standard deviation (σ) of a log-normal prior for t_a, the fraction of all systems observed to be misaligned (f), the fraction of all systems observed to start out misaligned (f_0), and the misaligned fraction of hot systems (f_h). The hyperparameters f and f_0 are in the same circle because mathematically, they behave the same way in both the Nurture and Chance hypotheses; they are distinguished by the blue subscript, because f_0 occurs in the Nurture hypothesis while the Chance hypothesis uses f.

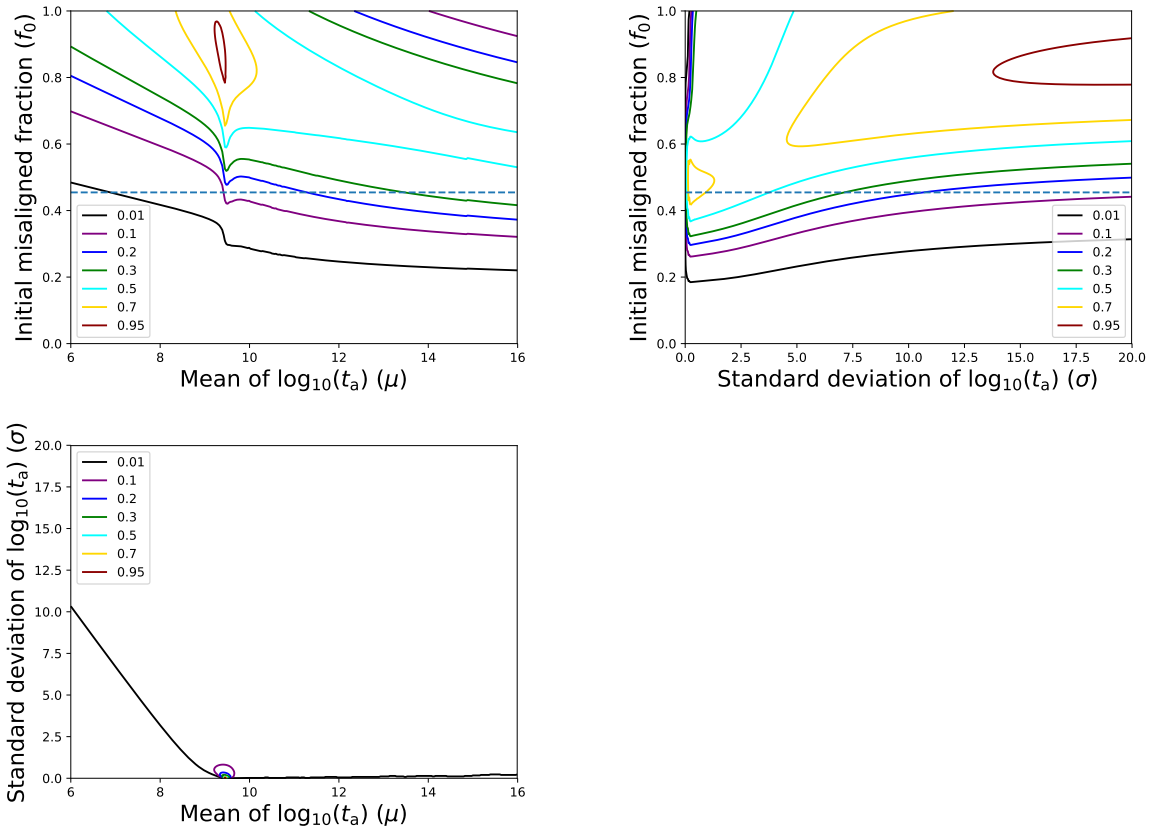

Figure 2.8. Probability contour plots for the Nurture hypothesis in the stellar alignment case, showing μ vs. f_0 (top left), σ vs. μ (top right), and σ vs. f_0 (bottom left). Contour levels are 0.01, 0.05, 0.2, 0.5, 0.6, 0.7, 0.8, and 0.95. The observed fraction of misaligned systems (10/22) is shown with a dashed line. Note that because the Nurture hypothesis involves misaligned systems aligning over time, we do not expect f_0 to match up with the observed misaligned fraction.

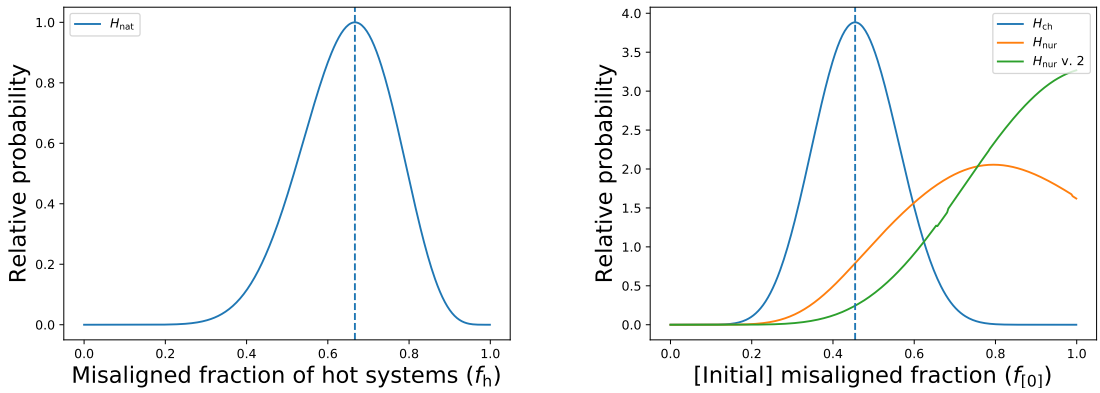

Figure 2.9. Left: Probability histogram of the fraction of hot systems observed to be misaligned under the Nature hypothesis ($f_{\rm h}$). The observed misaligned fraction of hot systems (10/15) is shown with a dashed line. Right: Probability histogram of the fraction (f) of all systems, hot and cool, observed to be misaligned under the Chance hypothesis (blue) and the initial misaligned fraction (f_0) under the Nurture hypothesis with the original hyperprior ranges for μ and σ (orange) and with the reduced hyperprior ranges (green, labeled as "$H_{\rm nur}$ v. 2"), after marginalizing over μ and σ. The curves have been normalized to have the same area. The observed fraction of misaligned systems (10/22) is shown with a dashed line. Because initially misaligned systems are aligned over time in the Nurture hypothesis, we do not expect f_0 to line up with the observed misaligned fraction.

2.5 Do Hot Jupiters Show Evidence for Tidal Circularization?

To look for evidence of tidal circularization, Quinn et al. (2014) analyzed the ages and eccentricities of hot Jupiters – which they defined as having $M_{\rm P} > 0.3\ M_{\rm J}$ and $P < 10$ days – available from the literature at the time. They compared the ages with the expected orbital circularization timescale (see Eqn. 2.36) for each system, assuming a planetary tidal quality factor of $Q_{\rm P} = 10^6$. They found evidence that eccentric orbits circularize over time: systems younger than their circularization timescales tend to be eccentric, and systems older than their circularization timescales tend to be circular.

We present an updated version of Quinn et al. (2014)'s Figure 4 as our Figure 2.10. Although Quinn et al. (2014) did not explicitly list each of the individual systems they included in their sample, they stated that they pulled hot Jupiters and their host star ages from the Extrasolar Planets Encyclopaedia (Schneider et al., 2011a). Using their same mass and period filter with the additional constraint of $M_{\rm P} < 13 M_{\rm J}$, we plot stellar age against circularization timescale, assuming $Q_{\rm P} = 10^6$, for the hot Jupiters for which the stellar and planetary masses, semimajor axis, age, and measured eccentricity are available on the Extrasolar Planets Encyclopaedia, queried on May 28, 2019. The sample contains 130 systems total. The ages of the stars have been determined in a variety of ways, but the most common method is isochrone or evolutionary track fitting. Uncertainties in stellar ages in the sample are typically $\sim 0.5 - 2$ Gyr. In this dataset, 11 systems do not have a measured planetary radius $R_{\rm P}$. When this is the case, we follow Quinn et al. (2014) and estimate $R_{\rm P}$ using the following empirical relation from Weiss et al. (2013):

$$\frac{R_{\rm P}}{R_\oplus} = 2.45 \left(\frac{M_{\rm P}}{M_\oplus}\right)^{-0.039} \left(\frac{F}{\rm erg\ s^{-1}\ cm^{-2}}\right)^{0.094} \tag{2.35}$$

where F represents the time-averaged incident flux the planet receives.

We divide the sample into eccentric systems and circular systems, classifying a given planet as eccentric if it has $e > 0$ at the 3σ level. This is a conservative criterion to only include systems with well measured eccentricities in the eccentric sample, and it means that the circular sample contains both truly low eccentricity planets as well as ambiguous cases. We exclude planets for which the reported eccentricity is $e = 0$ with no error bars, as this indicates assumed circularity in the orbital solution rather than a measured value. For planets for which only an upper limit on the eccentricity is given, we classify it as circular

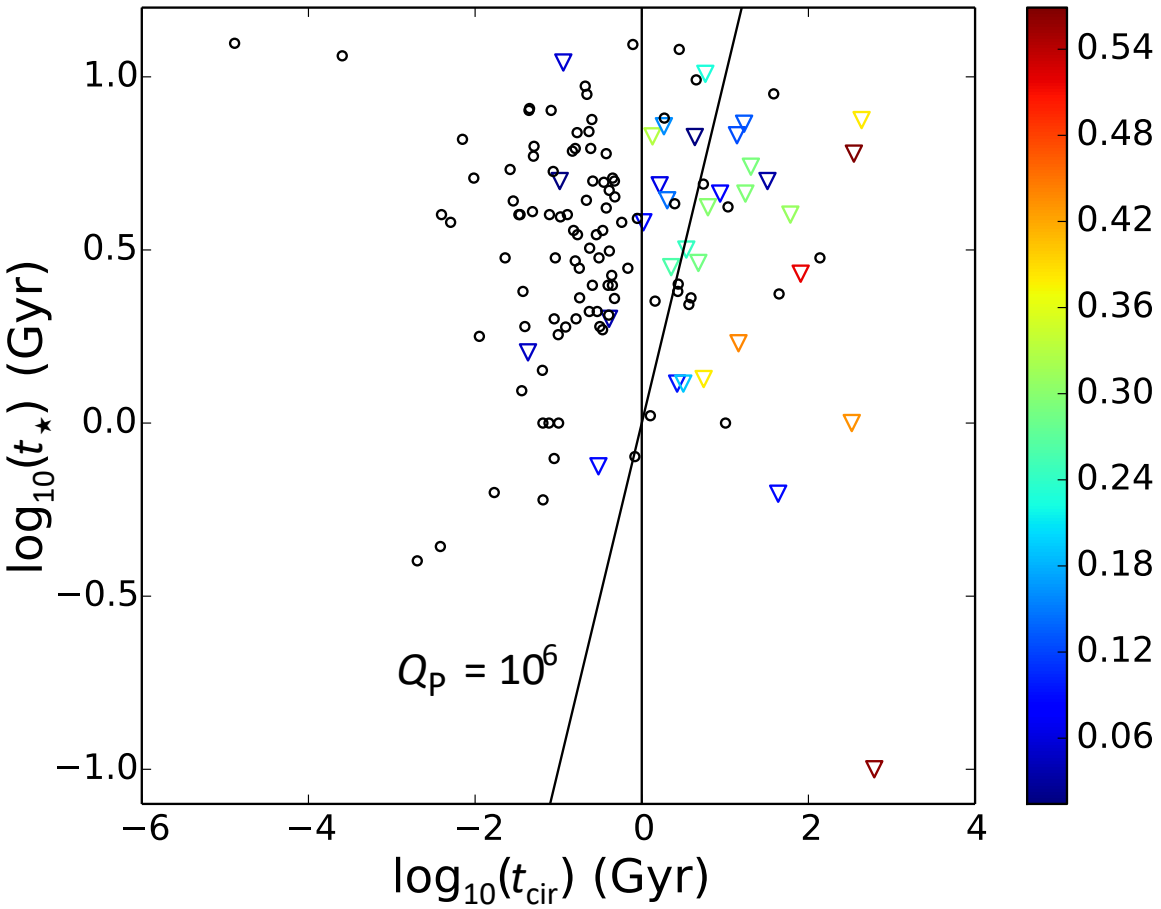

Figure 2.10. Stellar age ($t_\star$) versus circularization timescale ($t_{\rm cir}$) for known hot Jupiters, assuming $Q_{\rm P} = 10^6$. Planets with circular orbits are shown with black circles. Planets on eccentric orbits are shown with triangles colored according to eccentricity, as shown in the color bar on the right. The line of $t_\star = t_{\rm cir}$ is shown with a slanted solid black line. A vertical line is shown as another potential way to divide the sample between primarily eccentric and primarily circular planets.

if $e < 0.1$, and exclude it otherwise. Typical uncertainties in eccentricity in the sample range up to 0.05. Table 2.3 gives the first few lines of our sample data; the full machine-readable table can be accessed at https://doi.org/10.3847/1538-3881/abb536. In Figure 2.10, we over plot the $t_\star = t_{\rm cir}$ line Quinn et al. (2014) used to divide the sample into circular and eccentric planets.

To investigate the difference between the sample subsets on each side of the $t_\star = t_{\rm cir}$ line, Quinn et al. (2014) computed a Kolmogorov-Smirnov (KS) test and obtained $p = 3.3 \times 10^{-5}$, determining with ∼99.997% confidence that they could reject the null

Name	e	$t_\star$ (Gyr)	a (AU)	M_P (M_J)	R_P (R_J)	$M_\star$ ($M_\odot$)	Eccentric? (*)
CoRoT-16 b	0.33±0.1	6.73	0.0618	0.535	1.17	1.098	*
CoRoT-20 b	0.562±0.013	0.1	0.0902	4.24	0.84	1.14	*
CoRoT-23 b	0.16±0.017	7.2	0.0477	2.8	1.08	1.14	*
...							

Table 2.3. Planetary and stellar data for the sample we use in the eccentricities case, giving the planet's name, eccentricity (e) with reported errors used to classify the planet as eccentric or circular, stellar age ($t_\star$) in Gyr, planetary semimajor axis (a) in AU, planetary mass (M_P) in terms of M_J, planetary radius (R_P) in terms of R_J, and stellar mass ($M_\star$) in terms of $M_\odot$. The final column contains an asterisk (*) if the planet is classified as eccentric and no asterisk if the planet is classified as circular. We consider a planet to have an eccentric orbit if it has $e > 0$ at the 3σ level. The full machine-readable version of this table can be accessed at https://doi.org/10.3847/1538-3881/abb536.

hypothesis that the samples came from the same parent population. They found that even when assuming generous errors in eccentricities of 0.1, the KS test rejected the null hypothesis with over 3σ-level confidence. They concluded that planets younger than their cicularization timescales have higher eccentricities.

However, it is not immediately obvious that a $t_\star = t_\mathrm{cir}$ line better divides the sample than a vertical line would, as we show in Figure 2.10. For a sample of planets with similar masses and radii, a vertical line would represent a separation between eccentric vs. circular based only on semimajor axis and would not suggest a dependence on age. There are several possibilities for why we might see a dependence on semi-major axis with no significant age dependence. First, if the sample size has a relatively small age range and tidal circularization is at work, we would expect a noticeable division between planets that were circularized early on and planets that will not be able to circularize over the lifetimes of their stars. Larger radii while planets are young (making it even easier to circularize early on) could enhance this effect. Second, eccentricities are easier to excite at larger semi-major axes via planet-disk interactions (e.g., Duffell & Chiang 2015), planet-planet scattering (e.g., Petrovich et al. 2014), and/or forcing from an outer companion. Although many of the eccentricities are too high for these mechanisms or the planets lack the necessary nearby companions (see Dawson & Johnson 2018 and references therein), the qualitative trend in e vs. a is consistent.

We perform a KS test on the planets to the right and left of the $t_\star = t_\mathrm{cir}$ line using the updated hot Jupiter data, and obtain a p-value of 2.6×10^{-6}. This means we can reject the null hypothesis that the subsamples come from the same parent distribution with 99.9997% confidence, in agreement with Quinn et al. (2014)'s results. Next we perform a

KS test for the subsamples on either side of the vertical line we added in Figure 2.10. We obtain a p-value of 1.3×10^{-9} and can reject the null hypothesis with a confidence level of 99.9999999%. The nature of the KS test is such that we cannot compare the results we have obtained here to determine which line does a better job of dividing the sample. This is because, among other reasons, it is difficult to calculate accurate probabilities so far out on the tails of probability distributions because assumptions such as the lack of systematics break down; this renders the difference between our calculated p-values essentially meaningless. Each test is to determine whether or not we can confidently reject the null hypothesis that the data on each side of the line come from the same parent distribution. In both cases, we can reject the null hypothesis with a high level of confidence, demonstrating that there are multiple ways to effectively divide the data into primarily circular and primarily eccentric planets.

In Figure 2.11, we plot eccentricity versus semimajor axis for the planets in the sample. Eccentric planets are marked with a triangle and circular planets with a circle, but the marker colors now indicate the system's age. Clearly, planets at larger semimajor axes tend to be more eccentric than those closer in. However, the plot shows a tendency for younger systems to have higher eccentricities (we see blue triangles interior to the red triangles), supporting an additional dependence on age. We also display lines of constant $a(1-e^2)$, which is the final semimajor axis the planets get circularized to, and of constant periapse[1] $a(1-e)$, for the blue and the red points. It appears that the outer envelopes of red and blue points can be well traced by separate curves, indicating a possible age dependence. Because stars of different masses have different lifetimes, this could instead be a trend in stellar mass or temperature, but we do not see the same trend when we color the points according to stellar mass or temperature.

Here we seek to determine whether the available data truly exhibit a trend of eccentricity with stellar age or are better explained by a correlation with semimajor axis only. We derive the relevant equations for each hypothesis in Section 2.5.1, present our results in Section 2.5.2, show and discuss contour plots of hyperparameters in Section 2.5.3, then briefly summarize in Section 2.5.4. We show a graphical representation of the model for this case in Figure 2.12.

[1]Contrary to expectation, the periapse lines seem to follow the outer envelope of data points better than the final semimajor axis lines, even though tidal circularization timescales are thought to scale with $a(1-e^2)$ at low eccentricities, e.g. Adams & Laughlin 2006; Socrates et al. 2012.

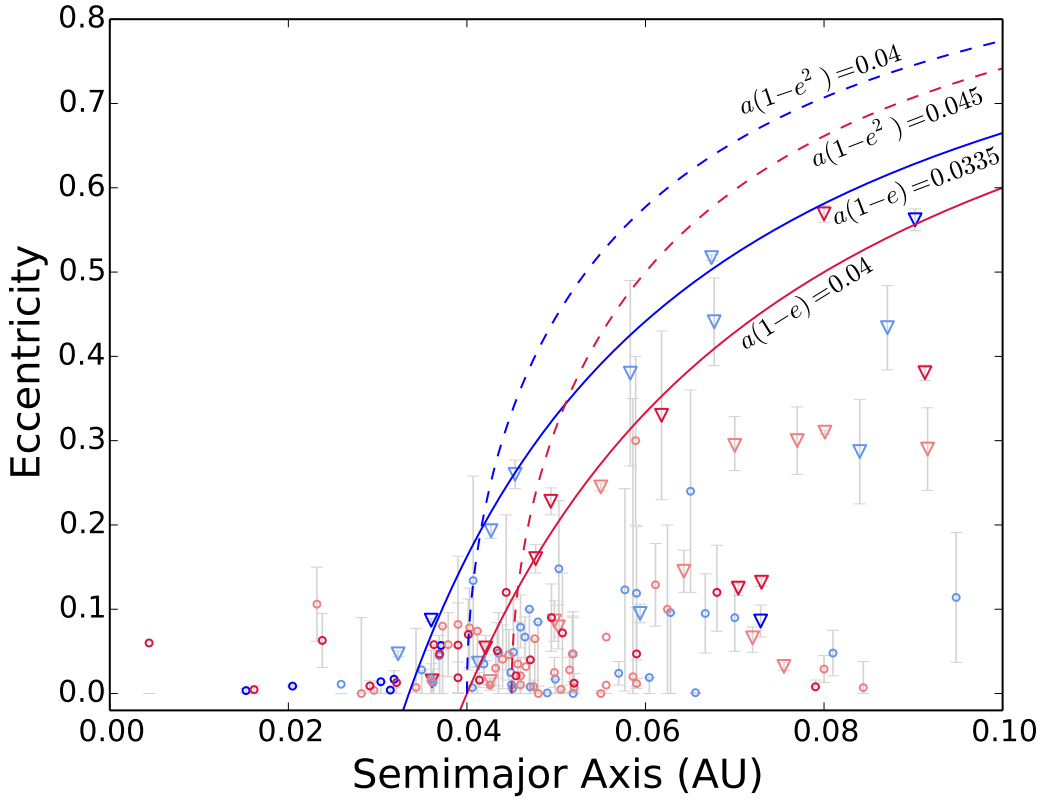

Figure 2.11. Eccentricity versus semimajor axis for known hot Jupiters. Planets with circular orbits are shown as circles, and planets on eccentric orbits are shown as triangles. The marker color indicates age: blue is for $t_\star < 1$ Gyr, light blue is for 1 Gyr $\leq t_\star < 3$ Gyr, light red is for 3 Gyr $\leq t_\star < 6$ Gyr, and red is for 6 Gyr $\leq t_\star$. The dashed blue and red curves are lines of constant $a(1-e^2)$ for the blue and red points, respectively. The solid blue and red curves are lines of constant $a(1-e)$ for the blue and red points, respectively.

2.5.1 Equations for each hypothesis

2.5.1.1 Hypothesis 1: Nurture (Age-driven)

In this application, the property of interest is whether the planet's orbit is eccentric. Similar to the alignment case, we are not concerned with the specific value of the eccentricity, but instead classify a given planet as eccentric if it has $e > 0$ at the 3σ level. We represent this classification with E, which is 1 if the orbit is eccentric and 0 if it is circular. The initial eccentricity state is designated as E_0 and behaves in the same way.

In the Nurture hypothesis, we compare the star's age to the planet's circularization timescale, $t_{\rm cir}$. This timescale depends on several other system properties, most strongly the planetary radius and semimajor axis, and the systems we are looking at here are varied

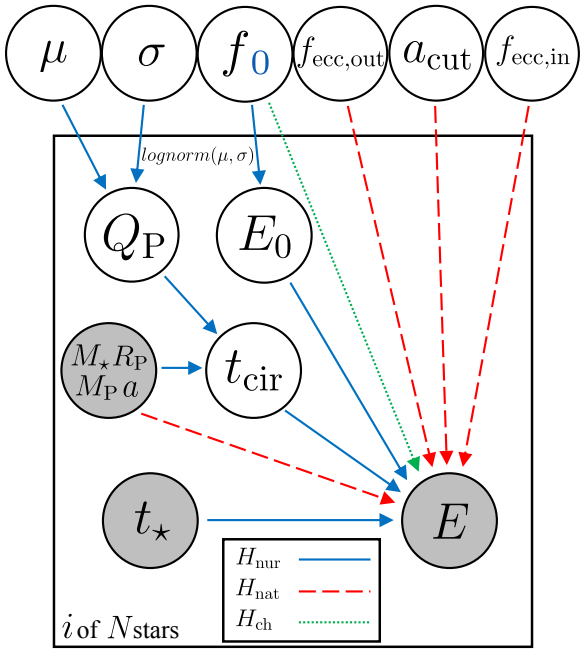

Figure 2.12. Graphical representation of the three hypotheses applied to the case of eccentricities. Relations under the Nurture hypothesis are shown with a solid blue line, those under the Nature hypothesis with a dashed red line, and those under the Chance hypothesis with a dotted green line. The "i of N stars" indicates that the plate is iterated over each of the N systems in the sample. Gray circles represent observed parameters: the current eccentricity state of the system (E), the stellar age ($t_\star$), the stellar mass ($M_\star$), the planetary mass ($M_{\rm P}$), the planetary radius ($R_{\rm P}$), and the semimajor axis (a). White circles are unobserved individual parameters (on the plate) – the initial eccentricity state (E_0), the circularization timescale ($t_{\rm cir}$), and the planetary tidal quality factor ($Q_{\rm P}$) – and hyperparameters – the mean (μ) and standard deviation (σ) of a log-normal prior for $Q_{\rm P}$, the fraction of eccentric systems (f), the initial fraction of eccentric systems (f_0), the semimajor axis cutoff ($a_{\rm cut}$), the fraction of eccentric systems beyond $a_{\rm cut}$ ($f_{\rm ecc,out}$), and the fraction of eccentric systems that remain eccentric within $a_{\rm cut}$ ($f_{\rm ecc,in}$). The hyperparameters f and f_0 are in the same circle because mathematically, they behave the same way in both the Nurture and Chance hypotheses; they are distinguished by the blue subscript, because f_0 occurs in the Nurture hypothesis while the Chance hypothesis uses f.

enough that we cannot discount the dependence on planet properties as we do in the alignment case. The circularization timescale, i.e. the decay rate of orbital eccentricity, is given as follows:

$$t_{\rm cir} = \frac{Q_{\rm P} M_{\rm P} a^{6.5}}{6\pi k_{\rm L} G^{0.5} M_\star^{1.5} R_{\rm P}^5} \tag{2.36}$$

where $Q_{\rm P}$ is the tidal quality factor, $M_{\rm P}$ is the mass of the planet, a is the semimajor axis, $M_\star$ is the mass of the star, $R_{\rm P}$ is the radius of the planet, and $k_{\rm L}$ is the Love number which is generally taken to be 0.38 (Socrates et al., 2012). This formulation is an approximation for low eccentricities, which is appropriate here because all of the systems

have $e < 0.6$ and most have $e < 0.25$.

The tidal quality factor $Q_{\rm P}$ is related to planet's tidal dissipation efficiency; it is very poorly known and probably depends on the planet's composition, internal structure, rotation, and temperature, as well as the forcing frequency it experiences (Socrates et al., 2012). For Jupiter, it has been constrained to $6 \times 10^4 < Q_{\rm J} < 2 \times 10^6$ (Yoder & Peale, 1981). $Q_{\rm P}$ is a component of $\mathbf{X}_{\rm nob}$ and is the primary source of uncertainty in $t_{\rm cir}$ for a given planet. To account for our lack of knowledge about this property, we assume the population of $Q_{\rm P}$ is a log-normal distribution with unknown mean μ and standard deviation σ. These latter two variables are hyperparameters. We give μ a log-uniform hyperprior of U(2,8), and we give σ a log-uniform hyperprior of U(0,5), both in $\log_{10}$ space. Some planets in our sample may have tidal quality factors similar to that of Jupiter, but some may be quite different. These hyperprior ranges for μ and σ allow for both possibilities by comfortably enclosing and extending beyond the range of possible $Q_{\rm P}$ found for Jupiter. Note that the hyperprior on μ is uninformative, while the hyperprior on σ is not and is weighted towards large values of σ. However, this is appropriate here since we expect a range of orders of magnitude in the tidal quality factor of hot Jupiters.

The other parameters in the calculation of $t_{\rm cir}$ – $M_{\rm P}$, $M_\star$, $R_{\rm P}$, and a – are measured data and thus are contained in $\mathbf{X}_{\rm ob}$. We assume the joint prior on $t_\star$, $M_{\rm P}$, $M_\star$, $R_{\rm P}$, and a is independent of other parameters, both observed and not observed, as well as hyperparameters, and we do not consider any unobserved parameters other than $Q_{\rm P}$. Then, from Eqn. 2.8, substituting in the above parameters and rearranging gives

$$
\begin{aligned}
&p(E, t_\star, a, R_{\rm P}, M_{\rm P}, M_\star | f_0, \mu, \sigma) \\
&\quad = \begin{cases}
p(t_\star, a, R_{\rm P}, M_{\rm P}, M_\star) & \\
\quad \times \int \left[1 - f_0 + f_0 \int_0^{t_\star} p(t_{\rm cir} | a, R_{\rm P}, M_{\rm P}, M_\star, Q_{\rm P}, \mu, \sigma) dt_{\rm cir}\right] & \\
\quad \times p(Q_{\rm P} | \mu, \sigma) dQ_{\rm P} & , E = 0 \\
p(t_\star, a, R_{\rm P}, M_{\rm P}, M_\star) & \\
\quad \times f_0 \int\int_{t_\star}^{\infty} p(t_{\rm cir} | a, R_{\rm P}, M_{\rm P}, M_\star, Q_{\rm P}, \mu, \sigma) dt_{\rm cir} & \\
\quad \times p(Q_{\rm P} | \mu, \sigma) dQ_{\rm P} & , E = 1.
\end{cases}
\end{aligned}
\tag{2.37}
$$

where f_0 is the fraction of systems that begin with detectable eccentric orbits. We assign to f_0 a uniform hyperprior from 0 to 1. We note that for f_0, the uninformative hyperprior is Beta(1/2,1/2); we will also compute odds ratios using this hyperprior, and compare to the results from the uniform hyperprior. Since $p(t_\star, a, R_{\rm P}, M_{\rm P}, M_\star)$ is independent of

unobserved system parameters, it will cancel out when the odds ratios are calculated.

Since the primary uncertainty in a given planet's $t_{\rm cir}$ comes from its tidal quality factor, we wish to reparameterize the above equation in terms of $Q_{\rm P}$. We treat the prior of $t_{\rm cir}$ itself, $p(t_{\rm cir})$, as a Delta function centered at the value for $t_{\rm cir}$ given by Eqn. 2.36. This means the integrals over $t_{\rm cir}$ in Eqn. 2.37 are either 1 or 0 depending on whether $t_{\rm cir}$ from Eqn. 2.36 is greater than or less than $t_\star$. We use Eqn. 2.36 to write $Q_{\rm P}$ in terms of $t_{\rm cir}$ and introduce $Q_{\rm P,crit}$ as the value of $Q_{\rm P}$ such that $t_{\rm cir} = t_\star$ for a given planet. We can then adjust the limits of integration over $Q_{\rm P}$ and obtain the following statements:

$$p(E, t_\star, a, R_{\rm P}, M_{\rm P}, M_\star | f_0, \mu, \sigma) = \begin{cases} p(t_\star, a, R_{\rm P}, M_{\rm P}, M_\star) \\ \times \left[1 - f_0 + f_0 \int_0^{Q_{\rm P,crit}} p(Q_{\rm P}|\mu, \sigma) dQ_{\rm P}\right], & E = 0 \\ p(t_\star, a, R_{\rm P}, M_{\rm P}, M_\star) f_0 \int_{Q_{\rm P,crit}}^{\infty} p(Q_{\rm P}|\mu, \sigma) dQ_{\rm P}, & E = 1. \end{cases} \tag{2.38}$$

2.5.1.2 Hypothesis 2: Nature (Driven by inherent system properties)

In the Nature hypothesis, we test the idea that a dependence on semimajor axis – with no contribution from stellar age – best explains the data, due to a relatively small span of stellar ages in the sample and/or eccentricities at larger semimajor axes being easier to excite and retain.

We introduce the parameter $a_{\rm cut}$, the cut-off semimajor axis, within which a planet has a circular orbit and beyond which a planet may acquire and/or retain an eccentric orbit. We treat $a_{\rm cut}$ as a hyperparameter, i.e. a universal semimajor axis cutoff for eccentricity. Thus $a_{\rm cut}$ behaves in much the same way as the 6250 K temperature division does in the obliquities case. The primary difference is that we do not here have a well-defined cutoff value, so we must marginalize over $a_{\rm cut}$. We give it a uniform prior from 0 to 0.1 AU, as this encompasses the range of semimajor axes in our sample. Introducing $a_{\rm cut}$ and the other parameters into Eqn. 2.9 gives

$$p(E, t_\star, a, R_{\rm P}, M_{\rm P}, M_\star | a_{\rm cut}) = p(E|a, a_{\rm cut}) p(t_\star, a, R_{\rm P}, M_{\rm P}, M_\star) \tag{2.39}$$

where we have noted that a is the only component of $\mathbf{X}_{\rm ob}$ on which E depends, and there are no $\mathbf{X}_{\rm nob}$.

If a planet is outside the semimajor axis cutoff, its orbit may be circular or eccentric. We introduce the additional hyperparameter $f_{\rm ecc,out}$, which we give a hyperprior of U(0,1),

to represent the fraction of planets with detectably eccentric orbits beyond $a_{\rm cut}$. So for planets outside of $a_{\rm cut}$,

$$p(E|a \geq a_{\rm cut}, f_{\rm ecc,out}) = \begin{cases} 1 - f_{\rm ecc,out} & , E = 0 \\ f_{\rm ecc,out} & , E = 1. \end{cases} \tag{2.40}$$

Under the Nature hypothesis, a planet within the semimajor axis cutoff must have a circular orbit. Thus for planets within $a_{\rm cut}$ we use:

$$p(E|a < a_{\rm cut}) = \begin{cases} 1 & , E = 0 \\ 0 & , E = 1. \end{cases} \tag{2.41}$$

If a planet is within the semimajor axis cutoff, its orbit should be circular. However, there may be some exceptions to this rule, such as planets whose orbits are influenced by an additional body that drives up their eccentricity. Accordingly, we will also consider a special case of this hypothesis which includes a fraction of eccentric systems, $f_{\rm ecc,in}$, that remain eccentric within $a_{\rm cut}$. Note that $f_{\rm ecc,in}$ is not a fraction of all the systems, but rather of all systems with detectably eccentric orbits, $f_{\rm ecc,out}$. So for planets within $a_{\rm cut}$, in this special case,

$$p(E|a < a_{\rm cut}, f_{\rm ecc,out}, f_{\rm ecc,in}) = \begin{cases} (1 - f_{\rm ecc,in}) f_{\rm ecc,out} + (1 - f_{\rm ecc,out}) & , E = 0 \\ f_{\rm ecc,in} f_{\rm ecc,out} & , E = 1. \end{cases} \tag{2.42}$$

We assign $f_{\rm ecc,in}$ a hyperprior of U(0,1). Note that $f_{\rm ecc,in}$ is a hyperparameter. We also note that for both $f_{\rm ecc,in}$ and $f_{\rm ecc,out}$, the true uninformative hyperprior is Beta(1/2,1/2); we will also compute odds ratios using this hyperprior on both $f_{\rm ecc,in}$ and $f_{\rm ecc,out}$ and compare to the results from the uniform hyperprior.

2.5.1.3 Hypothesis 3: Chance

From Eqn. 2.11,

$$p(E, t_\star, a, R_{\rm P}, M_{\rm P}, M_\star | f) = \begin{cases} p(t_\star, a, R_{\rm P}, M_{\rm P}, M_\star)(1 - f) & , E = 0 \\ p(t_\star, a, R_{\rm P}, M_{\rm P}, M_\star) f & , E = 1 \end{cases} \tag{2.43}$$

as there are no components of $\mathbf{X}_{\rm nob}$ or other hyperparameters we consider here. f is the fraction of detectably eccentric systems, which we give a uniform hyperprior from 0 to 1.

Parameter		Prior or Probability Function
Planetary tidal quality factor $(\log_{10}(Q_{\rm P})\|\mu,\sigma)$		$\frac{1}{\sqrt{2\pi\sigma^2}}\exp\left(\frac{-(\log_{10}(Q_{\rm P})-\mu)^2}{2\sigma^2}\right)$
Mean of $\log_{10}(Q_{\rm P})$ (μ)		U(2,8)
Standard deviation of $\log_{10}(Q_{\rm P})$ (σ)		U(0,5)
Initial fraction of eccentric systems (f_0)		U(0,1)
Semimajor axis cutoff $(a_{\rm cut})$		U(0,0.1)
Fraction of eccentric systems beyond $a_{\rm cut}$ $(f_{\rm ecc,out})$		U(0,1)
Fraction of eccentric systems within $a_{\rm cut}$ $(f_{\rm ecc,in})$		U(0,1)
Fraction of eccentric systems (f)		U(0,1)
Eccentricity state	$E=0\|a\geq a_{\rm cut}, f_{\rm ecc,out}$	$1-f_{\rm ecc,out}$
	$E=1\|a\geq a_{\rm cut}, f_{\rm ecc,out}$	$f_{\rm ecc,out}$
	$E=0\|a<a_{\rm cut}$	1
	$E=1\|a<a_{\rm cut}$	0

Table 2.4. Priors and probability functions of relevant parameters for the eccentricities case.

We will also compare the results to those obtained using a hyperprior of Beta(1/2,1/2).

2.5.2 Results

We apply Eqn. 2.37 for the Nurture hypothesis, Eqn. 2.39 for the Nature hypothesis, and Eqn. 2.43 for the Chance hypothesis to the observed sample. The complete equations for each hypothesis are

$$\begin{aligned}
p(H_{\rm nur}) = &\iiint \prod_{E=0} [p(t_\star,a,R_{\rm P},M_{\rm P},M_\star)\left(1-f_0+f_0\int_0^{Q_{\rm P,crit}} p(Q_{\rm P}|\mu,\sigma)dQ_{\rm P}\right)] \\
&\times \prod_{E=1} [p(t_\star,a,R_{\rm P},M_{\rm P},M_\star)f_0\int_{Q_{\rm P,crit}}^{\infty} p(Q_{\rm P}|\mu,\sigma)dQ_{\rm P}] \\
&\times p(\mu)p(\sigma)p(f_0)d\mu d\sigma df_0 \qquad (2.44)\\
p(H_{\rm nat}) = &\iiint \prod_{E=0} [p(E=0|a,a_{\rm cut},f_{\rm ecc,out},f_{\rm ecc,in})p(t_\star,a,R_{\rm P},M_{\rm P},M_\star)] \\
&\times \prod_{E=1} [p(E=1|a,a_{\rm cut},f_{\rm ecc,out},f_{\rm ecc,in})p(t_\star,a,R_{\rm P},M_{\rm P},M_\star)] \\
&\times p(a_{\rm cut})p(f_{\rm ecc,out})p(f_{\rm ecc,in})da_{\rm cut}df_{\rm ecc,out}df_{\rm ecc,in} \qquad (2.45)\\
p(H_{\rm ch}) = &\int \prod_{E=0} [p(t_\star,a,R_{\rm P},M_{\rm P},M_\star)(1-f)] \prod_{E=1} [p(t_\star,a,R_{\rm P},M_{\rm P},M_\star)f]\,p(f)df. \qquad (2.46)
\end{aligned}$$

Priors and probability functions of relevant parameters are summarized in Table 2.4. Note that the prior $p(t_\star,a,R_{\rm P},M_{\rm P},M_\star)$ will cancel out when we take the odds ratios, so we do not include it in the table.

We obtain the following odds ratios:

$$\frac{p(H_{\rm nur})}{p(H_{\rm nat})} = 1.3 \times 10^8$$
$$\frac{p(H_{\rm nur})}{p(H_{\rm ch})} = 1.5 \times 10^8$$
$$\frac{p(H_{\rm nat})}{p(H_{\rm ch})} = 1.1.$$

These odd ratios indicate that the Nurture hypothesis, i.e. a correlation of eccentricity with age, is significantly favored over the Nature hypothesis, i.e. a correlation of eccentricity with semimajor axis. The Nurture hypothesis is also very strongly favored over the Chance hypothesis. There is nearly equal support for the Nature and Chance hypotheses; this is probably due to a few eccentric planets at small semimajor axes that essentially spoil the general trend of eccentricity with semimajor axis that can be seen in Figure 2.11. When we fix $a_{\rm cut}$ to be 0.03 AU – just inside the eccentric planet with the smallest semimajor axis – the odds ratio of Nature to Chance is 22, which is moderately in favor of the Nature hypothesis.

We also compute the odds ratios with f_0, $f_{\rm ecc,out}$, and f assigned uninformative hyperpriors of Beta(1/2,1/2). This results in an increase by roughly a factor of 2 in the support of the Nurture hypothesis relative to Nature and Chance. The Nature vs. Chance ratio is essentially the same. Thus the Nurture hypothesis is still the strong winner, and our overall conclusion is unchanged.

In the special case in which we include $f_{\rm ecc,in}$ in the Nature hypothesis, we obtain odds ratios of:

$$\frac{p(H_{\rm nur})}{p(H_{\rm nat})} = 5.5 \times 10^4$$
$$\frac{p(H_{\rm nur})}{p(H_{\rm ch})} = 1.5 \times 10^8$$
$$\frac{p(H_{\rm nat})}{p(H_{\rm ch})} = 2.6 \times 10^3.$$

Thus, the allowance of a few eccentric planets within the semimajor axis cutoff increases support for the Nature hypothesis by several orders of magnitude, but despite this, the Nurture hypothesis is still very strongly favored. It may be expected that the value of $f_{\rm ecc,in}$ would be rather small; however, we found that assigning $f_{\rm ecc,in}$ a logarithmic prior to reflect the unknown scale of $f_{\rm ecc,in}$, while it increased support for Nature by a factor of

a few, still did not allow the Nature hypothesis to be supported over Nurture.

We found that assigning f_0, $f_{\rm ecc,out}$, $f_{\rm ecc,in}$, and f hyperpriors of Beta(1/2,1/2) decreased the support for the Nature hypothesis relative to Nurture and Chance by roughly a factor of 2, and decreased support for Nurture relative to Chance also by roughly a factor of 2. This again leaves Nurture as the strong winner and does not change our overall conclusions.

In Appendix 2.6, we perform additional variations in our calculations by removing systems with highly uncertain ages or eccentricities and by bootstrapping the data. We find that in both of these cases, the Nurture hypothesis is still very strongly favored over both Nature and Chance.

2.5.3 Contour Plots

In Figure 2.13, we display probability contours between the hyperparameters in the Nurture hypothesis, specifically, the initial fraction of eccentric systems f_0, and the mean μ and standard deviation σ of the log-normal prior of the tidal quality factor $Q_{\rm P}$. These plots indicate that most systems start out eccentric (high f_0) and have tidal quality factors of around 10^6. The peaks around $\sigma = 1$ suggest there is a moderate amount of variation in tidal quality factors among the planets.

Figure 2.14 shows probability contours between the hyperparameters in the Nature hypothesis, the semimajor axis cutoff $a_{\rm cut}$ and the fraction of eccentric systems $f_{\rm ecc,out}$ outside of $a_{\rm cut}$ when we do not include $f_{\rm ecc,in}$. This plot indicates a fraction of eccentric systems of around 30%, very close to what is observed, and a semimajor axis cutoff of around 0.03 AU.

The panels in Figure 2.15 display contours between $f_{\rm ecc,out}$, $a_{\rm cut}$, and the fraction $f_{\rm ecc,in}$ of eccentric systems within $a_{\rm cut}$ for the special case in which $f_{\rm ecc,in}$ is included. The contours are not smooth because of the limited size of the observed sample. These plots indicate that the best solution, under the Nature hypothesis in this special case, is a semimajor axis cutoff of ~ 0.07 AU, with $\sim 60\%$ of all planets starting out on eccentric orbits and $\sim 20\%$ remaining eccentric within $a_{\rm cut}$.

The small irregularities in the upper right panel of Figure 2.15 are low probability regions driven by close-in eccentric systems and more distant circular system, i.e. systems that do not fit the general pattern described by the Nature hypothesis. Removing them from the sample decreases the Nurture vs. Nature odds ratio by a couple orders of magnitude, but the Nurture hypothesis still has strong support.

In Figure 2.16 we display probability histograms for f in the Chance hypothesis, f_0

in the Nurture hypothesis, $f_{\rm ecc,out}$ in the Nature hypothesis, and $f_{\rm ecc,out}$ and $f_{\rm ecc,in}$ in the Nature hypothesis where we have included $f_{\rm ecc,in}$. The curves have been normalized to have the same area, and the observed eccentric fraction (33/130) is shown with a dashed line. Under the Nurture hypothesis, $\sim$90% of planets form on eccentric orbits. Under the Nature hypothesis with no $f_{\rm ecc,in}$, the fraction of eccentric systems outside the semimajor axis cutoff $a_{\rm cut}$ ($f_{\rm ecc,out}$) is only slightly more than the overall observed fraction of eccentric systems. The contours in Figure 2.14 indicate that this version of the Nature hypothesis favors a value for $a_{\rm cut}$ of around 0.03 AU, just inside the closest-in eccentric planet. There are only a few planets within 0.03 AU (see Figure 2.11), so $f_{\rm ecc,out}$ is close to the observed fraction. When $f_{\rm ecc,in}$ is included in the Nature hypothesis, a semimajor axis cutoff of around 0.07 AU is favored, as seen in Figure 2.15. Most of the sample is within this value, which leads to $f_{\rm ecc,in}$ being near the observed eccentric fraction, and the majority of planets in the sample beyond 0.07 AU are eccentric, giving $f_{\rm ecc,out}$ a higher value in this case.

2.5.4 Summary

In summary, we find very strong support for the hypothesis that eccentric hot Jupiters tend to be younger than circular hot Jupiters, compared to the hypothesis that eccentricity is due to semimajor axis or a chance relation. This result supports the theory that hot Jupiter orbits are circularized over time, consistent with high-eccentricity migration. In the future, we can improve our assessment by incorporating measurement uncertainties on the observed system parameters. We note in particular that the strong dependence of $t_{\rm cir}$ on a and $R_{\rm P}$ can inflate a measurement uncertainty of tens of percent into a factor of 2-10, which will be non-negligible in the calculation of $t_{\rm cir}$.

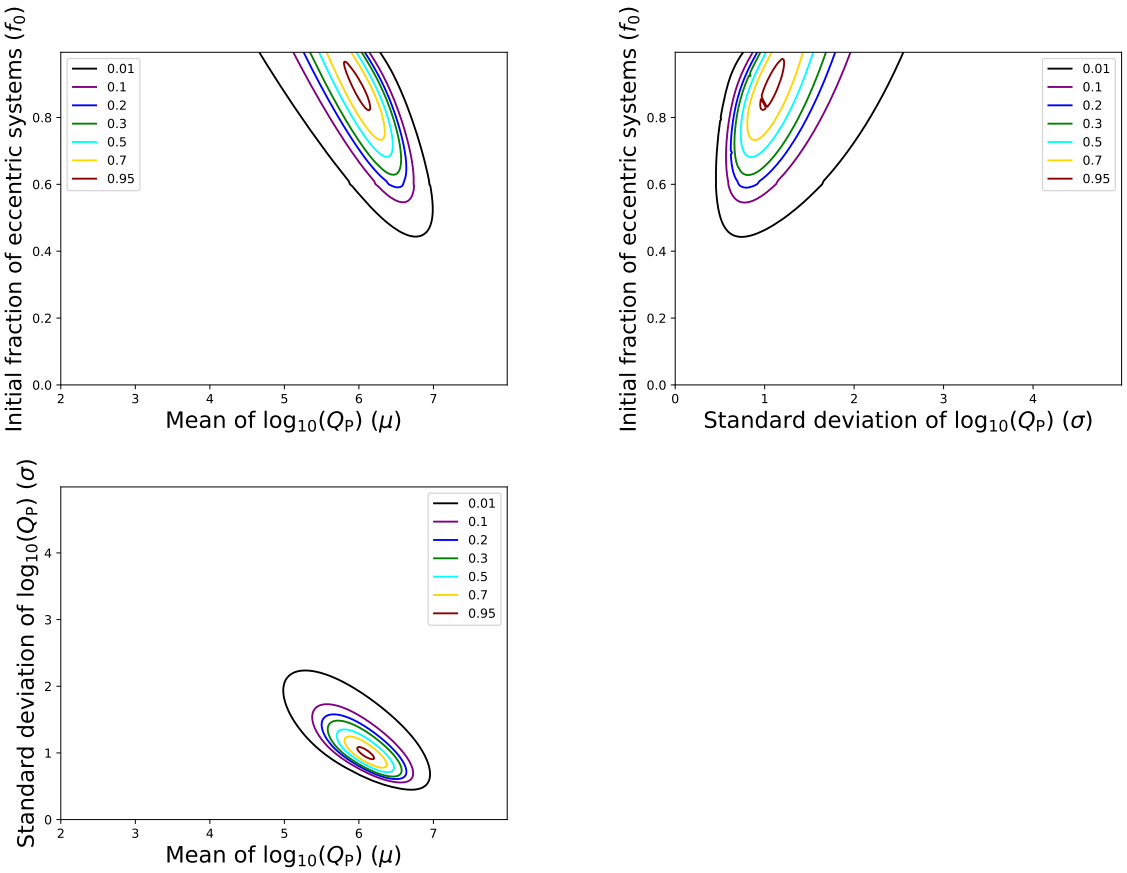

Figure 2.13. Probability contour plots for the Nurture hypothesis in the eccentricities case, showing f_0 vs. μ (top left), f_0 vs. σ (top right), and σ vs. μ (bottom left), where μ and σ are the mean and standard deviation, respectively, of a log-normal prior on Q_P. Contour levels are 0.01, 0.05, 0.2, 0.5, 0.6, 0.7, 0.8, and 0.95.

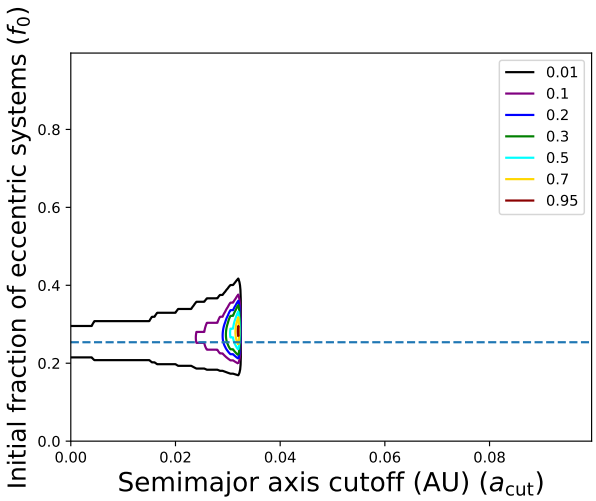

Figure 2.14. Probability contour plot for the Nature hypothesis in the eccentricities case showing $f_{\mathrm{ecc,out}}$ vs. a_{cut} in the case where we do not include the $f_{\mathrm{ecc,in}}$ parameter. Contour levels are 0.01, 0.05, 0.2, 0.5, 0.6, 0.7, 0.8, and 0.95. The observed fraction of detectably eccentric systems is shown as a blue dashed line.

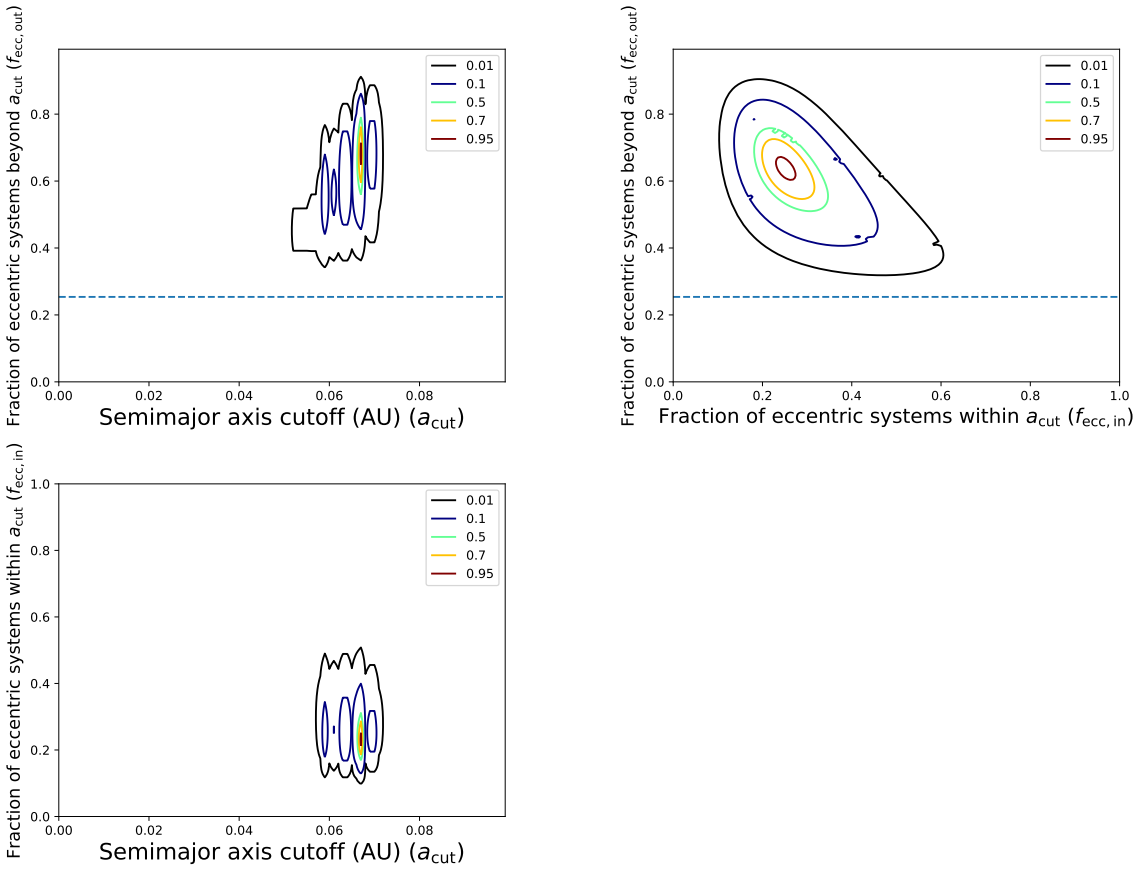

Figure 2.15. Probability contour plots for the Nature hypothesis in the eccentricities case where $f_{\mathrm{ecc,in}}$ is included, showing $f_{\mathrm{ecc,out}}$ vs. a_{cut} (top left) $f_{\mathrm{ecc,out}}$ vs. $f_{\mathrm{ecc,in}}$ (top right), and $f_{\mathrm{ecc,in}}$ vs. a_{cut} (bottom left). Contour levels are 0.01, 0.05, 0.2, 0.5, 0.6, 0.7, 0.8, and 0.95. The observed fraction of detectably eccentric systems is shown as a blue dashed line in the upper left and upper right plots.

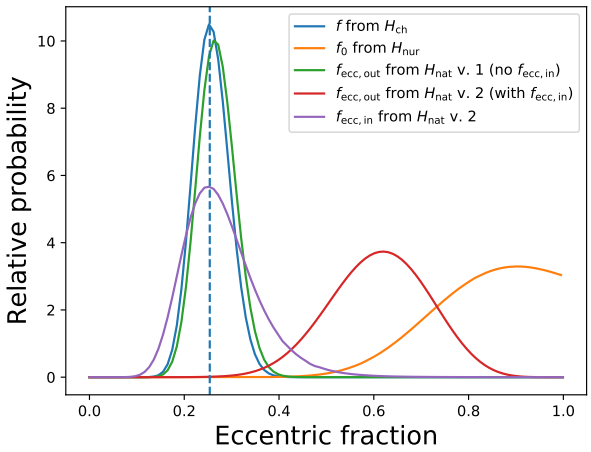

Figure 2.16. Probability histogram of the eccentric fraction, which under the Chance hypothesis is the eccentric fraction (f, blue), under Nurture is the initial eccentric fraction (f_0, orange), under Nature with no $f_{\rm ecc,in}$ is the eccentric fraction beyond $a_{\rm cut}$ ($f_{\rm ecc,out}$, green, labeled with "$H_{\rm nat}$ v. 1"), and under Nature with $f_{\rm ecc,in}$ included is $f_{\rm ecc,out}$ (red, labeled with "$H_{\rm nat}$ v. 2") and the eccentric fraction within $a_{\rm cut}$ ($f_{\rm ecc,in}$, purple, labeled with "$H_{\rm nat}$ v. 2"). The observed fraction of eccentric systems (33/130) is shown with a blue dashed line. The curves have been normalized to have equal area. Note that because the Nurture hypothesis describes eccentric systems circularizing over time, we do not expect f_0 to line up with the observed eccentric fraction.

2.6 Conclusions and Future Work

We develop a Bayesian framework (Section 2.2) for testing the strength of perceived correlations between planetary orbital and system properties. We define hypotheses to describe possible relationships between planetary and system properties: the Nurture hypothesis, where the planetary property $X_{\rm p}$ is driven by age; the Nature hypothesis, where $X_{\rm p}$ is driven by an observed system property other than age; and the Chance hypothesis, where $X_{\rm p}$ is not driven by any observed system parameters. We derive equations to use in calculating the odds ratios of pairs of these hypotheses.

The odds ratio itself is calculated using Eqn. 2.1. The use of that equation requires knowledge of the likelihood $p(X_{\rm p}, t_\star, \mathbf{X}_{\rm ob})$ for each individual system under each hypothesis. This likelihood is given by Eqns. 2.6, 2.9, and 2.10 for the Nurture, Nature, and Chance hypotheses, respectively. The equations for a binary parameter (i.e., when $X_{\rm p}$ can take on 0 or 1) – used in the applications here – are Eqns. 2.7, 2.9, and 2.11. If the binary parameter can only go from $X_{\rm p0} = 1$ to $X_{\rm p} = 0$ and not from $X_{\rm p0} = 0$ to $X_{\rm p} = 1$, the likelihood for the Nurture hypothesis can also be found with Eqn. 2.8.

In the future, we can incorporate uncertainties in stellar ages into the assessment of the odds ratio, by adding a term to the likelihood that accounts for the probability of measuring $t_\star$ given the measurement uncertainties ($p(t_{\star,\rm obs}|t_\star)$) and marginalizing over $t_\star$ in the joint $X_{\rm p}, t_\star$ posterior.

We apply our equations to the question of 2:1 resonance disruption (Section 2.3) and find a roughly equal amount of support for the Nurture hypothesis as for the Chance hypothesis. One is not clearly favored over the other, so by our approach, it is uncertain whether the supposed trend is coincidental or not. Going forward, though we are not aware of any such relation proposed in the literature, we will also investigate possible relations between 2:1 resonances and system properties other than age with the Nature hypothesis. Additionally, we will be able to apply our framework to a larger dataset thanks to observations from the likes of *TESS* and *Gaia* that will not only reveal more exoplanets (and thus more systems with 2:1 resonances), but also more precise stellar ages. *TESS* is expected to uncover many nearby planetary systems that will be relatively easy to follow up and characterize, which will make it easier to identify systems with 2:1 resonances. It will also yield ages via gyrochronology. The precise distances from *Gaia* will enable calibration of other stellar parameters and thus yield ages in that way. A larger sample of 2:1 resonant systems with known ages may allow us to confidently favor one hypothesis in our framework over another. This will help us understand planetary

formation environments as well as the mechanisms that disrupt orbital resonances.

We also investigate the source of the observed stellar obliquity trend (Section 2.4) and find that a correlation of alignment state with temperature is strongly favored over a correlation with age or a chance relation. Thus our results favor the interpretation of Winn et al. (2010) that hot stars tend to be misaligned with their planet's orbits and cool stars are aligned, rather than the interpretation that stars are gradually realigned as they age and cool down or that there is no relation between alignment state and other system properties. This indicates that whatever process realigns stellar spin and planetary orbits occurs predominantly in cooler stars (possibly due to the size of the convective zone) and happens on timescales much shorter than the lifetime of the stars (Winn et al., 2010). The processes that produce misalignments and govern their subsequent evolution are not well understood (see Albrecht et al. 2022 for a review), and the correlation seen here could also be an indication that different misaligning mechanisms operate at different stellar temperatures or, probably more directly, stellar masses.

Finally, we apply our framework to the set of known hot Jupiters with measured eccentricities and stellar ages to determine if it truly exhibits an evolutionary trend or is better described by a relation between eccentricity and semimajor axis (Section 2.5). We find very strong support for the Nurture hypothesis compared to the Nature and Chance hypotheses. Thus our results agree with those of Quinn et al. (2014) that the data show hot Jupiter orbits circularizing over time. This supports the high-eccentricity migration mechanism for hot Jupiter formation.

There are other planet-star correlations suggested in the literature to which we can apply this framework. Ballard & Johnson (2016) looked at the *Kepler* dichotomy around M-dwarfs. They suggested that the observed excess of singly-transiting planets may be a result either of different formation processes producing some planetary systems with high mutual inclinations, or of the dynamical scattering of planetary inclinations over longer timescales. Pu & Wu (2015) also suggested that many planetary systems may start out tightly packed and then experience dynamical instability that leads to the loss of some of the planets, producing the high number of singly- and doubly-transiting systems. Veras et al. (2015) have shown that the high-precision stellar ages expected from the *PLATO* mission will enable the detection of a trend of exoplanet frequency with age. We will investigate this case in our future work and look forward to the increased insight afforded by the high-quality data from upcoming missions.

Acknowledgements

We thank the referee for the helpful comments on this paper. We gratefully acknowledge support from the Alfred P. Sloan Foundation's Sloan Research Fellowship and NASA XRP 80NSSC18K0355. We thank Tom Loredo, Darin Ragozzine, and Leslie Rogers for helpful conversations. The Center for Exoplanets and Habitable Worlds is supported by the Pennsylvania State University, the Eberly College of Science, and the Pennsylvania Space Grant Consortium. This research was supported in part by the National Science Foundation under Grant No. NSF PHY-1748958.

Appendix A: Derivation of Equation 2.8 from Equation 2.7

To obtain Eqn. 2.8 from Eqn. 2.7, for when $X_{\rm p}$ can go from 1 to 0 but not from 0 to 1, we separate out Eqn. 2.7 for each combination of $X_{\rm p}$ and $X_{\rm p0}$ and adjust the limits of integration over $t_{\rm e}$ accordingly:

$$\begin{aligned} p(X_{\rm p}, t_\star, \mathbf{X}_{\rm ob}|f_0, \mathbf{Y}) &= \iint p(X_{\rm p}=0|t_\star, t_{\rm e}, X_{\rm p0}=0, \mathbf{Y}) \\ &\times p(t_{\rm e}|X_{\rm p0}, \mathbf{X}_{\rm ob}, \mathbf{X}_{\rm nob}, \mathbf{Y}) p(t_\star, \mathbf{X}_{\rm ob}, \mathbf{X}_{\rm nob}|\mathbf{Y}) \\ &\times p(X_{\rm p0}=0|f_0) dt_{\rm e} d\mathbf{X}_{\rm nob} \\ &= \iint (1) \times \delta(t_{\rm e}-\infty) p(t_\star, \mathbf{X}_{\rm ob}, \mathbf{X}_{\rm nob}|\mathbf{Y}) \\ &\times (1-f_0) dt_{\rm e} d\mathbf{X}_{\rm nob} \\ &= (1-f_0) \int p(t_\star, \mathbf{X}_{\rm ob}, \mathbf{X}_{\rm nob}|\mathbf{Y}) d\mathbf{X}_{\rm nob} \\ &, X_{\rm p}=0, X_{\rm p0}=0 \end{aligned} \tag{2.47}$$

$$\begin{aligned} p(X_{\rm p}, t_\star, \mathbf{X}_{\rm ob}|f_0, \mathbf{Y}) &= \iint p(X_{\rm p}=0|t_\star, t_{\rm e}, X_{\rm p0}=1, \mathbf{Y}) \\ &\times p(t_{\rm e}|X_{\rm p0}, \mathbf{X}_{\rm ob}, \mathbf{X}_{\rm nob}, \mathbf{Y}) p(t_\star, \mathbf{X}_{\rm ob}, \mathbf{X}_{\rm nob}|\mathbf{Y}) \\ &\times p(X_{\rm p0}=1|f_0) dt_{\rm e} d\mathbf{X}_{\rm nob} \\ &= \iint_0^{t_\star} (1) \times p(t_{\rm e}|X_{\rm p0}, \mathbf{X}_{\rm ob}, \mathbf{X}_{\rm nob}, \mathbf{Y}) \\ &\times p(t_\star, \mathbf{X}_{\rm ob}, \mathbf{X}_{\rm nob}|\mathbf{Y}) (f_0) dt_{\rm e} d\mathbf{X}_{\rm nob} \end{aligned}$$

$$
\begin{aligned}
&+ \iint_{t_\star}^{\infty} (0) \times p(t_\mathrm{e}|X_\mathrm{p0}, \mathbf{X}_\mathrm{ob}, \mathbf{X}_\mathrm{nob}, \mathbf{Y}) \\
&\times p(t_\star, \mathbf{X}_\mathrm{ob}, \mathbf{X}_\mathrm{nob}|\mathbf{Y})(f_0) dt_\mathrm{e} d\mathbf{X}_\mathrm{nob} \\
&= f_0 \iint_{0}^{t_\star} p(t_\mathrm{e}|X_\mathrm{p0}, \mathbf{X}_\mathrm{ob}, \mathbf{X}_\mathrm{nob}, \mathbf{Y}) dt_\mathrm{e} \\
&\times p(t_\star, \mathbf{X}_\mathrm{ob}, \mathbf{X}_\mathrm{nob}|\mathbf{Y}) d\mathbf{X}_\mathrm{nob} \\
&, X_\mathrm{p} = 0, X_\mathrm{p0} = 1
\end{aligned} \tag{2.48}
$$

$$
p(X_\mathrm{p}, t_\star, \mathbf{X}_\mathrm{ob}|f_0, \mathbf{Y}) = 0 \qquad\qquad , X_\mathrm{p} = 1, X_\mathrm{p0} = 0 \tag{2.49}
$$

$$
\begin{aligned}
p(X_\mathrm{p}, t_\star, \mathbf{X}_\mathrm{ob}|f_0, \mathbf{Y}) &= \iint p(X_\mathrm{p} = 1|t_\star, t_\mathrm{e}, X_\mathrm{p0} = 1, \mathbf{Y}) \\
&\times p(t_\mathrm{e}|X_\mathrm{p0}, \mathbf{X}_\mathrm{ob}, \mathbf{X}_\mathrm{nob}, \mathbf{Y}) p(t_\star, \mathbf{X}_\mathrm{ob}, \mathbf{X}_\mathrm{nob}|\mathbf{Y}) \\
&\times p(X_\mathrm{p0} = 1|f_0) dt_\mathrm{e} d\mathbf{X}_\mathrm{nob} \\
&= \iint_{0}^{t_\star} (0) \times p(t_\mathrm{e}|X_\mathrm{p0}, \mathbf{X}_\mathrm{ob}, \mathbf{X}_\mathrm{nob}, \mathbf{Y}) \\
&\times p(t_\star, \mathbf{X}_\mathrm{ob}, \mathbf{X}_\mathrm{nob}|\mathbf{Y})(f_0) dt_\mathrm{e} d\mathbf{X}_\mathrm{nob} \\
&+ \iint_{t_\star}^{\infty} (1) \times p(t_\mathrm{e}|X_\mathrm{p0}, \mathbf{X}_\mathrm{ob}, \mathbf{X}_\mathrm{nob}, \mathbf{Y}) \\
&\times p(t_\star, \mathbf{X}_\mathrm{ob}, \mathbf{X}_\mathrm{nob}|\mathbf{Y})(f_0) dt_\mathrm{e} d\mathbf{X}_\mathrm{nob} \\
&= f_0 \iint_{t_\star}^{\infty} p(t_\mathrm{e}|X_\mathrm{p0}, \mathbf{X}_\mathrm{ob}, \mathbf{X}_\mathrm{nob}, \mathbf{Y}) dt_\mathrm{e} \\
&\times p(t_\star, \mathbf{X}_\mathrm{ob}, \mathbf{X}_\mathrm{nob}|\mathbf{Y}) d\mathbf{X}_\mathrm{nob} \\
&, X_\mathrm{p} = 1, X_\mathrm{p0} = 1.
\end{aligned} \tag{2.50}
$$

Combining Eqns. 2.47 and 2.48 and Eqns. 2.49 and 2.50 gives the desired result:

$$
\begin{aligned}
p(X_\mathrm{p}, t_\star, \mathbf{X}_\mathrm{ob}|f_0, \mathbf{Y}) &= \int \left[1 - f_0 + f_0 \int_{0}^{t_\star} p(t_\mathrm{e}|X_\mathrm{p0}, \mathbf{X}_\mathrm{ob}, \mathbf{X}_\mathrm{nob}, \mathbf{Y}) dt_\mathrm{e}\right] \\
&\times p(t_\star, \mathbf{X}_\mathrm{ob}, \mathbf{X}_\mathrm{nob}|\mathbf{Y}) d\mathbf{X}_\mathrm{nob} \qquad\qquad , X_\mathrm{p} = 0 \\
p(X_\mathrm{p}, t_\star, \mathbf{X}_\mathrm{ob}|f_0, \mathbf{Y}) &= f_0 \iint_{t_\star}^{\infty} p(t_\mathrm{e}|X_\mathrm{p0}, \mathbf{X}_\mathrm{ob}, \mathbf{X}_\mathrm{nob}, \mathbf{Y}) dt_\mathrm{e} \\
&\times p(t_\star, \mathbf{X}_\mathrm{ob}, \mathbf{X}_\mathrm{nob}|\mathbf{Y}) d\mathbf{X}_\mathrm{nob} \qquad\qquad , X_\mathrm{p} = 1.
\end{aligned} \tag{2.51}
$$

Again, this is only valid for the situation of a binary X_p that can go from $X_\mathrm{p0} = 1$ to $X_\mathrm{p} = 0$ but cannot go from $X_\mathrm{p0} = 0$ to $X_\mathrm{p} = 1$.

Appendix B: Additional exploration of resonances case

Our investigation into whether 2:1 resonances get disrupted over time yielded an odds ratio for Nurture vs. Chance of 2.2, a result which does not favor one hypothesis over the other. Here we further explore the case of 2:1 resonance disruption by performing several variations on our original odds ratio calculation.

We first examine the effect of high stellar age uncertainties on the results of the resonances case. Koriski & Zucker (2011) retrieved ages for their sample from large chromospheric activity surveys, and the surveys themselves do not report uncertainties for individual stars. However, most of the systems have multiple reported ages. We remove systems which have a difference of $\gtrsim 3$ Gyr between the highest and lowest reported ages, which includes one 2:1 resonant system and four systems without 2:1 resonances. This gives an odds ratio of Nurture to Chance of 2.2, the same as our original result, suggesting that in this application, the stellar age uncertainties do not bias the overall result.

As a further step, we bootstrap the data 300 times – i.e. redraw from the original data a sample of the same size as the original sample, with replacement – and recompute the odds ratio for each iteration. By so doing, we obtain a distribution of odds ratios. This distribution is primarily concentrated between about 1.6 and 3, but has a few high-value outliers as well. We take the $\log_{10}$ of the odds ratios. The median value of the $\log_{10}$ distribution of Nurture vs. Chance ratios is 0.34 and the standard deviation is 0.15. In only 0.67% of cases is the odds ratio greater than 10. Thus there is still not enough evidence to favor either the Nurture or the Chance hypothesis.

Finally, the threshold for a system having a 2:1 resonance used by Koriski & Zucker (2011) – a normalized commensurability proximity value (see Eqn. 2.15) of $\delta < 0.1$ – and which we have adopted here is somewhat arbitrary. As another variation in our calculations, we treat the 2:1 resonance threshold as a hyperparameter. Eqn. 14 in Malhotra (2012) estimates the fractional range of orbital motion over which a resonance angle could librate (without very fast precession of the periapse); for a Jupiter-mass planet, this is about 1%. We marginalize over a range of 1% to 20% of the deviation of the period ratio from commensurability. With this treatment, we obtain a Nurture to Chance odds ratio of 2.0, which is similar to our original value of 2.2.

Appendix C: Additional exploration of obliquities case

The application of our framework to the stellar obliquity case strongly favored the Nature hypothesis, which says that stellar obliquity is driven by stellar temperature, rather than age. Here we present further exploration of this case by performing several variations on our original calculations.

First, we investigate how uncertainties in measured obliquity angle and stellar age impact the results of the obliquities case. Rather than simply removing those systems with highly uncertain obliquity angles, we are interested in those with a level of uncertainty that could easily place them on either side of the 20° threshold. We remove from our sample systems with measured obliquity angle within 1σ of 20°; this results in the exclusion of three aligned systems. We also exclude any systems with an uncertainty in stellar age > 1 Gyr, though the only system for which this is the case is already excluded by the angle criterion. This modified sample results in reduced support for the Nature hypothesis, relative to Nurture and Chance, by about a factor of 2, while the support of Nurture relative to Chance remains essentially unchanged. However, the support for the Nature hypothesis compared to Nurture and Chance remains very strong, and we still conclude that it is the best explanation of the three for the data in question.

Additionally, we bootstrap the data 300 times – i.e. redraw from the original data, with replacement, a sample of the same size as the original sample – and recompute the odds ratios each time to obtain distributions of the odds ratios. We then take the $\log_{10}$ of the ratios. The $\log_{10}$ distribution of Nurture vs. Chance ratios has a median of 0.17 and a standard deviation of 0.16. The $\log_{10}$ distribution of Nature vs. Nurture ratios has a median of 2.2 and standard deviation of 0.91, and the $\log_{10}$ distribution of Nature vs. Chance ratios has a median of 2.4 and standard deviation of 0.90. These values correspond to odds ratios that are slightly reduced from our original calculations, but not enough to change our overall conclusions. In only 4% of cases is the Nature vs. Nurture ratio less than 10, and in only 2% of cases is the Nature vs. Chance ratio less than 10. Thus the Nature hypothesis is still strongly favored.

Finally, the 20° threshold for stellar misalignment is somewhat arbitrary and does not have a strong physical basis. We have used this in our calculations to follow Triaud (2011). An alternative criterion is that of Winn et al. (2010), who consider a system to be misaligned if the measured obliquity angle is $> 10°$ at $> 3\sigma$ level. However, when we apply this alternative criterion to the dataset we use (that of Triaud 2011), we obtain the exact same subsamples of aligned and misaligned stars as with the 20° threshold. Thus,

the criterion we use provides a solid sample division, and we do not marginalize over the threshold in this case.

Appendix D: Additional exploration of eccentricities case

For the question of whether hot Jupiters show evidence of tidal circularization, we found very strong evidence that hot Jupiter eccentricities are driven by age rather than semimajor axis. Here we further explore this case by performing several variations on our original odds ratio calculations.

To examine the effect of highly uncertain data points on the results in the eccentricities case, we remove systems with age uncertainties ≥ 3 Gyr or eccentricity uncertainties ≥ 0.1. This excludes 10 eccentric systems and 19 circular systems. With this reduced sample, the Nurture vs. Nature ratio goes from 1.3×10^8 to 5.0×10^5. The Nurture vs. Chance ratio experiences a similar drop, from 1.5×10^8 to 2.6×10^5. The Nature vs. Chance ratio drops by about a factor of 2. Despite orders of magnitude less relative support for the Nurture hypothesis, it is still clearly the most favorable of the three options.

As an additional test, we bootstrap the data 300 times, i.e. redraw from the original data, with replacement, a sample of the same size as the original sample, to obtain distributions of each of the odds ratios. We then look at the $\log_{10}$ of those distributions. The $\log_{10}$ distribution of Nature vs. Chance ratios has a median value of -0.39 and a standard deviation of 0.65. The $\log_{10}$ Nurture vs. Nature distribution has a median of 9.4 and a standard deviation of 2.5. Finally, the Nurture vs. Chance distribution has a median of 9.3 and a standard deviation of 2.6. Additionally, both the Nurture vs. Nature and Nurture vs. Chance ratios are greater than 100 in every case. Thus a correlation driven by age is still overwhelmingly favored.

Chapter 3
Nature vs. Nurture: Investigating the Effects of Measurement Uncertainties in the Assessment of Potential Trends Between Planetary and Stellar Properties

The text in this chapter is slightly modified from E. D. Safsten and R. I. Dawson, 2022, AJ, 163, 4. I performed the calculations and wrote the manuscript. R. I. Dawson advised on the project and provided significant comments on the manuscript.

Correlations between planetary and stellar properties, particularly age, can provide insight on planetary formation and evolution processes. However, the underlying source of such trends can be unclear, and measurement uncertainties and small sample sizes can leave doubt as to whether an observed trend truly exists. We use a Bayesian framework to examine how uncertainties in measured parameters influence the odds ratios of competing hypotheses for the source of an observed trend. We analyze three reported trends from the literature. In each application, while uncertainties do affect the numerical value of the odds ratios, our conclusions remain the same whether or not uncertainties are taken into account: hot Jupiter eccentricities are circularized over time, obliquities of hot Jupiter hosts are driven by stellar temperature, and there is not enough evidence to favor a trend of 2:1 orbital resonances with age over a chance relation. Updated samples for the 2:1 resonances and obliquities cases do not change the original conclusions. Simulated

2:1 resonance data show that sample size may be more important than measurement precision for drawing a firm conclusion. However, if 2:1 resonances get disrupted on a wide range of timescales, an age trend will be inherently difficult to confirm over a chance relation, even with a large sample. For some applications, full incorporation of measurement uncertainties may be too computationally expensive, making it preferable to use the framework without uncertainties and perform additional tests to examine the effects of highly uncertain measurements.

3.1 Introduction

A good grasp of the properties of stars is essential for understanding the planets they may host, both because stars and planets form contemporaneously from the same original cloud of gas and dust, and because most observations of exoplanets are done indirectly through study of their host stars. Correlations between observed stellar and planetary properties can provide clues about planetary formation and evolution (Christiansen et al., 2019a). In particular, a trend in a planetary property due to stellar age indicates that the planetary property evolves over time, while correlations driven by other stellar parameters (such as effective temperature or mass) may indicate that formation conditions are important for shaping the observed distribution of the planetary property. However, the stellar properties themselves are often interrelated (for example, stars change temperature as they age), which can make it difficult to know the true underlying source of an observed trend. Additionally, proposed trends between planetary and stellar properties may suffer from small sample sizes or large measurement uncertainties, which can leave doubt about whether an apparent trend is real or not.

In Safsten et al. (2020), hereafter Paper 1, we developed a Bayesian framework to assess the strengths of trends of planetary orbital properties with stellar ages. This framework is designed to compare the evidence for two competing hypotheses using an odds ratio, to determine which hypothesis the data better supports. In particular, we defined three hypotheses for the source of an observed trend between a planetary property and a stellar property: that the planetary property is due to the system age and thus evolves over time (Nurture); that the planetary property is due to an observed system parameter other than age (Nature); and that the planetary property is independent of both age and other observed system parameters (Chance). We then used this framework to investigate proposed trends of three planetary properties from the literature: the disruption of 2:1 orbital resonances (Koriski & Zucker, 2011), the obliquities of stars with

hot Jupiters (e.g., Winn et al. 2010; Triaud 2011), and the eccentricities of hot Jupiters (e.g., Quinn et al. 2014). We found that obliquities of hot Jupiter hosts are most likely driven by stellar temperature, and that eccentricities of hot Jupiters are driven by age (i.e., they evolve over time due to tidal circularization). Our result for the 2:1 orbital resonances case was inconclusive.

The Bayesian framework in Paper 1 lacked a formal incorporation of measurement uncertainties. For each case that we examined in Paper 1, we performed additional tests to examine the potential effects of highly uncertain measurements, and in all cases found our overall conclusions to be the same. However, we wish to fully incorporate uncertainties in order to make our framework more general and accurate. In particular, stellar ages typically have large uncertainties (see Soderblom 2010 for a review), though recent observations by the *Gaia* spacecraft (Gaia Collaboration et al., 2016) have enabled better constraints on many stellar parameters, including ages (e.g. Berger et al. 2018, 2020b). In this work, we investigate the effects of measurement uncertainties on the odds ratios we obtain.

Additionally, in both the 2:1 resonances and stellar obliquities cases, we analyzed the original data sets used by Koriski & Zucker (2011) and Triaud (2011) (the studies that originally reported the age trends), respectively, in order to directly compare our results with those of the original papers. More exoplanets have been discovered and characterized since these data sets were compiled, and we wish to apply our framework to updated samples to see how the odds ratios may change, particularly in the 2:1 resonances case, for which our original analysis was inconclusive. In addition to having a greater number of planets, an updated sample can allow us to take advantage of studies that have homogeneously derived ages for planet host stars.

Our aim in this paper is twofold. First, we further generalize the Bayesian framework described in Paper 1 by formally incorporating measurement uncertainties (Section 3.2). We then apply this updated framework to the same datasets used in Paper 1 and compare the results to our original odds ratio calculations. Second, as the original samples for the 2:1 resonances and obliquities cases were compiled a decade ago, we apply our framework to the most recent available data on 2:1 resonances and stellar obliquities. The analysis for the case of 2:1 resonances is in Section 3.3, for the case of stellar obliquities is in Section 3.4, and for the case of hot Jupiter eccentricities is in Section 3.5. We then conclude in Section 3.6.

3.2 General Framework

The Bayesian framework developed in Paper 1 is designed to compare the strengths of competing hypotheses given the available data. The hypotheses represent possible explanations for an apparent correlation between a certain planetary property, denoted $X_{\rm p}$, and other observed system properties. To assess the relative strengths of two hypotheses $H_{\rm A}$ and $H_{\rm B}$, we need to compute an odds ratio (Eqn. 1 in Paper 1):

$$\frac{p(H_{\rm A}|\{X_{\rm p,i}, t_{\star,{\rm i}}, \mathbf{X}_{\rm ob,i}\})}{p(H_{\rm B}|\{X_{\rm p,i}, t_{\star,{\rm i}}, \mathbf{X}_{\rm ob,i}\})} = \frac{\int[\prod_{\rm i} p(X_{\rm p,i}, t_{\star,{\rm i}}, \mathbf{X}_{\rm ob,i}|\mathbf{Y}, H_{\rm A})]p(\mathbf{Y})d\mathbf{Y}}{\int[\prod_{\rm i} p(X_{\rm p,i}, t_{\star,{\rm i}}, \mathbf{X}_{\rm ob,i}|\mathbf{Y}, H_{\rm B})]p(\mathbf{Y})d\mathbf{Y}} \frac{p(H_{\rm A})}{p(H_{\rm B})}, \tag{3.1}$$

the ratio of the probabilities of each hypothesis given the available data, where $t_\star$ is the stellar age and $\mathbf{X}_{\rm ob}$ is observed system parameters other than age and $X_{\rm p}$. This requires us to compute, for each individual system and under each hypothesis, the likelihood $p(X_{\rm p}, t_\star, \mathbf{X}_{\rm ob}|\mathbf{Y})$ that the system exists with a certain set of $X_{\rm p}$, age, and other system parameters, given the hyperparameters (population-wide variables) $\mathbf{Y}$. It also requires us to specify our a priori beliefs on the relative strengths of $H_{\rm A}$ and $H_{\rm B}$, represented by $p(H_{\rm A})/p(H_{\rm B})$. Hereafter, we give equal weight to each hypothesis, so this term cancels out. Note that we also drop the i subscript, with the understanding that variables other than hyperparameters refer to individual system parameters.

In Paper 1, we defined three hypotheses for the source of the observed distribution of $X_{\rm p}$. First, the Nurture hypothesis says that the planetary property $X_{\rm p}$ is driven by the age of the system, i.e. it evolves over time. Second, the Nature hypothesis says that $X_{\rm p}$ is due to a system parameter other than age, such as stellar temperature, and there is no time evolution of $X_{\rm p}$. Finally, the Chance hypothesis says $X_{\rm p}$ is independent of both age and other system parameters. For a more detailed description of the framework, including a more thorough explanation of the Nurture, Nature, and Chance hypotheses, we refer the reader to Section 2 in Paper 1.

We first give the basic equation for the likelihood from which the rest of the framework was derived (Eqn. 2 from Paper 1):

$$p(X_{\rm p}, t_\star, \mathbf{X}_{\rm ob}|\mathbf{Y}) = \int p(X_{\rm p}, t_\star, \mathbf{X}_{\rm ob}, \mathbf{X}_{\rm nob}|\mathbf{Y})d\mathbf{X}_{\rm nob}, \tag{3.2}$$

where $\mathbf{X}_{\rm nob}$ contains other unobserved system parameters that may be relevant for the question at hand. This equation implicitly assumes that all observed parameters are measured at their true values with zero uncertainty. For each of the observed parameters,

we need to include a term in Eqn. 3.2 for the probability of measuring the observed value of the parameter given the true value. We then marginalize over the true parameter values. Let $X_{\rm p,obs}$, $t_{\star,\rm obs}$, and $\mathbf{X}_{\rm ob,obs}$ represent the observed values of the planetary property of interest, the stellar age, and the other observed system properties, respectively, for an individual planetary system, and let $X_{\rm p}$, $t_\star$, and $\mathbf{X}_{\rm ob}$ represent the true values of those quantities, respectively. Then, with uncertainties included, Eqn. 3.2 becomes:

$$p(X_{\rm p,obs}, t_{\star,\rm obs}, \mathbf{X}_{\rm ob,obs}|\mathbf{Y}) = \iiiint p(X_{\rm p,obs}, t_{\star,\rm obs}, \mathbf{X}_{\rm ob,obs}|X_{\rm p}, t_\star, \mathbf{X}_{\rm ob}) \times p(X_{\rm p}, t_\star, \mathbf{X}_{\rm ob}, \mathbf{X}_{\rm nob}|\mathbf{Y}) dX_{\rm p} dt_\star d\mathbf{X}_{\rm ob} d\mathbf{X}_{\rm nob}. \quad (3.3)$$

The $p(X_{\rm p}, t_\star, \mathbf{X}_{\rm ob}, \mathbf{X}_{\rm nob}|\mathbf{Y})$ term can then be modified for each hypothesis as described in Paper 1. This yields the following equations for each hypothesis.

The equations for the Nurture hypothesis introduce two unobserved parameters, $X_{\rm p0}$ and $t_{\rm e}$. $X_{\rm p0}$ is the initial value of $X_{\rm p}$, which is important because $X_{\rm p}$ evolves over time in this hypothesis. The variable $t_{\rm e}$ is the evolutionary timescale, representing the time it takes for a planetary system to go from $X_{\rm p0}$ to $X_{\rm p}$. Then the equation for the Nurture hypothesis, in which $X_{\rm p}$ is driven by the stellar age, $t_\star$, is (modified from Eqn. 6 in Paper 1):

$$\begin{aligned} p(X_{\rm p,obs}, t_{\star,\rm obs}, &\mathbf{X}_{\rm ob,obs}|\mathbf{Y}) \\ &= \iiiint p(X_{\rm p,obs}, t_{\star,\rm obs}, \mathbf{X}_{\rm ob,obs}|X_{\rm p}, t_\star, \mathbf{X}_{\rm ob}) \\ &\times \left[\iint p(X_{\rm p}|t_\star, t_{\rm e}, X_{\rm p0}, \mathbf{Y}) p(t_{\rm e}|\mathbf{X}_{\rm ob}, \mathbf{X}_{\rm nob}, X_{\rm p0}, \mathbf{Y}) \right. \\ &\qquad \left. \times p(t_\star, \mathbf{X}_{\rm ob}, \mathbf{X}_{\rm nob}|\mathbf{Y}) p(X_{\rm p0}|\mathbf{Y}) dt_{\rm e} dX_{\rm p0} \right] dX_{\rm p} dt_\star d\mathbf{X}_{\rm ob} d\mathbf{X}_{\rm nob}. \end{aligned} \quad (3.4)$$

In some applications, $X_{\rm p}$ may take on only two discrete values, which may be represented as $X_{\rm p} = 0$ and $X_{\rm p} = 1$. The Nurture equation for such a binary $X_{\rm p}$ is

(modified from Eqn. 7 in Paper 1):

$$
\begin{aligned}
&p(X_{\rm p,obs}, t_{\star,\rm obs}, \mathbf{X}_{\rm ob,obs}|f_0, \mathbf{Y}) \\
&\qquad = \iiint \sum_{X_{\rm p}=0}^{1} p(X_{\rm p,obs}, t_{\star,\rm obs}, \mathbf{X}_{\rm ob,obs}|X_{\rm p}, t_\star, \mathbf{X}_{\rm ob}) \\
&\qquad \times \Bigg[\int \sum_{X_{\rm p0}=0}^{1} p(X_{\rm p}|t_\star, t_{\rm e}, X_{\rm p0}, \mathbf{Y}) p(t_{\rm e}|\mathbf{X}_{\rm ob}, \mathbf{X}_{\rm nob}, X_{\rm p0}, \mathbf{Y}) \\
&\qquad\qquad \times p(t_\star, \mathbf{X}_{\rm ob}, \mathbf{X}_{\rm nob}|\mathbf{Y}) p(X_{\rm p0}|f_0) dt_{\rm e} \Bigg] dt_\star d\mathbf{X}_{\rm ob} d\mathbf{X}_{\rm nob}.
\end{aligned}
\tag{3.5}
$$

Here, f_0 is a hyperparameter representing the population-wide fraction of systems with a particular value of $X_{\rm p0}$, for example, the fraction of systems that start out with a 2:1 orbital resonance.

The Nurture equation for single-direction evolution of binary $X_{\rm p}$, i.e. where $X_{\rm p}$ can evolve from $X_{\rm p0} = 1$ to $X_{\rm p} = 0$ but not the other way, is (modified from Eqn. 8 in Paper 1):

$$
\begin{aligned}
&p(X_{\rm p,obs}, t_{\star,\rm obs}, \mathbf{X}_{\rm ob,obs}|f_0, \mathbf{Y}) \\
&\qquad = \begin{cases}
\iiint p(X_{\rm p,obs}, t_{\star,\rm obs}, \mathbf{X}_{\rm ob,obs}|X_{\rm p}=0, t_\star, \mathbf{X}_{\rm ob}) & \\
\quad \times \left[1 - f_0 + f_0 \int_0^{t_\star} p(t_{\rm e}|X_{\rm p0}, \mathbf{X}_{\rm ob}, \mathbf{X}_{\rm nob}, \mathbf{Y}) dt_{\rm e}\right] & \\
\quad \times p(t_\star, \mathbf{X}_{\rm ob}, \mathbf{X}_{\rm nob}|\mathbf{Y}) dt_\star d\mathbf{X}_{\rm ob} d\mathbf{X}_{\rm nob} & , X_{\rm p} = 0 \\
\iiint p(X_{\rm p,obs}, t_{\star,\rm obs}, \mathbf{X}_{\rm ob,obs}|X_{\rm p}=1, t_\star, \mathbf{X}_{\rm ob}) & \\
\quad \times \left[f_0 \int_{t_\star}^{\infty} p(t_{\rm e}|X_{\rm p0}, \mathbf{X}_{\rm ob}, \mathbf{X}_{\rm nob}, \mathbf{Y}) dt_{\rm e}\right] & \\
\quad \times p(t_\star, \mathbf{X}_{\rm ob}, \mathbf{X}_{\rm nob}|\mathbf{Y}) dt_\star d\mathbf{X}_{\rm ob} d\mathbf{X}_{\rm nob} & , X_{\rm p} = 1.
\end{cases}
\end{aligned}
\tag{3.6}
$$

In this special case, f_0 specifically represents the fraction of systems with $X_{\rm p0} = 1$.

The equation for the Nature hypothesis, in which $X_{\rm p}$ is driven by a system parameter other than age, contained in $\mathbf{X}_{\rm ob}$, is (modified from Eqn. 9 in Paper 1):

$$
\begin{aligned}
p(X_{\rm p,obs}, t_{\star,\rm obs}, \mathbf{X}_{\rm ob,obs}|\mathbf{Y}) = &\iiiint p(X_{\rm p,obs}, t_{\star,\rm obs}, \mathbf{X}_{\rm ob,obs}|X_{\rm p}, t_\star, \mathbf{X}_{\rm ob}) \\
&\times p(X_{\rm p}|\mathbf{X}_{\rm ob}, \mathbf{Y}) p(t_\star, \mathbf{X}_{\rm ob}, \mathbf{X}_{\rm nob}|\mathbf{Y}) dX_{\rm p} dt_\star d\mathbf{X}_{\rm ob} d\mathbf{X}_{\rm nob}.
\end{aligned}
\tag{3.7}
$$

The equation for the Chance hypothesis, in which $X_{\rm p}$ is not related to either age or other system parameters, and is only determined by random chance, is (modified from

Eqn. 10 in Paper 1):

$$p(X_{\rm p,obs}, t_{\star,\rm obs}, \mathbf{X}_{\rm ob,obs}|\mathbf{Y}) = \iiiint p(X_{\rm p,obs}, t_{\star,\rm obs}, \mathbf{X}_{\rm ob,obs}|X_{\rm p}, t_\star, \mathbf{X}_{\rm ob}) \times p(X_{\rm p}|\mathbf{Y}) p(t_\star, \mathbf{X}_{\rm ob}, \mathbf{X}_{\rm nob}|\mathbf{Y}) dX_{\rm p} dt_\star d\mathbf{X}_{\rm ob} d\mathbf{X}_{\rm nob}. \tag{3.8}$$

The Chance equation for binary $X_{\rm p}$, i.e. where $X_{\rm p}$ can only take on two discrete values, $X_{\rm p} = 0$ or $X_{\rm p} = 1$, is (modified from Eqn. 11 in Paper 1):

$$p(X_{\rm p,obs}, t_{\star,\rm obs}, \mathbf{X}_{\rm ob,obs}|f, \mathbf{Y}) = \begin{cases} \iiint p(X_{\rm p,obs}, t_{\star,\rm obs}, \mathbf{X}_{\rm ob,obs}|X_{\rm p}=0, t_\star, \mathbf{X}_{\rm ob}) & \\ \times (1-f) p(t_\star, \mathbf{X}_{\rm ob}, \mathbf{X}_{\rm nob}|\mathbf{Y}) dt_\star d\mathbf{X}_{\rm ob} d\mathbf{X}_{\rm nob} & , X_{\rm p} = 0 \\ \iiint p(X_{\rm p,obs}, t_{\star,\rm obs}, \mathbf{X}_{\rm ob,obs}|X_{\rm p}=1, t_\star, \mathbf{X}_{\rm ob}) & \\ \times f p(t_\star, \mathbf{X}_{\rm ob}, \mathbf{X}_{\rm nob}|\mathbf{Y}) dt_\star d\mathbf{X}_{\rm ob} d\mathbf{X}_{\rm nob} & , X_{\rm p} = 1. \end{cases} \tag{3.9}$$

In this hypothesis, f is the population-wide fraction of systems with $X_{\rm p} = 1$.

In many instances, the uncertainty distributions associated with the measured quantities are assumed to be Gaussian, with reported error bars representing 1σ. Under this assumption, Eqn. 3.3 becomes

$$p(X_{\rm p,obs}, t_{\star,\rm obs}, \mathbf{X}_{\rm ob,obs}|\mathbf{Y}) = \iiiint \mathrm{N}_{\rm Xp}(X_{\rm p}, \sigma_{\rm Xp}) \mathrm{N}_{\rm t\star}(t_\star, \sigma_{\rm t\star}) \mathrm{N}_{\rm Xob}(\mathbf{X}_{\rm ob}, \sigma_{\rm Xob}) \times p(X_{\rm p}, t_\star, \mathbf{X}_{\rm ob}, \mathbf{X}_{\rm nob}|\mathbf{Y}) dX_{\rm p} dt_\star d\mathbf{X}_{\rm ob} d\mathbf{X}_{\rm nob}, \tag{3.10}$$

where $\sigma_{\rm Xp}$, $\sigma_{\rm t\star}$, and $\sigma_{\rm Xob}$ are the 1σ measurement uncertainties on $X_{\rm p,obs}$, $t_{\star,\rm obs}$, and $\mathbf{X}_{\rm ob,obs}$, respectively.

In Figure 3.1, we display a graphical model showing relationships between parameters and hyperparameters under the three hypotheses without incorporating uncertainties (left) and when uncertainties are incorporated (right). For simplicity, we do not include every possible parameter dependence, but instead tend to focus on those that most often appear in our applications.

As in Paper 1, we interpret the odds ratios using a scale similar to that of Jeffreys (1961) and Kass & Raftery (1995) and consider ratios of $\sim 1 - 10$ to be inconclusive, $\sim 10 - 100$ to be moderately supportive but not decisive, and $\gtrsim 100$ to be strong.

3.3 2:1 Orbital Resonances

Various mechanisms can result in planets locked in orbital resonances. However, it is not known if these configurations are generally stable over long timescales and how common these configurations are shortly after formation. Studies such as Thommes et al. (2008) and Izidoro et al. (2017) have demonstrated resonance disruption through dynamical interactions. Koriski & Zucker (2011) found evidence that systems with 2:1 period commensurabilities were younger than those without. This observed trend suggests that 2:1 resonances may get systematically disrupted over time. If true, this disruption would have important implications for understanding the stability of planetary systems. However, follow-up work by Dong & Dawson (2016) explored the initial resonant fraction and disruption timescale required to account for such a trend. They found that in order to fit the data, all systems would need to start out in resonance. They would also all need to be disrupted on a timescale similar to the age difference between the 2:1 resonant and nonresonant systems. Such fine-tuning of the parameters cast doubt as to whether the observed age trend is real or not.

In Paper 1, we applied our Bayesian framework to the Koriski & Zucker (2011) data, but our analysis did not find sufficient evidence that 2:1 orbital resonances are systematically disrupted over time. Instead, we found an odds ratio of the Nurture hypothesis to the Chance hypothesis of 2.2, which is not strong enough to favor either hypothesis. Here, we revisit the question with our modified framework applied to the original data used by Koriski & Zucker (2011) as well as to several recently obtained samples of planets. We compare evidence for two hypotheses: the Nurture hypothesis, which says that 2:1 resonances are disrupted over time; and the Chance hypothesis, which says that there is no connection between 2:1 resonances and any other system parameters that we consider. As in Paper 1, we do not test the Nature hypothesis because, to our knowledge, there has not been any proposed correlation between 2:1 resonances and system parameters other than age.

We treat this case as having a binary $X_{\rm p}$ – either a system is near a 2:1 resonance, or it is not. We denote this resonance state as R, and we say a system has $R = 1$ if it is near a 2:1 resonance and $R = 0$ if it is not. R represents the true 2:1 resonance state of a system, and $R_{\rm obs}$ represents its observed 2:1 resonance state. The term $p(R_{\rm obs}|R)$ accounts for uncertainties in the measured period ratio and represents the probability of observing a system in a certain resonance state given its true resonance state. In the samples we analyze, all but a few of the systems are either near a 2:1 resonance or not

near a 2:1 resonance at the 3σ level. Accordingly, we will assume $R_{\rm obs} = R$ and drop the $p(R_{\rm obs}|R)$ term in the following equations. In Appendix 3.6, we fully account for uncertainties in period ratio, but find our results to be nearly identical to what we obtain here. We give the stellar age $t_\star$ a uniform prior from 0 to 13.7 Gyr, corresponding to the assumption of a constant star formation rate throughout the age of the universe, and we assume that uncertainties in $t_\star$ are Gaussian. The general equations applied to this case are as follows.

For the Nurture (time-evolution) hypothesis, we assume that R can only evolve in one direction, from $R = 1$ to $R = 0$, i.e. resonances may be broken, but not reformed later on. We also introduce a 2:1 resonance disruption timescale $t_{\rm d}$, which is the time it takes an individual system to go from $R = 1$ to $R = 0$, and which we give a lognormal prior with mean μ and standard deviation σ. We assign $p(\mu) = U(6, 16)$ and $p(\sigma) = U(0, 20)$, both in $\log_{10}$[yr] space. We also include f_0, the fraction of systems that form near a 2:1 resonance, which we give a uniform hyperprior from 0 to 1. Note that f_0, μ, and σ are all hyperparameters. Then the Nurture equation becomes (derived from Eqn. 3.6 and analogous to Eqn. 21 in Paper 1):

$$p(R_{\rm obs}, t_{\star,\rm obs}|\mu, \sigma, f_0) = \begin{cases} \int dt_\star p(t_{\star,\rm obs}|t_\star) & \\ \times \left[(1 - f_0) + f_0 \int_0^{t_\star} dt_{\rm d} p(t_{\rm d}|\mu, \sigma)\right] p(t_\star) & , R_{\rm obs} = 0 \\ \int dt_\star p(t_{\star,\rm obs}|t_\star) f_0 \left[\int_{t_\star}^{\infty} dt_{\rm d} p(t_{\rm d}|\mu, \sigma)\right] p(t_\star) & , R_{\rm obs} = 1. \end{cases} \tag{3.11}$$

In the Chance hypothesis, we have the hyperparameter f, which is the overall fraction of systems near a 2:1 resonance. We give f a uniform hyperprior from 0 to 1. Then the Chance equation becomes (derived from Eqn. 3.9 and analogous to Eqn. 23 in Paper 1):

$$p(R_{\rm obs}, t_{\star,\rm obs}|f) = \begin{cases} \int p(t_{\star,\rm obs}|t_\star) p(t_\star)(1 - f) dt_\star & , R_{\rm obs} = 0 \\ \int p(t_{\star,\rm obs}|t_\star) p(t_\star) f dt_\star & , R_{\rm obs} = 1. \end{cases} \tag{3.12}$$

We consider a pair of planets to be near a 2:1 resonance if they have a normalized commensurability proximity (NCP) score of $\delta < 0.1$, according to Koriski & Zucker (2011). The NCP score is defined by Koriski & Zucker (2011) as

$$\delta = 2\frac{|r - r_{\rm c}|}{r + r_{\rm c}}, \tag{3.13}$$

where r is the measured period ratio and $r_{\rm c}$ is the period commensurability ratio of

interest (2:1, in this case). If a pair of planets in a given system meets this criterion, the entire system is flagged as being near a 2:1 resonance. We note that this threshold for a system being near a 2:1 resonance is somewhat arbitrary. Furthermore, period commensurability alone is not sufficient for a pair of planets to be in resonance – the resonance angle must also librate. However, this condition is much more difficult to ascertain than a simple period commensurability.

3.3.1 Results

For this case, we perform integrations in Python using `scipy.integrate.nquad` with default settings. This integrator uses techniques from the Fortran library QUADPACK; it uses a Clenshaw-Curtis method using Chebyshev moments for finite integration limits, and a Fourier integral if there is an infinite limit.

We apply Eqns. 3.11 and 3.12 first to the original dataset of Koriski & Zucker (2011), in order to compare with our original results. A histogram of the ages in this sample is shown in the upper left panel of Figure 3.2. There are 30 systems total; 5 are near a 2:1 resonance, and 25 are not. The median age is 6.1 Gyr and the standard deviation is 1.8 Gyr. The ages in this dataset were pulled from various surveys of Ca II H&K lines and do not have individual uncertainties reported. However, many of those surveys used a relation derived by Mamajek & Hillenbrand (2008), who estimated an overall uncertainty of 60% on ages derived from their relation when accounting for both calibration and observational uncertainties and astrophysical scatter. Therefore, for each system, we assign $p(t_{\star,\mathrm{obs}}|t_\star)$ a Gaussian distribution with a width of 60% of the reported age. This analysis yields a ratio of the Nurture hypothesis to the Chance hypothesis of 2.2. Within the significant figures we report, this value is the same as what we obtained without formally incorporating uncertainties, and is not strong enough for us to favor one hypothesis over the other.

We consider three additional updated samples. First, we obtained data on systems discovered via radial velocity (RV) with pairs of adjacent massive planets (planetary mass $M_{\mathrm{P}}\sin i > 0.3 M_{\mathrm{J}}$) and measured ages. We acquired the data from NASA's Exoplanet Archive (exoplanetarchive.ipac.caltech.edu; NASA Exoplanet Archive 2021a) on 2021 August 26, using values in the default parameter set, but using the values from alternative sources for systems whose only ages are not in the default parameter set. The total sample contains 40 planetary systems; of these, 7 have a planet pair near a 2:1 resonance, and 33 do not. A histogram of stellar ages of 2:1 resonant and nonresonant systems in this sample is shown in the upper right panel of Figure 3.2. The ages in this sample

range between 0.5 and 10 Gyr, with a median age of 3.0 Gyr and standard deviation of 2.2 Gyr. Most ages have measurement uncertainties of ∼1-2 Gyr. For those systems without reported age uncertainties, we take the median age uncertainty of the rest of the sample, which is 1.6 Gyr for the upper error and 1.5 Gyr for the lower error. As this sample was pulled from the Exoplanet Archive, rather than a single study, the ages have been derived by a variety of methods, most commonly isochrones/evolutionary tracks or chromospheric activity. This sample has a Nurture to Chance odds ratio of 2.0.

As a second updated sample, we use pairs of adjacent giant planets – defined here to mean having planetary radius $R_{\rm P} > 6R_{\oplus}$ – discovered by *Kepler*, with the ages calculated by Berger et al. (2020b) and planetary radii from Berger et al. (2020a). The planetary periods were obtained from the Exoplanet Archive on 2021 November 12 (NASA Exoplanet Archive, 2021b). We use both candidate and confirmed systems (based on the disposition of the Exoplanet Archive) and exclude any that are not in the Berger et al. (2020a,b) catalog. Berger et al. (2020b) combined data from the *Kepler* and *Gaia* spacecraft and used isochrones to derive a homogeneous catalog of stellar ages and other properties. They reported a median stellar age uncertainty of 56%. This sample contains 11 giant-planet pairs. 2 of these are near a 2:1 resonance, and 9 are not. An ages histogram for this sample is shown in the lower left panel of Figure 3.2. Most of the systems in this sparse sample are a couple Gyr old, with two older systems; the median age is 2.5 Gyr, with a standard deviation of 3.2 Gyr. With this sample, we obtain an odds ratio of Nurture to Chance of 1.7.

Finally, we also consider pairs of adjacent small planets ($R_{\rm P} \leq 6R_{\oplus}$) discovered by *Kepler*, again with the Berger et al. (2020b) ages and Berger et al. (2020a) radii, and with the data on periods acquired from the Exoplanet Archive on 2021 November 12. In this sample, there are 598 planetary systems. 158 of these are near a 2:1 resonance, and 440 are not. An ages histogram for this sample is shown in the lower right panel of Figure 3.2. The ages of both resonant and non-resonant systems in this sample range from about 0.5 to about 15 Gyr, with a median age of 4.5 Gyr and standard deviation of 3.1 Gyr. This sample yields an odds ratio of Nurture to Chance of 1.1.

In Figure 3.3, we display histograms of the NCP values for the original Koriski & Zucker (2011) sample and for each of the three updated samples. These plots do not show every system in the samples, but instead are focused near $\delta = 0.1$, the threshold for being near a 2:1 resonance. In the original sample, there is one system close to the resonance threshold, but otherwise the 2:1 resonant and nonresonant systems are well separated. There is one nonresonant RV system near the threshold, but otherwise, for

2:1 ORBITAL RESONANCES

Ratio	Without uncertainties KZ11	With uncertainties KZ11	RV	*Kepler* Giant	*Kepler* Small
$p(H_{\rm nur})/p(H_{\rm ch})$	2.2	2.2	2.0	1.7	1.1

Table 3.1. Odds ratios for the 2:1 resonances cases without (from Paper 1) and with incorporating measurement uncertainties, for the original sample as well as the updated samples.

the RV and *Kepler* giant planet samples, there is a noticeable separation between 2:1 resonant and nonresonant systems. There is less of a separation for the *Kepler* small planets.

Table 3.1 compares the odds ratios obtained without (from Paper 1) and with incorporating uncertainties, for the original sample as well as the updated samples. None of the odds ratios for our updated samples are different enough from our original result to allow us to favor one hypothesis over another. In other words, the relation between 2:1 resonances and age that we have modeled here is just as good as the ages of both 2:1 resonant and nonresonant systems being determined purely by chance. One reason for this comparability is that the ranges we use for our hyperpriors are designed to include a wide range of possibilities for the 2:1 resonance disruption timescale. This means that we potentially include both high-probability and low-probability regions in the $\mu - \sigma$ parameter space. Further testing shows that restricting, for example, μ to (6,7) and σ to (0,1) could produce odds ratios that strongly favor the Chance hypothesis (these ranges were chosen to span relatively low-probability regions of the plots shown in Figure 5 in Paper 1, which show probability contour plots for the hyperparameters f_0, μ, and σ). In such a scenario, the majority of 2:1 resonances get disrupted very early on, so the presence of a 2:1 resonance in a system a few Gyr old goes against the proposed age trend, and thus Chance is favored. However, our lack of knowledge of resonance disruption timescales and the possibility of a wide range of timescales (e.g. Izidoro et al. 2017) prevents us from making any meaningful restrictions on hyperprior ranges. If there is a large variation in the disruption timescale from system to system (i.e. a high value of σ), an age trend may be inherently difficult to distinguish from Chance, even with a large sample such as that of the *Kepler* small planets. We discuss this more in the next section.

3.3.2 Simulated Resonance Data

In this section, we investigate the types of age trends we might be able to detect with available and future age datasets, as well as the effects of measurement uncertainties on the odds ratios. We begin by using the original ages used by Koriski & Zucker (2011) and assume these are the true ages of the stars. There are 30 stars in this sample. We choose a value for μ and a value for σ, to define the underlying population of $t_{\rm d}$ values. For each stellar age, we draw a value for $t_{\rm d}$ from the log-normal distribution set by μ and σ. If the selected value of $t_{\rm d}$ is greater than the age, the system is classified as being near a 2:1 resonance; otherwise, it is classified as non-resonant. This first experiment assumes that $f_0 = 1$, i.e. that all systems begin with a 2:1 resonance. We then simulate measurements of each stellar age by randomly drawing from a normal distribution centered at the true age and with a width of an assumed measurement precision. We do this 100 times for the whole dataset, and calculate two versions of the Nurture to Chance odds ratio for each set of observations, one accounting for measurement uncertainties and one without accounting for measurement uncertainties. We perform these calculations for a range of values of μ and σ at two different levels of measurement uncertainty, 20% and 60% of the stellar age. The latter value is comparable to the median age uncertainties in the Koriski & Zucker (2011) and Berger et al. (2020b) datasets.

We test values of $\mu = 9$, 9.5, and 9.75 – mean disruption timescales comparable to the ages in the sample – and $\sigma = 0.1$, 1, and 5. In all these cases, the odds ratios are of order unity, regardless of the level of measurement uncertainty and regardless of whether the uncertainties are marginalized over or not. Using an initial fraction of $f_0 = 0.5$ or 0.35, instead of 1, makes no significant difference. With the uninformative prior and hyperpriors we have chosen to describe the 2:1 resonance disruption timescale, values of μ comparable to system ages are the most likely to yield strong odds ratios in favor of Nurture; since, with this dataset, they do not, we do not test other values of μ.

Next, we perform this exercise using a somewhat larger artificial sample of 45 stellar ages randomly selected between 0 and 13.7 Gyr, and test μ values of 7, 9, 9.5, 10, and 11, and σ values of 0.01, 0.1, 1, and 5. For most values of μ and σ, we obtain odds ratios of order unity, indicating nearly equal support for the Nurture and Chance hypotheses in the simulated data. For simulated sets with a value of μ significantly higher or lower than the age range in the data, the comparable support for each hypothesis may be due to the limited age range and size of the simulated data. If the typical disruption timescale is, for instance, on the order of 100 Gyr, a dataset with a maximum age of 13.7 Gyr will have most systems still in their initial resonance state. This scenario is essentially equivalent to

Chance, because in both situations, the systems are observed to have the same resonance state with which they formed. Similarly, if the typical disruption timescale is on the order of 10 Myr, a dataset uniformly spread between 0 and 13.7 Gyr will have most initially resonant systems disrupted, and would need many age measurements of very young stars for an age trend to be evident. Thus, an age trend in these scenarios is inherently difficult to distinguish from a Chance relation, given the limitations of a typical age dataset, because they do not show a transition in the number of 2:1 resonant systems with age.

Of the values for μ and σ that we tried, the support for the Nurture hypothesis over Chance was greatest with $\mu = 9.5$ and $\sigma = 0.01$ or 0.1, i.e. a scenario in which 2:1 resonances typically get disrupted after a few billion years, and there is little variation in the disruption timescale from system to system. Histograms of the distribution of Nurture vs. Chance odds ratios for $\mu = 9.5$ and $\sigma = 0.1$ are shown in the top row of Figure 3.4. These plots show the ratios for both levels of measurement uncertainty, and for the calculations performed without incorporating uncertainties (in blue) and with incorporating uncertainties (in green) into the odds ratios. Note that even when uncertainties are not accounted for in the odds ratio, the level of uncertainty does affect the observed ages because we don't perfectly measure the true quantities. This is why the blue histograms differ between the left and right panels. With 20% measurement uncertainties, the odds ratios span roughly three orders of magnitude, but all strongly favor the Nurture hypothesis. Further, there is strong overlap between the blue and green histograms, suggesting that in this case, incorporating uncertainties has little effect on the odds ratios. With 60% measurement uncertainties, the ratios again span several orders of magnitude, but are, on the whole, lower than the ratios from 20% uncertainties. Without incorporating uncertainties, roughly half of the odds ratios are below the threshold of 100 for strongly favoring Nurture. When uncertainties are incorporated, the distribution shifts somewhat to higher ratios, though there is still a good amount of overlap between the blue and green histograms. This suggests that incorporating uncertainties may have a somewhat stronger effect on the 60% age uncertainty odds ratios compared to the 20% age uncertainty odds ratios. The Nurture hypothesis is also strongly favored with $\mu = 10$ and $\sigma = 0.01$ when the ages are measured with 20% uncertainty, and again we see significant overlap between the distributions with and without incorporating uncertainties (though this scenario is not shown in our plots), but with 60% uncertainties, the odds ratios are all inconclusive. For both $\mu = 9.5$ and $\mu = 10$, increasing σ by an order of magnitude yields only odds ratios that do not strongly favor either hypothesis.

We perform this same exercise again using a large simulated dataset, consisting of

200 stellar ages randomly drawn between 0 and 13.7 Gyr. We test $\mu = 7$, 9, 9.5, 10, and 11, and $\sigma = 0.1$, 1, and 5. With a larger sample, a disruption timescale distribution with $\sigma = 5$ still does not yield conclusive odds ratios, and, for values of μ significantly smaller or larger than the typical stellar age, neither does $\sigma = 1$. However, this larger sample strengthens the odds ratios for several other values of μ and σ, particularly for $\mu = 9$ or 9.5. We display a few of the cases where Nurture is strongly favored in the middle and bottom rows of Figure 3.4. The middle row shows $\mu = 9$ and $\sigma = 1$. The Nurture hypothesis is strongly favored for all observations for 20% measurement uncertainty, regardless of whether the uncertainties are marginalized over or not. When uncertainties are incorporated, there are a few very high, outlying odds ratios, but the bulk of the distribution strongly overlaps with the no-uncertainties version. Zooming in on the bulk of the distribution makes this overlap more apparent and shows no significant shift between the uncertainties and no-uncertainties distributions. The bottom left panel shows that Nurture is also overwhelmingly favored with $\mu = 10$, $\sigma = 0.1$, and 20% age uncertainty. The green distribution again overlaps strongly with the blue, though it is shifted to higher values.

In general, the odds ratios calculated with 60% age uncertainties in the larger simulated dataset tend to be lower than those with 20% uncertainties, but usually result in the same overall conclusion. An exception to this is when $\mu = 9$ and $\sigma = 1$, shown in the middle row of Figure 3.4. With 20% uncertainties, Nurture is very strongly favored, but with 60%, the median odds ratio falls below the threshold of 100, whether uncertainties are incorporated or not. With 60% uncertainties, incorporating uncertainties usually doesn't affect the overall conclusion. There is usually significant overlap between the uncertainties and no-uncertainties odds ratio distributions. However, for 60% uncertainties, there is often a noticeable upward shift in the distribution when uncertainties are incorporated. Within the parameters we tested, this shift is most pronounced for $\mu = 10$ and $\sigma = 0.1$, shown in the bottom right of Figure 3.4.

With the large simulated dataset, at least within the parameters we tested, the level of measurement uncertainty, and whether uncertainties are marginalized over or not, does not usually have an effect on the overall conclusions from the odds ratio calculations. For ratios that already strongly favor Nurture, marginalizing over uncertainties may affect the value of the ratio by even several orders of magnitude, but Nurture is usually still strongly favored. On the other hand, the closer the median ratio is to 1, the smaller the effect of measurement uncertainties, and the smaller the spread of ratios from the different simulated observations.

These results indicate that most of the datasets currently available are inadequate for assessing most possible age trends. It is possible that a trend of 2:1 resonances with age may yet exist, but is obscured by measurement uncertainty. More precise stellar age measurements may help settle this question. However, this exercise also suggests that even if 2:1 resonances get disrupted over time, the limited range of a typical stellar age dataset, even with well-measured ages, may preclude us from favoring an age trend over Chance. If the typical 2:1 resonance disruption timescale is much younger or much older than a few Gyr, or if disruption happens on a wide variety of timescales (i.e. if $\sigma \gtrsim 1$) as some studies (e.g. Izidoro et al. 2017) indicate, these situations may be difficult to distinguish from a Chance relation because the available ages do not span enough orders of magnitude. Age measurements of very young multiplanet systems may help this issue if the typical 2:1 resonance disruption timescale is relatively short.

3.4 Obliquities of Stars with Hot Jupiters

Stellar obliquity refers to the tilt of a star's rotation axis relative to the orbital axis of its planet. Obliquities may be excited or dampened by a number of mechanisms, such as planet-planet scattering or tidal interactions; see Section 3.2 of Dawson & Johnson (2018) for a review. Understanding the dominant processes that control stellar obliquities will shed light on the formation and orbital evolution of their associated planets.

Winn et al. (2010) found a correlation between the effective temperatures and obliquities of stars with hot Jupiters: hot stars have high obliquities, and cool stars have low obliquities. They separated "hot" and "cool" stars at a stellar effective temperature of $T_{\rm eff,\star} = 6250$ K, near the Kraft break (Kraft, 1967). They proposed that all stars start out with a wide range of obliquities, and the cooler stars quickly realign with planetary orbits due to their large convective envelopes; hotter stars, without such convective envelopes, remain misaligned. This trend with temperature was also found by Schlaufman (2010) using projected rotational velocity measurements and confirmed by Albrecht et al. (2012) with a much larger sample of obliquities. On the other hand, Triaud (2011) described a trend of stellar obliquity with age, where young stars have a wide range of obliquities but older stars are aligned. They noted that stars more massive than $1.2 M_\odot$ will cool considerably over their main sequence lifetimes. This evolution means, they proposed, that the cool stars with low obliquities could be older stars that slowly tidally realigned as they aged and cooled down. This connection between age and temperature can make it difficult to tell which is the fundamental driving force behind the distribution of stellar

obliquities.

In Paper 1, we used our Bayesian framework to determine whether the sample from Triaud (2011) better supported a model of gradual tidal realignment over time (Nurture hypothesis), or a model of hot stars having high obliquities and cool stars being well aligned (Nature hypothesis). This dataset consisted of 22 stars with mass $M_\star > 1.2 M_\odot$. A star was deemed misaligned if it had a measured projected obliquity angle $\lambda > 20°$; under this criterion, the sample contained 10 misaligned stars and 12 aligned stars (Triaud, 2011). We note that while cool stars do get realigned in the temperature-dependent scenario, the timescale for the realignment would need to be short enough, and occur soon enough after the planet's formation or arrival close to the star, to produce such a sharp trend that we are comfortable classifying this scenario as the Nature hypothesis. We found strong support for the Nature hypothesis, with an odds ratio for Nature vs. Nurture of 210. This conclusion held up under additional tests, including removing stars with highly uncertain ages, and bootstrapping the data. Here, we reanalyze this dataset as well as an updated sample with our modified framework to formally incorporate measurement uncertainties.

For simplicity, and to keep in line with Winn et al. (2010) and Triaud (2011), rather than using the actual value of a system's measured obliquity, we consider whether the obliquity means the system is aligned or misaligned. We represent this property as the binary parameter A, where $A = 1$ if a system is misaligned and $A = 0$ if a system is aligned. $A_{\rm obs}$ represents the observed alignment state of a system, and A represents the true alignment state of a system. The term $p(A_{\rm obs}|A)$ accounts for the uncertainty in the measured projected obliquity, specifically uncertainty as to whether the system is aligned or misaligned. To account for this, we impose the criterion that a system is considered misaligned if it has $\lambda > 10°$ at the 3σ level. This is according to Winn et al. (2010) and is a departure from the $\lambda > 20°$ criterion used by Triaud (2011) and which we used in Paper 1. However, for the Triaud (2011) sample, these two criteria yield the same sets of aligned and misaligned systems. For our updated sample, the new criterion means that the misaligned group will only contain stars with obliquities measured well enough to be confidently considered misaligned. Accordingly, we assume $A_{\rm obs} = A$ and drop the $p(A_{\rm obs}|A)$ term from the following equations. We also note that since the obliquity angle may be easier to precisely measure for stars of different temperatures, the criterion for being considered misaligned may be biased towards certain types of stars, which we do not account for here.

Since a primary concern in this particular application is the evolution of stellar

temperature with age – which makes the true source of the obliquity trend more difficult to distinguish – we need a way to account for this interdependence in the joint distribution $p(t_\star, T_{\rm eff,\star})$. To do this, we use the `isochrones` Python package (Morton, 2015). As input to this program, we use each sample star's $T_{\rm eff,\star,obs}$, $\log(g)_{\rm obs}$, $[{\rm Fe/H}]_{\rm obs}$, and the associated uncertainties for these parameters as listed in the TEPCat catalog (Southworth, 2011), as of 2021 April 29 (in future work, luminosities from *Gaia* may be used). The program output is a joint distribution of stellar age and stellar effective temperature, which we normalize to have an area of 1 and which we will refer to in the following equations as $p(t_{\star,\rm iso}, T_{\rm eff,\star,iso})$. We will then marginalize over $t_{\star,\rm iso}$ and $T_{\rm eff,\star,iso}$. The likelihood equations adapted for each hypothesis in this application are as follows.

In the Nurture (time-evolution) hypothesis, we assume that A can only evolve from 1 to 0, i.e. systems can go from misaligned to aligned, but not the other way around. We introduce the alignment timescale $t_{\rm a}$, the time it takes a system to go from $A = 1$ to $A = 0$. We assume the underlying population of $t_{\rm a}$ has a lognormal distribution with mean μ and standard deviation σ. Both μ and σ are hyperparameters that we give uniform hyperpriors, in $\log_{10}[{\rm yr}]$ space, of $p(\mu) = U(6, 16)$ and $p(\sigma) = U(0, 20)$, respectively. We also include the hyperparameter f_0, the fraction of systems that form misaligned, and give this a uniform hyperprior from 0 to 1. Then the equation for the Nurture hypothesis is (derived from Eqn. 3.6 and analogous to Eqn. 27 in Paper 1):

$$
\begin{aligned}
&p(A_{\rm obs}, T_{\rm eff,\star,obs}, \log(g)_{\rm obs}, [{\rm Fe/H}]_{\rm obs} | \mu, \sigma, f_0) \\
&\quad = \begin{cases}
\iint p(T_{\rm eff,\star,obs}, \log(g)_{\rm obs}, [{\rm Fe/H}]_{\rm obs}) & \\
\times p(T_{\rm eff,\star,iso}, t_{\star,\rm iso} | T_{\rm eff,\star,obs}, \log(g)_{\rm obs}, [{\rm Fe/H}]_{\rm obs}) & \\
\times \left[(1 - f_0) + f_0 \int_0^{t_{\star,\rm iso}} p(t_{\rm a} | \mu, \sigma) dt_{\rm a} \right] dT_{\rm eff,\star,iso} dt_{\star,\rm iso} & , A_{\rm obs} = 0 \\
\iint p(T_{\rm eff,\star,obs}, \log(g)_{\rm obs}, [{\rm Fe/H}]_{\rm obs}) & \\
\times p(T_{\rm eff,\star,iso}, t_{\star,\rm iso} | T_{\rm eff,\star,obs}, \log(g)_{\rm obs}, [{\rm Fe/H}]_{\rm obs}) & \\
\times \left[f_0 \int_{t_{\star,\rm iso}}^{\infty} p(t_{\rm a} | \mu, \sigma) dt_{\rm a} \right] dT_{\rm eff,\star,iso} dt_{\star,\rm iso} & , A_{\rm obs} = 1.
\end{cases}
\end{aligned}
\tag{3.14}
$$

The Nature hypothesis for the alignment case says that stars above $T_{\rm eff,\star} = 6250$K may be misaligned, while stars cooler than this must be aligned. This leads us to use the following for $p(A | T_{\rm eff,\star})$:

$$
p(A | T_{\rm eff,\star} < 6250 \text{ K}, f_{\rm h}) = \begin{cases} 1 & , A_{\rm obs} = 0 \\ 0 & , A_{\rm obs} = 1 \end{cases}
\tag{3.15}
$$

$$p(A|T_{\mathrm{eff},\star} \geq 6250 \text{ K}, f_{\mathrm{h}}) = \begin{cases} 1 - f_{\mathrm{h}} & , A_{\mathrm{obs}} = 0 \\ f_{\mathrm{h}} & , A_{\mathrm{obs}} = 1. \end{cases} \tag{3.16}$$

Here, f_{h} is a hyperparameter representing the overall fraction of hot stars that are misaligned. We assign f_{h} a uniform hyperprior from 0 to 1. Then the equation for the Nature hypothesis is (derived from Eqn. 3.7 and analogous to Eqn. 28 in Paper 1):

$$\begin{aligned} p(A_{\mathrm{obs}}, T_{\mathrm{eff},\star,\mathrm{obs}}, \log(g)_{\mathrm{obs}}, &[\mathrm{Fe/H}]_{\mathrm{obs}} | f_{\mathrm{h}}) \\ &= \iint p(T_{\mathrm{eff},\star,\mathrm{obs}}, \log(g)_{\mathrm{obs}}, [\mathrm{Fe/H}]_{\mathrm{obs}}) \\ &\times p(T_{\mathrm{eff},\star,\mathrm{iso}}, t_{\star,\mathrm{iso}} | T_{\mathrm{eff},\star,\mathrm{obs}}, \log(g)_{\mathrm{obs}}, [\mathrm{Fe/H}]_{\mathrm{obs}}) \\ &\times p(A | T_{\mathrm{eff},\star,\mathrm{iso}}, f_{\mathrm{h}}) dT_{\mathrm{eff},\star,\mathrm{iso}} dt_{\star,\mathrm{iso}}. \end{aligned} \tag{3.17}$$

In the Chance hypothesis, there is no dependence of stellar obliquity on stellar temperature or age. The only thing that determines whether a system is aligned or misaligned is the hyperparameter f, the overall fraction of systems that are misaligned. We give f a uniform hyperpior from 0 to 1. Then the equation for the Chance hypothesis is (derived from Eqn. 3.9 and analogous to Eqn. 31 in Paper 1):

$$\begin{aligned} p(A_{\mathrm{obs}}, &\log(g)_{\mathrm{obs}}, T_{\mathrm{eff},\star,\mathrm{obs}}, [\mathrm{Fe/H}]_{\mathrm{obs}} | f) \\ &= \begin{cases} (1-f) \iint p(T_{\mathrm{eff},\star,\mathrm{obs}}, \log(g)_{\mathrm{obs}}, [\mathrm{Fe/H}]_{\mathrm{obs}}) & \\ \times p(T_{\mathrm{eff},\star,\mathrm{iso}}, t_{\star,\mathrm{iso}} | T_{\mathrm{eff},\star,\mathrm{obs}}, \log(g)_{\mathrm{obs}}, [\mathrm{Fe/H}]_{\mathrm{obs}}) & \\ \times dT_{\mathrm{eff},\star,\mathrm{iso}} dt_{\star,\mathrm{iso}} & , A_{\mathrm{obs}} = 0 \\ f \iint p(T_{\mathrm{eff},\star,\mathrm{obs}}, \log(g)_{\mathrm{obs}}, [\mathrm{Fe/H}]_{\mathrm{obs}}) & \\ \times p(T_{\mathrm{eff},\star,\mathrm{iso}}, t_{\star,\mathrm{iso}} | T_{\mathrm{eff},\star,\mathrm{obs}}, \log(g)_{\mathrm{obs}}, [\mathrm{Fe/H}]_{\mathrm{obs}}) & \\ \times dT_{\mathrm{eff},\star,\mathrm{iso}} dt_{\star,\mathrm{iso}} & , A_{\mathrm{obs}} = 1. \end{cases} \end{aligned} \tag{3.18}$$

We note that the $p(T_{\mathrm{eff},\star,\mathrm{obs}}, \log(g)_{\mathrm{obs}}, [\mathrm{Fe/H}]_{\mathrm{obs}})$ term, which shows up in the equations for each hypothesis, can be pulled out of the integrals and will cancel when odds ratios are calculated, so we do not need to specify it.

3.4.1 Results

To facilitate better comparison with previous analyses, we begin by using the stellar sample of Triaud (2011) with the TEPCat parameters as described above. We

perform integrations in Julia (Bezanson et al., 2017) using the HCubature package (https://github.com/JuliaMath/HCubature.jl), which uses an adaptive GenzMalik algorithm (Genz & Malik, 1980). We use this package because, while `scipy.integrate.nquad` was sufficient for the calculations performed in the 2:1 resonances case, we need a faster algorithm for this case. We obtain the following odds ratios:

$$\frac{p(H_{\rm nat})}{p(H_{\rm nur})} = 1.6 \times 10^3$$
$$\frac{p(H_{\rm nur})}{p(H_{\rm ch})} = 1.4$$
$$\frac{p(H_{\rm nat})}{p(H_{\rm ch})} = 2.2 \times 10^3.$$

These odds ratios mean we find very strong support for the Nature hypothesis (correlation due to temperature) over both Nurture (evolution over time) and Chance. Regarding Nurture vs. Chance, there is nearly equal support for both hypotheses, which is the same result we obtained in Paper 1. The odds ratios for Nature vs. Nurture and Nature vs. Chance are nearly an order of magnitude greater than those which we obtained in our previous analysis. This result further strengthens our conclusion in support of Winn et al. (2010)'s interpretation, that hot stars have high obliquities and cool stars have low obliquities.

In Paper 1, we used the same ages as Triaud (2011) did, whereas here, the ages are found via isochrones. The magnitude of the difference between the original ages and the mean ages from the `isochrones` program is less than 2 Gyr for all stars in the sample, and less than 1 Gyr for all but two stars. Additionally, while we use the stellar temperatures from TEPCat in our original calculations as well as for the input to the `isochrones` program, the mean temperatures output from `isochrones` vary slightly from the input values; the difference is less than 35 K for all stars, and less than 15 K for all but four stars. To check whether these differences have a significant effect on the outcome, we use the mean isochrone ages and mean isochrone temperatures to calculate the odds ratios without uncertainties. We find results very close to those that we got in Paper 1: a Nature vs. Nurture ratio of 170, a Nurture vs. Chance ratio of 1.8, and a Nature vs. Chance ratio of 310. To investigate how much of an effect the covariance of $T_{\rm eff,\star}$ and $t_\star$ has on the results, we marginalize over uncertainties in $T_{\rm eff,\star}$ and $t_\star$, as output by `isochrones`, but treat $T_{\rm eff,\star}$ and $t_\star$ as independent of each other. This yields odds ratios of Nature vs. Nurture of 840, Nurture vs. Chance of 1.8, and Nature vs. Chance of 1.5×10^3. These results show that the increased support for the Nature hypothesis

that we find here is primarily due to accounting for the uncertainties of $T_{\rm eff,\star}$ and $t_\star$, not from discrepancies between the ages used by Triaud (2011) and the isochrone-derived ages, and that the covariance between $T_{\rm eff,\star}$ and $t_\star$ plays a relatively minor role here.

We also test an updated sample of planetary systems with measured obliquities from Albrecht et al. (2022). This dataset consists of 59 stars with mass $M_\star > 1.2 M_\odot$, hosting planets with $a/R_\star < 10$ and planet mass $M_{\rm P} > 0.5 M_{\rm J}$. It contains 25 misaligned stars and 34 aligned stars. We collected each star's $T_{\rm eff,\star,obs}$, $\log(g)_{\rm obs}$, and $[{\rm Fe/H}]_{\rm obs}$ from the TEPCat catalog on 2021 June 16. For two systems – MASCARA-1 and MASCARA-4 – the values for $\log(g)_{\rm obs}$ and $[{\rm Fe/H}]_{\rm obs}$ are listed in the TEPCat catalog without any uncertainties; in these instances, we assign large uncertainties of 0.2 dex for $\log(g)_{\rm obs}$ and 0.1 dex for $[{\rm Fe/H}]_{\rm obs}$. The measured obliquities for this sample are plotted against the TEPCat stellar temperatures and mean ages from the `isochrones` program in Figure 3.5. This dataset yields the following odds ratios:

$$\frac{p(H_{\rm nat})}{p(H_{\rm nur})} = 13$$
$$\frac{p(H_{\rm nur})}{p(H_{\rm ch})} = 4.4$$
$$\frac{p(H_{\rm nat})}{p(H_{\rm ch})} = 55.$$

This updated sample shows a dramatic decrease in support for the Nature (temperature-driven) hypothesis compared to the original sample. It appears that this shift is driven by the WASP-60 system, which has a star with $T_{\rm eff,\star} = 6105 \pm 50$ K strongly misaligned at $\lambda = 129 \pm 17^\circ$ – a strong exception to the rule that cool stars have low obliquities. When we redo the calculations with WASP-60 removed, we obtain odds ratios of:

$$\frac{p(H_{\rm nat})}{p(H_{\rm nur})} = 3.7 \times 10^3$$
$$\frac{p(H_{\rm nur})}{p(H_{\rm ch})} = 5.9$$
$$\frac{p(H_{\rm nat})}{p(H_{\rm ch})} = 2.2 \times 10^4.$$

However, WASP-60 is a borderline case, with a relatively large $a/R_\star$ of 8.5 ± 0.4, planet mass of 0.56 ± 0.04 Jupiter masses near our minimum, and a stellar effective temperature near the hot-cool boundary. Therefore WASP-60 may be a case of a system just out of reach of realignment. When we calculate the odds ratios using a cutoff of $a/R_\star < 7$,

Ratio	Without unc. T11 (no unc.)	With unc. T11	Updated	Updated, no WASP-60
$p(H_{\rm nat})/p(H_{\rm nur})$	210	1.6×10^3	13	3.7×10^3
$p(H_{\rm nur})/p(H_{\rm ch})$	1.4	1.4	4.4	5.9
$p(H_{\rm nat})/p(H_{\rm ch})$	310	2.2×10^3	55	2.2×10^4

Table 3.2. Odds ratios for the stellar obliquity case without (from Paper 1) and with incorporating measurement uncertainties, for the original sample as well as the updated sample.

which excludes WASP-60, we obtain $p(H_{\rm nat})/p(H_{\rm nur}) = 94$, $p(H_{\rm nur})/p(H_{\rm ch}) = 3.3$, and $p(H_{\rm nat})/p(H_{\rm ch}) = 310$, still strongly favoring Nature. Assuming that it is acceptable for WASP-60 to be misaligned under the Nature hypothesis, our results of analyzing updated data indicate very strong support for the Nature hypothesis compared to Nurture or Chance.

Finally, it has been shown that stellar effective temperatures derived from different spectroscopic analysis pipelines can have large discrepancies, of 100 K or more (Furlan et al., 2018). Since the temperatures in the updated sample were not derived homogeneously, this means that our sample of hot stars may be contaminated by stars that are actually cool (and vice versa), potentially skewing the odds ratios. To investigate this possible effect, we select a few of the hot stars near the 6250 K boundary to instead be cool. We give each star with $6250 \leq T_{\rm eff,\star} < 6500$ a 50% chance of having its temperature decreased by 250 K (putting it on the cool side), then recompute the isochrones and odds ratios (excluding WASP-60). This results in 11 hot stars switching to the cool side, including five misaligned stars. The resulting probability for the Nature hypothesis is too small to compute. This is not too surprising; the inclusion of the strong exception of WASP-60 is enough to make the Nature vs. Nurture odds ratio inconclusive, so adding several more strong exceptions would further exacerbate this effect. We do not have any reason to suspect any particular hot star is actually cool, but this just underscores the need for accurate and homogeneously-derived stellar properties for large numbers of stars, for the proper assessment of perceived trends.

We conclude that the obliquities of stars with hot Jupiters are likely driven by stellar temperature rather than age. Table 3.2 summarizes the odds ratios obtained without (from Paper 1) and with incorporating uncertainties, for the original samples as well as the updated sample, with and without WASP-60.

3.5 Eccentricities of Hot Jupiters

Multiple theories have been developed to explain the existence of hot Jupiters, and there is still some debate about which one plays the dominant role. The lead contenders are high-eccentricity migration (e.g. Rasio & Ford 1996) and subsequent tidal circularization, disk migration (Goldreich & Tremaine, 1980; Lin & Papaloizou, 1986), and in situ formation (e.g. Batygin et al. 2016; Boley et al. 2016). Studying the eccentricities of hot Jupiters can offer a clue about which is the dominant mechanism because each will leave a different signature in the eccentricity distribution of hot Jupiters. Disk migration and in situ formation are not expected to excite very large eccentricities (e.g. Petrovich et al. 2014), while high-eccentricity migration, as its name implies, sets planets on initially high-eccentricity orbits that circularize over time (Dawson & Johnson, 2018).

Quinn et al. (2014) found that hot Jupiters that were younger than their tidal circularization timescale $t_{\rm cir}$ tended to have eccentric orbits, while those older than $t_{\rm cir}$ tended to have circular orbits. This is evidence that hot Jupiter orbits circularize over time, supporting high-eccentricity migration as the dominant formation path for this type of planet. However, it was not obvious that separating their sample into groups older and younger than $t_{\rm cir}$ was the only effective way to divide the data into primarily circular and primarily eccentric planets. In Paper 1 we showed that such a division could also effectively be achieved by separating the hot Jupiter sample into groups with small and large semimajor axes, with eccentric planets tending to be farther from their stars. Astrophysically, this separation is plausible because eccentricities at larger semimajor axes are easier to excite and maintain (e.g. Petrovich et al. 2014; Duffell & Chiang 2015). The strong dependence of $t_{\rm cir}$ on semimajor axis also means that a trend of eccentricity with semimajor axis may be seen, particularly in a sample with a small age range, if tidal circularization is at work.

In Paper 1, we compared evidence for the hypothesis that the distribution of hot Jupiter eccentricities is driven by age (Nurture) to the evidence that the eccentricity distribution is shaped by semimajor axis (Nature). We found that the data very strongly supported a correlation due to age over a correlation due to semimajor axis, as well as over a Chance relation in which eccentricity is not at all related to other system properties. Here, we build upon that result by using the modified framework to incorporate measurement uncertainties and examine how the uncertainties affect our results.

Rather than using the measured value of a planet's eccentricity, we only consider whether it means that a planet is on a circular or eccentric orbit. We represent the

eccentricity state with the binary parameter E, where $E = 1$ if the planet is eccentric and $E = 0$ if the planet is circular. We assume that E can only evolve from 1 to 0. $E_{\rm obs}$ represents the observed eccentricity state of a system, and E represents the true eccentricity state of a system. We consider a planet to be eccentric if it has eccentricity $e > 0$ at the 3σ level. We consider this criterion to mean that $E_{\rm obs} = E$, because it means that the eccentric group only contains systems with eccentricities measured well enough to be confidently classified as eccentric. Accordingly, we will drop the $p(E_{\rm obs}|E)$ term from the following equations. Similar to the alignment case, there is a potential bias here due to different levels of RV precision for stars of different temperatures, but we do not account for that here.

In the Nurture (age-dependent) hypothesis, we use the tidal circularization timescale $t_{\rm cir}$, which represents the decay rate of the orbital eccentricity and is given by (Socrates et al., 2012):

$$t_{\rm cir} = \frac{Q_{\rm P} M_{\rm P} a^{6.5}}{6\pi k_{\rm L} G^{0.5} M_\star^{1.5} R_{\rm P}^5}. \tag{3.19}$$

Here, $M_{\rm P}$ is the planetary mass, a is the semimajor axis, $M_\star$ is the stellar mass, and $R_{\rm P}$ is the planetary radius. Following Socrates et al. (2012), we set $k_{\rm L}$, the Love number, to 0.38.

The planetary tidal quality factor $Q_{\rm P}$ is a rough measure of the efficiency of tidal dissipation in a planet. It is difficult to constrain, as it likely depends on a variety of planetary parameters. Yoder & Peale (1981) constrained Jupiter's tidal quality factor to $6 \times 10^4 < Q_{\rm J} < 2 \times 10^6$. For short period giant planets, it is generally assumed to be near 10^6 (e.g. Ogilvie & Lin 2004; Jackson et al. 2008). $Q_{\rm P}$ provides the primary source of uncertainty in the calculation of $t_{\rm cir}$, so in Paper 1 we parameterized the equation for the Nurture hypothesis in terms of $Q_{\rm P}$ instead of $t_{\rm cir}$. We give $Q_{\rm P}$ a lognormal prior with mean μ and standard deviation σ, which are both hyperparameters. We assign μ a uniform hyperprior U(2,8), and σ a uniform hyperprior U(0,5), both in $\log_{10}$ space. These ranges are designed to cover the wide span and variety of possible values of $Q_{\rm P}$ among the hot Jupiter sample. Then with accounting for measurement uncertainties, the equation for the Nurture hypothesis (derived from Eqn. 3.6 and analogous to Eqn. 38 in Paper 1) is:

$$p(E_{\rm obs}, t_{\star,\rm obs}, a_{\rm obs}, R_{\rm P,obs}, M_{\rm P,obs}, M_{\star,\rm obs}|f_0, \mu, \sigma)$$

$$= \begin{cases} \iiiint \int p(t_{\star,\rm obs}|t_\star)p(a_{\rm obs}|a)p(R_{\rm P,obs}|R_{\rm P})p(M_{\rm P,obs}|M_{\rm P}) \\ \times p(M_{\star,\rm obs}|M_\star)p(t_\star, a, R_{\rm P}, M_{\rm P}, M_\star) \\ \times \left[1 - f_0 + f_0 \int_0^{Q_{\rm P,crit}} p(Q_{\rm P}|\mu,\sigma)dQ_{\rm P}\right] dt_\star da dR_{\rm P} dM_{\rm P} dM_\star & , E_{\rm obs} = 0 \\ \iiiint \int p(t_{\star,\rm obs}|t_\star)p(a_{\rm obs}|a)p(R_{\rm P,obs}|R_{\rm P})p(M_{\rm P,obs}|M_{\rm P}) \\ \times p(M_{\star,\rm obs}|M_\star)p(t_\star, a, R_{\rm P}, M_{\rm P}, M_\star) \\ \times f_0 \left[\int_{Q_{\rm P,crit}}^{\infty} p(Q_{\rm P}|\mu,\sigma)dQ_{\rm P}\right] dt_\star da dR_{\rm P} dM_{\rm P} dM_\star & , E_{\rm obs} = 1. \end{cases} \tag{3.20}$$

Here, $Q_{\rm P,crit}$ is the value of $Q_{\rm P}$ for a given planet at which $t_{\rm cir} = t_\star$. We use the hyperparameter f_0 to represent the fraction of planets that start out with eccentric orbits, and give it a uniform hyperprior from 0 to 1. We have also assumed that the uncertainties of measured parameters are independent of each other. For $t_\star$, a, $R_{\rm P}$, $M_{\rm P}$, and $M_\star$, we use uniform priors that encompass the observed values of these parameters in our sample.

The Nature hypothesis for the eccentricities case says that planets close to their stars have circular orbits and those farther out may be eccentric. In Paper 1, we introduced the hyperparameter $a_{\rm cut}$, the semimajor axis cut-off within which planets are all circular. Beyond $a_{\rm cut}$, a planet may be either circular or eccentric. We use the hyperparameter $f_{\rm ecc,out}$ to describe the fraction of eccentric systems outside of $a_{\rm cut}$. This leads to the following for $p(E|a, a_{\rm cut})$:

$$p(E|a < a_{\rm cut}, f_{\rm ecc,out}) = \begin{cases} 1 & , E = 0 \\ 0 & , E = 1 \end{cases} \tag{3.21}$$

$$p(E|a \geq a_{\rm cut}, f_{\rm ecc,out}) = \begin{cases} 1 - f_{\rm ecc,out} & , E = 0 \\ f_{\rm ecc,out} & , E = 1. \end{cases} \tag{3.22}$$

We give $a_{\rm cut}$ a uniform hyperprior from 0 to 0.1 AU, and we give $f_{\rm ecc,out}$ a uniform hyperprior from 0 to 1. With uncertainties, which we again assume to be independent, the equation for the Nature hypothesis (derived from Eqn. 3.7 and analogous to Eqn. 39 in Paper 1) is:

$$\begin{aligned} &p(E_{\rm obs}, t_{\star,\rm obs}, a_{\rm obs}, R_{\rm P,obs}, M_{\rm P,obs}, M_{\star,\rm obs}|a_{\rm cut}, f_{\rm ecc,out}) \\ &\quad = \iiiint \int p(t_{\star,\rm obs}|t_\star)p(a_{\rm obs}|a)p(R_{\rm P,obs}|R_{\rm P})p(M_{\rm P,obs}|M_{\rm P})p(M_{\star,\rm obs}|M_\star) \\ &\quad \times p(E_{\rm obs}|a, a_{\rm cut}, f_{\rm ecc,out})p(t_\star, a, R_{\rm P}, M_{\rm P}, M_\star) dt_\star da dR_{\rm P} dM_{\rm P} dM_\star. \end{aligned} \tag{3.23}$$

In the Chance hypothesis, there is no relation between hot Jupiter eccentricities and any other system properties considered. The proportion of eccentric planets is only governed by the hyperparameter f, the overall fraction of planets that have eccentric orbits. Then with uncertainties, which we assume to be independent, the equation for the Chance hypothesis (derived from Eqn. 3.9 and analogous to Eqn. 43 in Paper 1) is:

$$
\begin{aligned}
&p(E_{\rm obs}, t_{\star,\rm obs}, a_{\rm obs}, R_{\rm P,obs}, M_{\rm P,obs}, M_{\star,\rm obs}|f) \\
&\quad = \begin{cases}
\iiiint \int p(t_{\star,\rm obs}|t_\star)p(a_{\rm obs}|a)p(R_{\rm P,obs}|R_{\rm P})p(M_{\rm P,obs}|M_{\rm P})p(M_{\star,\rm obs}|M_\star) \\
p(t_\star, a, R_{\rm P}, M_{\rm P}, M_\star)(1-f)dt_\star da dR_{\rm P} dM_{\rm P} dM_\star, \\
E_{\rm obs} = 0 \\
\iiiint \int p(t_{\star,\rm obs}|t_\star)p(a_{\rm obs}|a)p(R_{\rm P,obs}|R_{\rm P})p(M_{\rm P,obs}|M_{\rm P})p(M_{\star,\rm obs}|M_\star) \\
p(t_\star, a, R_{\rm P}, M_{\rm P}, M_\star) f dt_\star da dR_{\rm P} dM_{\rm P} dM_\star, \\
E_{\rm obs} = 1.
\end{cases}
\end{aligned} \tag{3.24}
$$

We give f a uniform hyperprior from 0 to 1.

3.5.1 Results

For this case, we analyze the same sample that we used in Paper 1, and we refer the reader to Paper 1 for a link to a machine-readable table of the sample data. This dataset consists of 130 stars hosting hot Jupiters (defined as having planetary mass $0.3 M_{\rm J} < M_{\rm P} < 13 M_{\rm J}$ and orbital period $P < 10$ days) with measured stellar and planetary masses, semimajor axis, age, and eccentricity. We obtained this data, as well as planetary radii for the planets which had them, from the Extrasolar Planets Encyclopaedia (exoplanet.eu; Schneider et al. 2011b) on 2019 May 28. For the 11 systems without reported planetary radii, we estimated the planetary radius using the relation in Eqn. 9 in Weiss et al. (2013). The stellar ages have been derived in a variety of ways, mostly isochrones or evolutionary tracks. Since this data was acquired fairly recently, we do not use an updated sample in this case. Figure 3.6 shows eccentricity versus semimajor axis, eccentricity versus stellar age, and eccentricity versus tidal circularization timescale for our sample.

We consider a planet to be eccentric ($E_{\rm obs} = 1$) if it has $e > 0$ with 3σ confidence, and circular ($E_{\rm obs} = 0$) otherwise. We have excluded planets with reported eccentricity of $e = 0$ with no error bars. If a planet has only an upper limit on the eccentricity, we classify it as circular if $e < 0.1$ and exclude it otherwise.

For this case, we perform integrations in Julia using the HCubature package. As with

the obliquities case, we choose this integrator over `scipy.integrate.nquad` because of HCubature's greater speed. With so many parameters to integrate over for so many systems, the full calculations of Eqns. 3.20-3.24 become prohibitively long. Accordingly, we begin by integrating over just age, as it is typically the most uncertain of the parameter measurements, as well as the tidal quality factor $Q_{\rm P}$ (in the Nurture hypothesis) and the hyperparameters. We treat the other observed parameters – semimajor axis, planetary radius, planetary mass, and stellar mass – as having no measurement uncertainty. We obtain the following odds ratios:

$$\frac{p(H_{\rm nur})}{p(H_{\rm nat})} = 1.8 \times 10^8$$
$$\frac{p(H_{\rm nur})}{p(H_{\rm ch})} = 3.6 \times 10^8$$
$$\frac{p(H_{\rm nat})}{p(H_{\rm ch})} = 2.0.$$

These results are nearly the same as those in Paper 1. We noted in Paper 1 that the strong dependence of $t_{\rm cir}$ on a and $R_{\rm P}$ means that uncertainties in those parameters could have a strong effect on the calculated $t_{\rm cir}$. Integrating over uncertainties in both a and $R_{\rm P}$ along with $t_\star$ ends up requiring too much computation time and memory. Instead, we examined the effects of these parameters individually. Integrating over just uncertainties in a, treating all other observed parameters as having no measurement uncertainty, yields the following odds ratios:

$$\frac{p(H_{\rm nur})}{p(H_{\rm nat})} = 6.9 \times 10^7$$
$$\frac{p(H_{\rm nur})}{p(H_{\rm ch})} = 1.4 \times 10^8$$
$$\frac{p(H_{\rm nat})}{p(H_{\rm ch})} = 2.0.$$

Finally, when integrating over just uncertainties in $R_{\rm P}$, we obtain the following odds ratios:

$$\frac{p(H_{\rm nur})}{p(H_{\rm nat})} = 1.1 \times 10^8$$
$$\frac{p(H_{\rm nur})}{p(H_{\rm ch})} = 2.2 \times 10^8$$

HOT JUPITER ECCENTRICITIES

Ratio	Without uncertainties	With uncertainties		
	No unc.	$t_\star$ unc.	a unc.	$R_{\rm P}$ unc.
$p(H_{\rm nur})/p(H_{\rm nat})$	1.3×10^8	1.8×10^8	6.9×10^7	1.1×10^8
$p(H_{\rm nur})/p(H_{\rm ch})$	1.5×10^8	3.6×10^8	1.4×10^8	2.2×10^8
$p(H_{\rm nat})/p(H_{\rm ch})$	1.1	2.0	2.0	2.0

Table 3.3. Odds ratios for the eccentricities case without (from Paper 1) and with incorporating uncertainties in $t_\star$, a, and $R_{\rm P}$.

$$\frac{p(H_{\rm nat})}{p(H_{\rm ch})} = 2.0.$$

Individually, the uncertainties on $t_\star$, a, and $R_{\rm P}$ do not make a substantial difference in the odds ratios, and so it does not seem likely that they would have a very profound influence when accounted for together. The most significant difference comes from including a uncertainties, which decreases support for the Nurture hypothesis by a factor of $\sim$2. Table 3.3 summarizes the odds ratios obtained without (from Paper 1) and with incorporating uncertainties in $t_\star$, a, and $R_{\rm P}$.

Even when incorporating what we expect to be the most influential uncertainties, the evidence very strongly favors a trend of eccentricity driven by age, rather than by semimajor axis or random chance. This result supports tidal circularization as a hot Jupiter formation mechanism. We note that since we allow for an underlying circular population of hot Jupiters (represented by $1 - f_0$), this does not mean that tidal circularization is the only formation mechanism for hot Jupiters, but does support that at least some hot Jupiters undergo this process.

In Figure 3.7 we display a posterior probability histogram of f_0, which has been marginalized over all other parameters and hyperparameters and normalized such that the highest probability is 1. We draw 10^4 random points from this distribution. This sample has a median of 0.824, with a 68% confidence interval of 0.692 to 0.935. We thus conclude that under the Nurture hypothesis, at least half of the planets in our sample have undergone or are currently experiencing tidal circularization.

3.6 Conclusion

We improve upon the Bayesian framework outlined in Paper 1 by formally incorporating measurement uncertainties (Section 3.2). We then reanalyze the data we used in Paper 1 with the updated framework and find that marginalizing over measurement uncertainties

does not change our original conclusions. We also analyze updated samples for both the 2:1 resonances and the obliquities cases, and find our previous conclusions still hold. These results lead us to conclude that hot Jupiters are circularized over time, supporting high-eccentricity migration and tidal circularization (Section 3.5), and that the stellar obliquities of stars with hot Jupiters are driven by stellar effective temperature (Section 3.4). It remains unclear whether 2:1 orbital resonances are disrupted over time (Section 3.3). Through the analysis of simulated data, we show that significant uncertainties, comparable to the uncertainties in the real data, in the measured stellar ages can, in some cases, obscure a true trend of 2:1 resonances with age. However, an increased sample size will likely have a more significant effect on the odds ratio than just more precise ages. Even with a large sample size, though, it will be difficult to confirm a trend of 2:1 resonances with age if the resonances get disrupted on a wide range of timescales.

While it is relatively simple to include uncertainties in the general equations as well as equations for specific applications, performing the complete calculations may, in some cases, present a prohibitive computational challenge. Each observed parameter included in the equations means another integral to perform, and the computational time and memory required to do them all can pile up to impracticable levels. Additionally, in Paper 1 we showed that in certain cases, some terms in the equations canceled out when the odds ratios were taken, eliminating the need to calculate those terms. When uncertainties are fully incorporated, such cancellation may not be possible. For example, in the obliquities case (Section 3.4), we integrate over a joint posterior of stellar age and stellar effective temperature, $p(T_{\mathrm{eff},\star,\mathrm{iso}}, t_{\star,\mathrm{iso}} | T_{\mathrm{eff},\star,\mathrm{obs}}, \log(g)_{\mathrm{obs}}, [\mathrm{Fe/H}]_{\mathrm{obs}})$. For an individual star, this term is, of course, the same under each hypothesis. However, since age and temperature appear elsewhere in the equations, the integral over the joint posterior cannot be separated out and canceled when ratios are taken (specifically, stellar age appears in the integration limits over the alignment timescale t_{a} in the Nurture hypothesis, and the stellar effective temperature appears in the $p(A|T_{\mathrm{eff},\star,\mathrm{iso}})$ term, which describes how the alignment state A depends on effective temperature, in the Nature hypothesis). Without incorporating uncertainties, there is still a $p(T_{\mathrm{eff},\star}, t_{\star})$ term, but no integral over $T_{\mathrm{eff},\star}$ or $t_{\star}$, so $p(T_{\mathrm{eff},\star}, t_{\star})$ would cancel in the odds ratios. For applications of this framework with many variables to account for and/or a large sample size, the use of the simpler framework in Paper 1 may be preferable, accompanied by additional tests (bootstrapping, removing outliers, etc.) to explore the effect of highly uncertain measurements on the results. Alternatively, one could choose to only account for uncertainties on parameters with large measurement errors, as we do for the eccentricities case here (see Section 3.5).

Acknowledgements

We thank the referee for the helpful comments on this paper. We gratefully acknowledge support from NASA XRP 80NSSC18K0355. This material is based upon work supported by the National Aeronautics and Space Administration under Grant No. 80NSSC20M0097 issued through the PA Space Grant Consortium. The Center for Exoplanets and Habitable Worlds is supported by the Pennsylvania State University, the Eberly College of Science, and the Pennsylvania Space Grant Consortium. Computations for this research were performed on the Pennsylvania State University's Institute for Computational and Data Sciences' Roar supercomputer. This content is solely the responsibility of the authors and does not necessarily represent the views of the Institute for Computational and Data Sciences. This research has made use of the NASA Exoplanet Archive, which is operated by the California Institute of Technology, under contract with the National Aeronautics and Space Administration under the Exoplanet Exploration Program. This research has made use of data obtained from or tools provided by the portal exoplanet.eu of The Extrasolar Planets Encyclopaedia. We acknowledge the use of the software packages NumPy (Harris et al., 2020) in performing calculations and generating random numbers; Pandas (McKinney, 2010, 2011) in reading in data files; Matplotlib (Hunter, 2007) in generating plots; and Cython (Behnel et al., 2011) and PyJulia (Arakaki et al., 2020) in creating code that runs faster than pure Python.

This research made use of the following software: SciPy (Virtanen et al., 2020), NumPy (Harris et al., 2020), Matplotlib (Hunter, 2007), Cython (Behnel et al., 2011), Pandas (McKinney, 2010, 2011), PyJulia (Arakaki et al., 2020), Julia (Bezanson et al., 2017), isochrones (Morton, 2015).

Appendix A: Accounting for Uncertainty in Period Ratio in 2:1 Resonances case

When studying the case of 2:1 orbital resonances in Section 3.3, we consider the 2:1 resonant state of a system R, rather than directly using the period ratio or normalized commensurability proximity (NCP; Eqn. 3.13) parameters themselves. The resulting $p(R_{\rm obs}|R)$ term in the equations represents the probability of seeing the observed resonance state given the true resonance state of a system. Since the majority of the systems in our samples are more than 3σ away from the 2:1 resonance threshold of $\boldsymbol{\delta} = 0.1$ – i.e.

are confidently either near a 2:1 resonance or not – based on period ratio uncertainties, we assumed $R_{\rm obs} = R$ and dropped the $p(R_{\rm obs}|R)$ term from the equations. Here, we fully incorporate uncertainties in period ratio to address the few systems in our samples whose period ratio errors put them within 3σ of the 2:1 resonance threshold. In the RV sample, two systems are within 3σ, two systems are within 2σ, and one system is within 1σ. In both of the *Kepler* samples, no systems are within 3σ.

It is not straightforward to translate uncertainty in period ratio to a formulation for $p(R_{\rm obs}|R)$. Instead, we rewrite the equations in terms of the period ratio itself, r, and the observed value of the period ratio, $r_{\rm obs}$. This formulation will allow us to marginalize over r. A certain range of values of r, surrounding $r = 2$, yield NCP values of $\delta < 0.1$ and thus are considered to be near a 2:1 resonance. We represent the lower and upper bounds of the range as $r_{\rm l}$ and $r_{\rm h}$, respectively. Within the range of $r_{\rm l}$-$r_{\rm h}$, the rest of the equation takes the form for $R = 1$; otherwise, it takes the form for $R = 0$. Then the likelihood equations become

$$\begin{aligned} p(r_{\rm obs}, t_{\star,\rm obs}|\mu, \sigma, f_0) = &\int_{r_{\rm l}}^{r_{\rm h}} p(r_{\rm obs}|r) p_{\rm Nur,res}(r, t_{\star,\rm obs}|\mu, \sigma, f_0) dr \\ &+ \int_{-\infty}^{r_{\rm l}} p(r_{\rm obs}|r) p_{\rm Nur,nonres}(r, t_{\star,\rm obs}|\mu, \sigma, f_0) dr \\ &+ \int_{r_{\rm h}}^{\infty} p(r_{\rm obs}|r) p_{\rm Nur,nonres}(r, t_{\star,\rm obs}|\mu, \sigma, f_0) dr \end{aligned} \tag{3.25}$$

$$\begin{aligned} p(r_{\rm obs}, t_{\star,\rm obs}|f) = &\int_{r_{\rm l}}^{r_{\rm h}} p(r_{\rm obs}|r) p_{\rm Ch,res}(r, t_{\star,\rm obs}|f) dr \\ &+ \int_{-\infty}^{r_{\rm l}} p(r_{\rm obs}|r) p_{\rm Ch,nonres}(r, t_{\star,\rm obs}|f) dr \\ &+ \int_{r_{\rm h}}^{\infty} p(r_{\rm obs}|r) p_{\rm Ch,nonres}(r, t_{\star,\rm obs}|f) dr, \end{aligned} \tag{3.26}$$

where Eqn. 3.25 is for the Nurture hypothesis and Eqn. 3.26 is for the Chance hypothesis. The probability $p_{\rm Nur,nonres}(r, t_{\star,\rm obs}|\mu, \sigma, f_0)$ includes everything other than $p(R_{\rm obs}|R)$ in the $R = 0$ case of Eqn 3.11, and $p_{\rm Nur,res}(r, t_{\star,\rm obs}|\mu, \sigma, f_0)$ includes everything other than $p(R_{\rm obs}|R)$ in the $R = 1$ case of that same equation. Similarly, $p_{\rm Ch,nonres}(r, t_{\star,\rm obs}|f)$ includes everything other than $p(R_{\rm obs}|R)$ in the $R = 0$ case of Eqn 3.12, and $p_{\rm Ch,res}(r, t_{\star,\rm obs}|f)$ includes everything other than $p(R_{\rm obs}|R)$ in the $R = 1$ case of that same equation. The term $p(r_{\rm obs}|r)$ accounts for the uncertainty in the period ratio (derived from uncertainties in the measured periods), and we assume $r_{\rm obs}$ is drawn from a Gaussian distribution with mean r and standard deviation equal to the period ratio uncertainty.

Calculating the odds ratios in this way results in a Nurture to Chance ratio of 2.1 for the RV sample, 1.7 for the *Kepler* giant planet pairs, and 1.1 for the Kepler small planet pairs. There are only a handful of planets within 3σ of the threshold for being near a 2:1 resonance, so it is unsurprising that these results barely differ from what we obtained before.

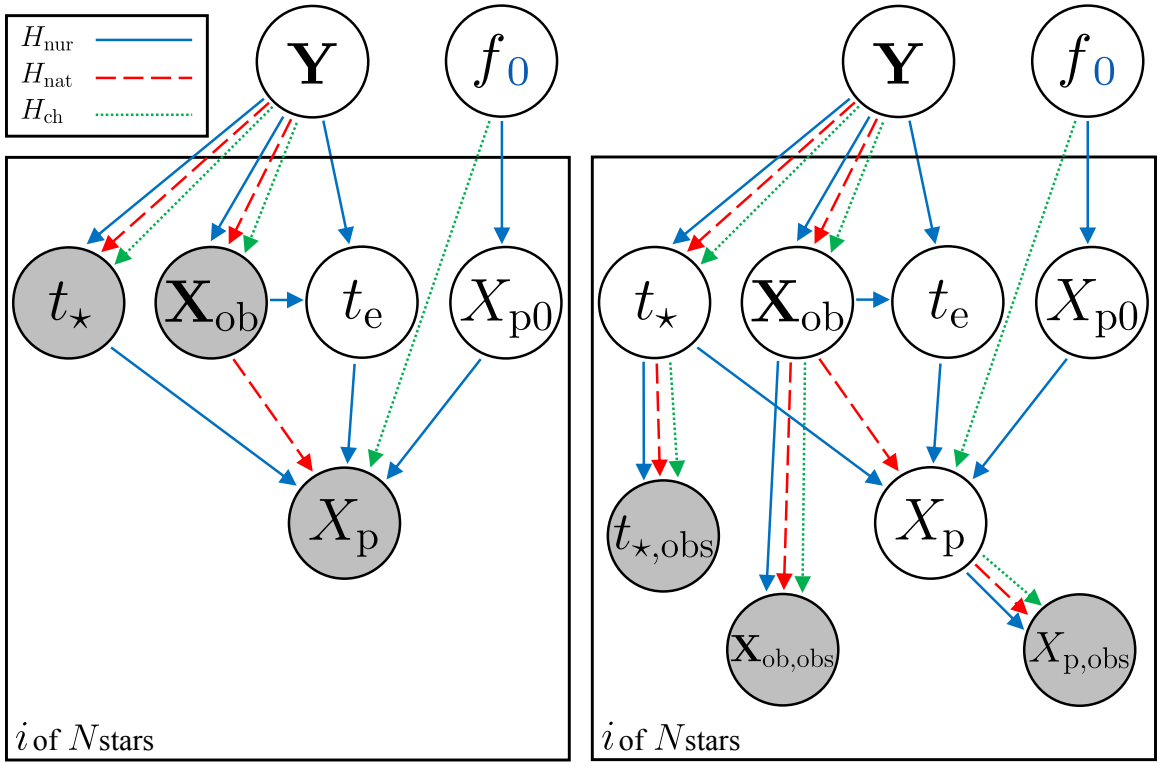

Figure 3.1. Graphical representation of relationships between parameters under the three hypotheses without uncertainties incorporated (left) and with uncertainties incorporated (right). For simplicity, we do not show every possible dependence a model may have, but instead tend to focus on those that come up most often in our applications (specifically, we do not explicitly include relevant non-observed quantities $\mathbf{X}_{\rm nob}$). Parameter relations under the Nurture, Nature, and Chance hypotheses are shown with blue solid, red dashed, and green dotted lines, respectively. The "i of N stars" means that the parameters in the box, or plate, are iterated over each of the N systems in the sample. Gray circles represent observed parameters: the observed planetary property of interest ($X_{\rm p}$ on the left, $X_{\rm p,obs}$ on the right), the observed stellar age ($t_\star$ on the left, $t_{\star,\rm obs}$ on the right), and other observed parameters ($\mathbf{X}_{\rm ob}$ on the left, $\mathbf{X}_{\rm ob,obs}$ on the right). White circles are unobserved individual parameters (on the plate) – the initial value of $X_{\rm p}$ ($X_{\rm p0}$), the evolutionary timescale ($t_{\rm e}$), and, on the right, the true value of the planetary property of interest ($X_{\rm p}$), the true stellar age ($t_\star$), and the true values of other observed parameters ($\mathbf{X}_{\rm ob}$) – and hyperparameters – the fraction of systems with a given value of $X_{\rm p}$ (f), the fraction of systems with a given value of $X_{\rm p0}$ (f_0), and other hyperparameters ($\mathbf{Y}$). The hyperparameters f and f_0 are in the same circle because mathematically, they behave the same way in each hypothesis; they are distinguished by the blue subscript, because f_0 occurs in the Nurture hypothesis while the Chance hypothesis uses f.

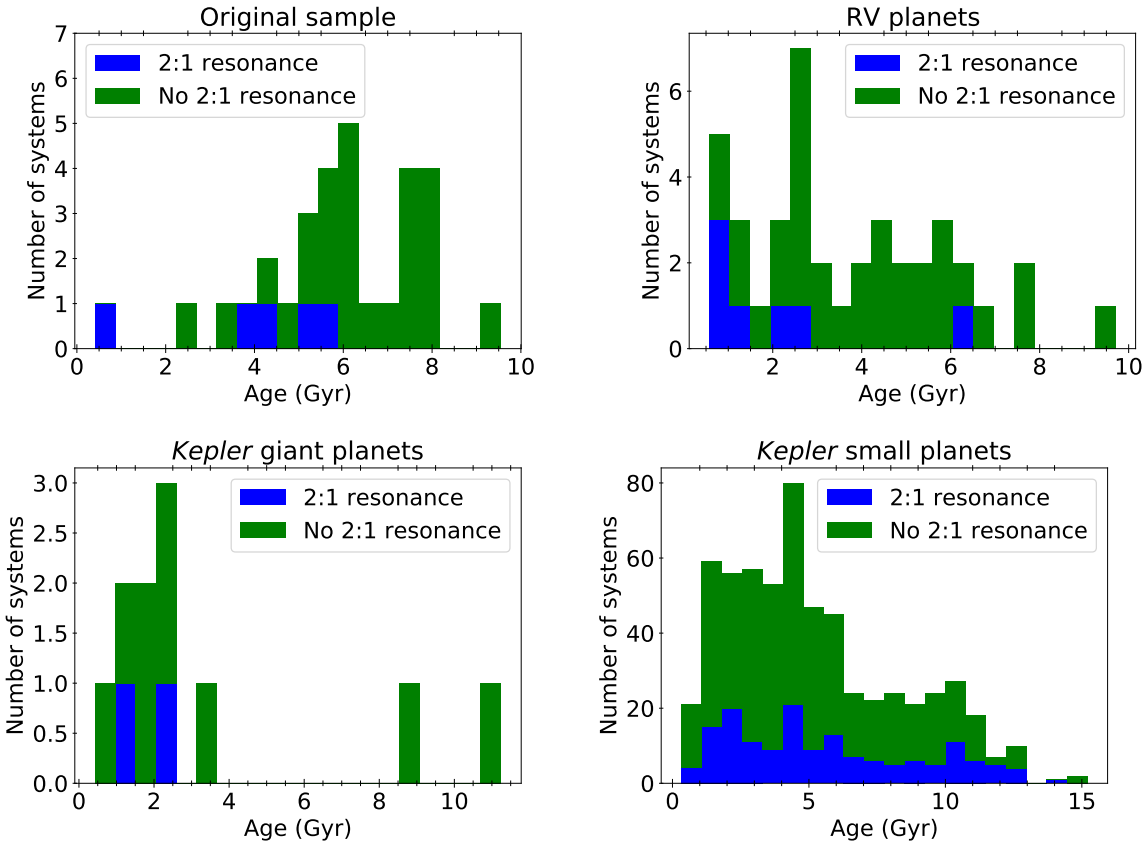

Figure 3.2. Ages histograms for the original Koriski & Zucker (2011) sample (upper left), massive planet pairs in the RV sample (upper right), giant planet pairs in the *Kepler* sample (lower left), and small planet pairs in the *Kepler* sample (lower right). Systems near a 2:1 resonance are shown in blue, and systems without a 2:1 resonance are shown in green.

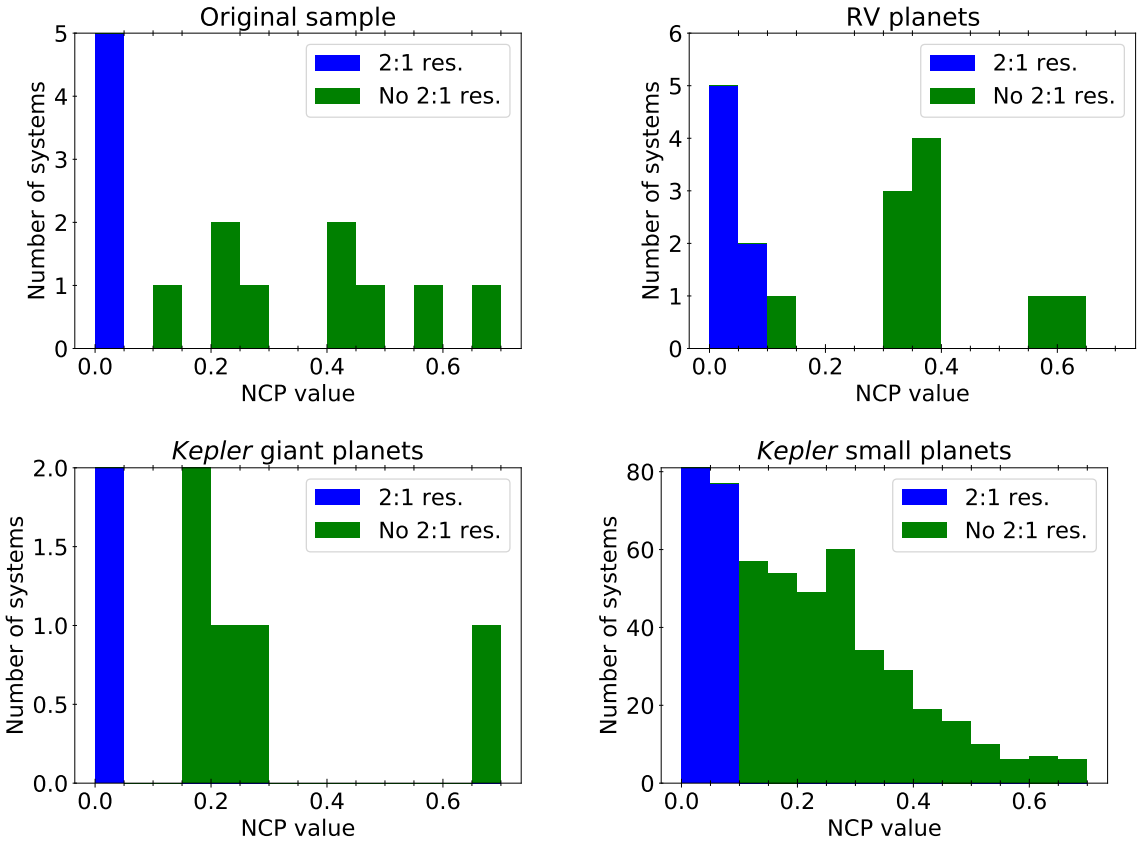

Figure 3.3. Histograms of NCP values for the original Koriski & Zucker (2011) sample (upper left), massive planet pairs in the RV sample (upper right), giant planet pairs in the *Kepler* sample (lower left), and small planet pairs in the *Kepler* sample (lower right). Systems near a 2:1 resonance are shown in blue, and systems without a 2:1 resonance are shown in green. These plots are focused near $\boldsymbol{\delta} = 0.1$, the threshold for being near a 2:1 resonance, and do not show every system in the samples.

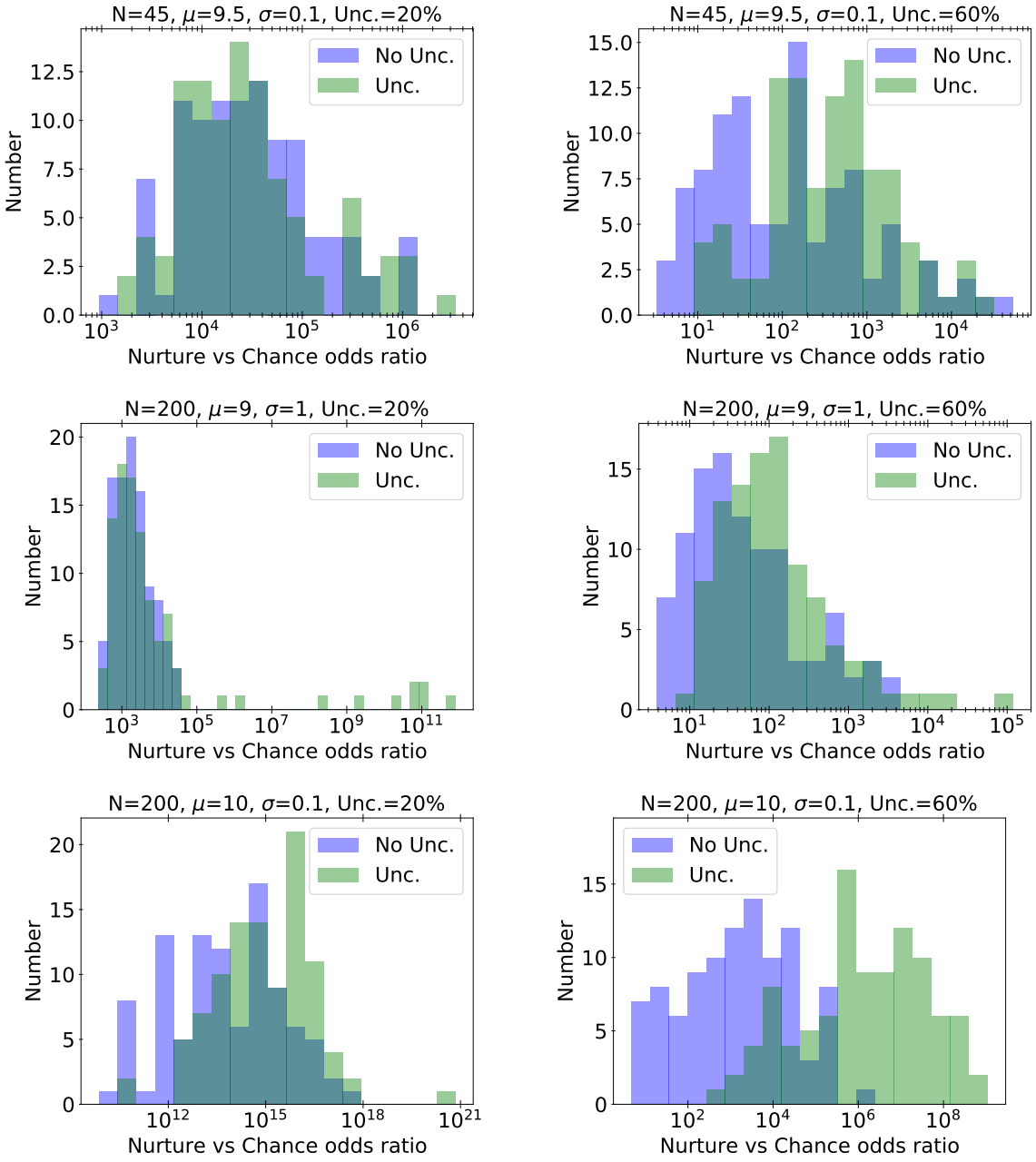

Figure 3.4. Distributions of Nurture vs. Chance odds ratios for various values of simulated dataset size N, μ, σ, and measurement uncertainty, generated from 100 "observations" of the true simulated ages. Ratios calculated without incorporating measurement uncertainties are shown in blue, and ratios calculated with incorporating uncertainties are shown in green. Note that even when uncertainties are not accounted for in the odds ratio, the level of uncertainty does affect the observed ages because we don't perfectly measure the true quantities. This is why the blue histograms differ between the left and right panels.

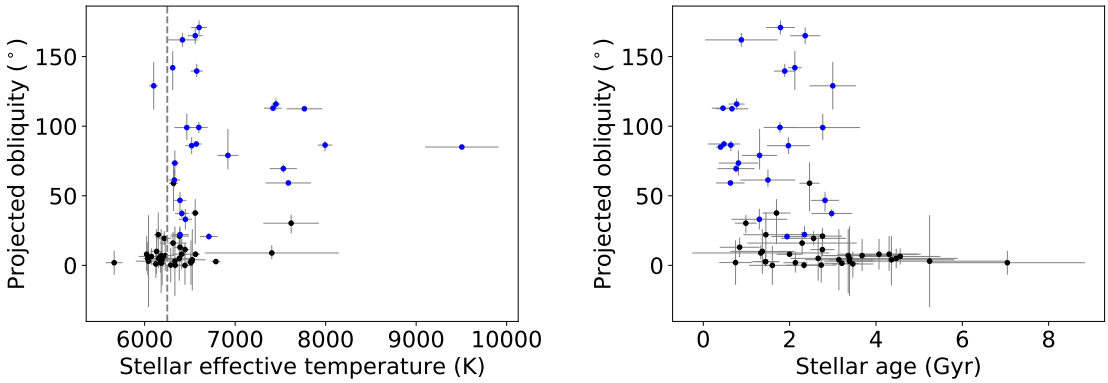

Figure 3.5. Projected obliquity (λ) versus stellar effective temperature (left) and mean age, in Gyr, from the `isochrones` program (right). Blue points represent systems that have $\lambda > 10°$ at the 3σ level, and black points represent systems that do not. The left panel also shows a dashed line at $T_{\rm eff,\star} = 6250$ K, which we use to divide the sample into "hot" and "cool" stars. Note that this sample only contains stars with $M_\star > 1.2 M_\odot$.

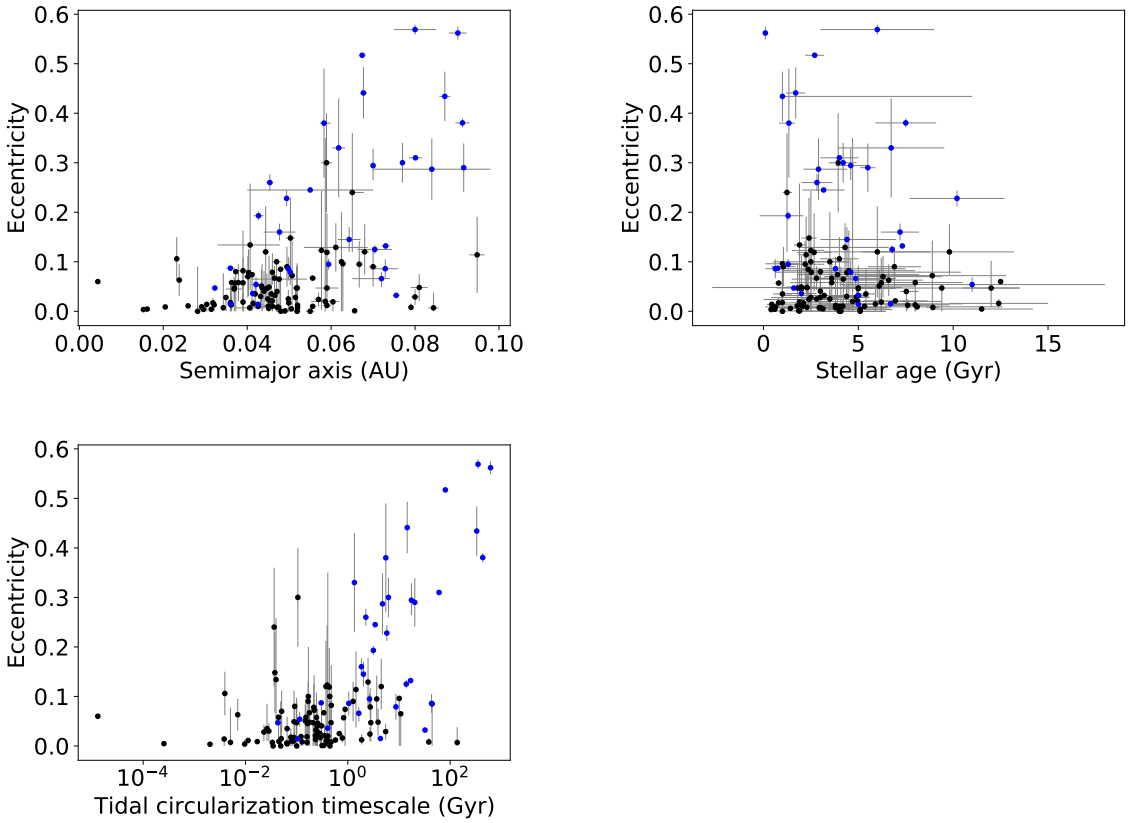

Figure 3.6. Eccentricity (e) versus semimajor axis (upper left), age in Gyr (upper right), and tidal circularization timescale in Gyr (lower left) for the sample of hot Jupiters we analyze in the eccentricities case. Blue points represent systems that have $e > 0$ at the 3σ level, and black points represent systems that do not.

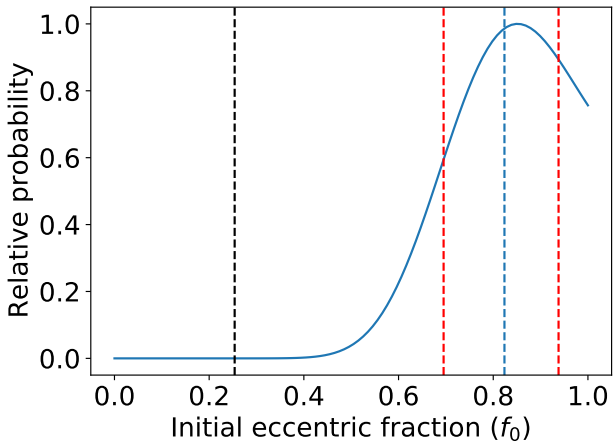

Figure 3.7. Posterior probability histogram of the initial eccentric fraction f_0, normalized such that the highest probability is 1. The median is shown by the dashed blue line, and the red dashed lines mark the 68% confidence interval. For reference, the observed eccentric fraction is shown by the black dashed line; since the Nurture hypothesis involves evolution over time, we do not expect the observed eccentric fraction to match up with the median value for f_0.

Chapter 4
Comparing Core-Powered Mass Loss versus Photoevaporation as the Primary Sculptor of the Radius Valley with a Bayesian Statistical Framework

The text in this chapter is from a paper by E. D. Safsten and R. I. Dawson that is in preparation for submission. I performed the calculations and wrote the manuscript. R. I. Dawson advised on the project and provided significant comments.

The exoplanet radius valley is a relative scarcity of planets around ∼1.5-2 $R_\oplus$ that creates a bimodal radius distribution of small planets. It is thought that this valley separates rocky super-Earths from sub-Neptunes that have a substantial atmosphere. The most favored theories for the formation of the valley are core-powered mass loss and photoevaporation, but distinguishing between these hypotheses has been difficult because many of the predictions of each are consistent with observed data. We use a Bayesian statistical framework to compute an odds ratio for these two hypotheses using the data from the California-*Kepler* Survey (CKS), in which the radius gap was first observed and to which studies of photoevaporation and core-powered mass loss compared their simulations, as well as the more recent data from the *Gaia-Kepler-TESS*-Host Stellar Properties (GKTH) catalog. The results from the CKS sample depend on the assumptions regarding core mass and initial atmospheric mass fraction and the sample cuts used. The

data strongly favor core-powered mass loss when we follow the respective prescriptions for core mass and initial atmospheric mass fraction from studies on photoevaporation and core-powered mass loss, but tend to favor photoevaporation or be inconclusive when we use other assumptions. On the other hand, the GKTH data very strongly support core-powered mass loss regardless of these assumptions. We do see a dependence of our results on stellar temperature and orbital period, where core-powered mass loss is preferred at the shortest orbital periods, while results at longer periods either favor photoevaporation or are inconclusive, depending on stellar temperature.

4.1 Introduction

One of the interesting features revealed by the analysis of planets discovered by the *Kepler* mission is the planetary radius gap. This is a relative lack of close-in (period P<100 days) planets with radius ∼1.5-2 $R_\oplus$, creating a bimodal distribution of planetary radii between ∼1-4 $R_\oplus$ (Fulton et al., 2017; Berger et al., 2018; Van Eylen et al., 2018; Fulton & Petigura, 2018; Martinez et al., 2019). It is generally thought that this gap separates the super-Earths – bare rocky cores – from the sub-Neptunes, which are believed to have substantial atmospheres composed primarily of hydrogen and helium.

Several theories have been developed to explain the existence of the radius gap. Two of the most favored are photoevaporation (Owen & Wu, 2013, 2017) and core-powered mass loss (Ginzburg et al., 2018; Gupta & Schlichting, 2019, 2020). Both of these mechanisms cause the erosion of planetary atmospheres after formation, turning planets born as sub-Neptunes into super-Earths. Photoevaporation is driven by high-energy stellar radiation and primarily occurs over the first ∼100 Myr, when the star is most active, though it can continue at later times. Core-powered mass loss is driven by the energy emitted by the planetary core as it cools after formation and is expected to take place over several gigayears. (Note that we use the term "core" to refer to the non-gaseous part of a planet.) Other sources for the valley have been proposed, such as mass loss from planetesimal impacts (Wyatt et al., 2020) or that it forms primordially (e.g. Lee & Connors 2021; Lee et al. 2022), but for now we will just focus on core-powered mass loss and photoevaporation.

Observed relations between the radius gap and other stellar or planetary quantities can offer clues about the dominant mechanism shaping the gap, but this is more difficult when some of the predictions of different processes are similar. The location of the radius gap is observed to decrease with orbital period, with a slope of approximately

$d\log R_{\rm p}/d\log P \sim -0.09$ (Van Eylen et al., 2018; Martinez et al., 2019; David et al., 2021; Petigura et al., 2022), turning the gap into a valley in planetary radius-period space. Both core-powered mass loss and photoevaporation predict radius-period slopes consistent with measured values (Owen & Wu, 2017; Gupta & Schlichting, 2019). Berger et al. (2020a) observed a dependence of the location of the radius gap on stellar mass, fitting a slope of $d\log R_p/d\log M_\star = 0.26^{+0.21}_{-0.16}$ to the valley. Petigura et al. (2022) found a similar slope of $0.18^{+0.07}_{-0.08}$. Under the photoevaporation model, such a dependence can exist if there is a relation between planetary core mass and stellar mass (Wu, 2019). Because of its dependence on stellar luminosity, core powered mass loss predicts a slope of about 0.33 (Gupta & Schlichting, 2020). Both mechanisms can thus be compatible with the observed stellar mass relation.

David et al. (2021) examined how the planetary radius distribution and the location of the radius valley change over time. They noted different radius distributions of young and old planets and found that, due to an absence of large super-Earths at young ages, the location of the valley for younger planets is at a smaller radius than for older planets. They found a gigayear timescale for the evolution of the valley. Sandoval et al. (2021) also studied how the radius distribution evolves over time, specifically by looking at the ratio of super-Earths to sub-Neptunes at different stellar ages, and found the ratio to increase with age from 1 to 10 Gyr. This agrees with the results of Berger et al. (2020a), who found the ratio of super-Earths to sub-Neptunes to be 0.61 ± 0.09 for stars younger than 1 Gyr and 1.00 ± 0.10 for stars older than 1 Gyr. These studies point to planetary radius evolution on gigayear timescales, which, though more in line with the predictions of core-powered mass loss, is compatible with both atmospheric loss processes. Furthermore, the relative paucity of known planets with very young ages makes it difficult to observe a significant change in the radius distribution on timescales less than 1 Gyr.

Both photoevaporation and core-powered mass loss satisfactorily reproduce the observed radius-period distribution of super-Earths and sub-Neptunes and are also compatible with the observed stellar mass and age dependencies, leaving it unclear which mechanism may play the dominant role in shaping the distribution. Rogers et al. (2021) attempted to answer this question by studying the observed gap in the three-dimensional radius-stellar-mass-incident bolometric flux space. They defined parameters describing the gap in 3D space, specifically, the slope of the valley with bolometric flux at fixed stellar mass, and the slope of the valley as a function of stellar mass at fixed incident bolometric flux. The latter, in particular, they predicted to be different for photoevaporation and core-powered mass loss. They calculated these 3D parameters for

both the California-*Kepler* survey (CKS; Fulton et al. 2017; Fulton & Petigura 2018) and the *Gaia-Kepler* Survey (GKS; Berger et al. 2020a). However, with the level of uncertainty in the data, the measured 3D parameters were consistent with the predictions of both models, and their results were inconclusive. Berger et al. (2023b) repeated the analysis using the updated stellar and planetary parameters of the *Gaia-Kepler-TESS*-Host Stellar Properties (GKTH) catalog (Berger et al., 2023a) and found the values of the measured 3D parameters to be consistent with those predicted by core-powered mass loss, but not with those predicted by photoevaporation.

Here, we take another approach to comparing the evidence for photoevaporation versus core-powered mass loss. We use the Bayesian statistical framework developed in Safsten et al. (2020), which is designed to compare the evidence for two hypotheses that are potential explanations for observed trends between planetary and stellar properties. The trend we examine is the increase in the ratio of super-Earths to sub-Neptunes with stellar age. Photoevaporation and core-powered mass loss are the hypotheses we compare, and we compute the relative evidence for each using two available samples. We describe our method in Section 4.2 and our results in Section 4.3. We discuss our findings in Section 4.4, and we conclude in Section 4.5.

4.2 Method

4.2.1 Bayesian Framework

In Safsten et al. (2020), we developed a Bayesian statistical framework designed to compare hypotheses for observed trends between planetary and stellar properties. The framework is intended to address questions of the true, underlying cause of observed correlations, particularly between planetary properties and stellar ages. Such questions can occur because stellar ages are correlated with other stellar properties, meaning that a trend might be observed both between a planetary property and stellar age, and between the planetary property and another stellar parameter, leaving the fundamental source of the correlation unclear. In other cases, there may be doubt that a supposed trend actually exists. More generally, the framework may be used to compare any pair of hypotheses to see which one better describes the observed data. The comparison is made with an odds ratio, a ratio of the evidences for two hypotheses $H_{\rm A}$ and $H_{\rm B}$ given the available data. The evidence for each hypothesis is computed from the product of individual system likelihoods (under a given hypothesis), marginalization over hyperparameters $\mathbf{Y}$

(population-wide, rather than system-specific, parameters), and priors assigned to each hypothesis $p(H_{\rm A})$ and $p(H_{\rm B})$, as follows:

$$\frac{p(H_{\rm A}|\{X_{\rm p,i}, t_{\star,{\rm i}}, \mathbf{X}_{\rm ob,i}\})}{p(H_{\rm B}|\{X_{\rm p,i}, t_{\star,{\rm i}}, \mathbf{X}_{\rm ob,i}\})} = \frac{\int[\prod_{\rm i} p(X_{\rm p,i}, t_{\star,{\rm i}}, \mathbf{X}_{\rm ob,i}|\mathbf{Y}, H_{\rm A})]p(\mathbf{Y})d\mathbf{Y}}{\int[\prod_{\rm i} p(X_{\rm p,i}, t_{\star,{\rm i}}, \mathbf{X}_{\rm ob,i}|\mathbf{Y}, H_{\rm B})]p(\mathbf{Y})d\mathbf{Y}} \frac{p(H_{\rm A})}{p(H_{\rm B})} \tag{4.1}$$

where $X_{\rm p}$ is the observed property of interest of the planet, $t_\star$ is the age of the star, and $\mathbf{X}_{\rm ob}$ contains other observed system quantities relevant to the problem (e.g., stellar temperature, planetary orbital period). $\{X_{\rm p,i}, t_{\star,{\rm i}}, \mathbf{X}_{\rm ob,i}\}$ represents the observed data, with the i subscript denoting an individual planet, star, or system (we will hereafter omit this subscript). We will give equal weight to each hypothesis we consider, so $p(H_{\rm A})/p(H_{\rm B}) = 1$. Then, for each system and each hypothesis, we need to find the individual system likelihood $p(X_{\rm p,i}, t_{\star,{\rm i}}, \mathbf{X}_{\rm ob,i}|\mathbf{Y})$, the probability of a system existing with a certain configuration given the hyperparameter(s).

In Safsten et al. (2020), we described three types of hypotheses that might explain an observed correlation between planetary and stellar properties: the Nurture hypothesis, in which a planetary property is due to the stellar age and therefore evolves over time; the Nature hypothesis, in which a planetary property is due to some other property of the star, such as effective temperature, pointing to formation environment being important; and the Chance hypothesis, in which the planetary property is independent of observed parameters and any observed correlation is merely coincidental. For each hypothesis, we derived equations for the individual system likelihood. In some applications, the planetary property of interest $X_{\rm p}$ may be considered as a binary parameter, i.e. it can only take on one of two discrete values. This is the model we will employ here: we will only consider whether a planet's measured radius classifies it as a super-Earth or a sub Neptune, according to the location of the radius valley, without further regard to its actual value.

We can classify both photoevaporation and core-powered mass loss as versions of the Nurture hypothesis, because each process involves the loss of a planet's envelope over time. The key differences are the mechanisms driving the loss and thus the timescales over which they take place. Therefore, the odds ratio we calculate will be a comparison of two distinct Nurture hypotheses. We will also compare each Nurture hypothesis with the Chance hypothesis. However, we do not consider a Nature hypothesis in this work. We note that other explanations for the radius valley may be described by a Nature hypothesis, where a planet's existence as a super-Earth or a sub-Neptune is governed by

some other observed parameter, such as stellar mass. We leave the exploration of these possibilities to future work.

An important consideration is the uncertainties on measured parameters, particularly stellar ages, which tend to have large uncertainties. The original Bayesian framework described in Safsten et al. (2020) did not formally account for uncertainties. In Safsten & Dawson (2022), we did include uncertainties and showed that doing so did not change any of the conclusions reached for the particular applications in Safsten et al. (2020). Since formally accounting for measurement uncertainties can lead to a substantial increase in computation time, we opt to leave them out of the equations here, but we will later incorporate uncertainties in planetary radius in Section 4.3.

Figure 4.1 shows planetary radius versus orbital period for the two datasets we use, the CKS sample (Fulton et al., 2017) and the GKTH sample (Berger et al., 2023a), along with the location of the radius valley as determined by Van Eylen et al. (2018). The planetary property of interest here is whether or not a planet lies above or below the radius valley. We represent this with the binary parameter V, where V=1 if the planet is above the valley and V=0 if the planet is below the valley. Further, we assume that V can only evolve from 1 to 0, i.e. a planet below the valley will not later on accrete a substantial atmosphere and jump to the upper side of the valley. The transition across the valley happens on the total atmospheric loss timescale $t_{\dot{X},\text{total}}$. This parameter is distinct from the $t_{\dot{X}}$ parameter in Owen & Wu (2017) and the t_{loss} parameter in Gupta & Schlichting (2019, 2020) as these latter terms are derived from the instantaneous mass-loss rate and change as the planet evolves and the atmospheric mass fraction decreases. Here, we are interested in the time it takes a planet to completely lose its atmosphere – or, at least, lose enough that the remnant is negligible, which we take to occur at a mass fraction of 10^{-6} (see Ginzburg et al. 2018). Applying Equation 8 from Safsten et al. (2020), the individual system likelihoods for both photoevaporation and core-powered mass loss are given by

$$p(V, t_\star, \mathbf{X}_{\text{ob}}|f_0) = \begin{cases} \int \left[(1-f_0) + f_0 \int_0^{t_\star} p(t_{\dot{X},\text{total}}|V_0, \mathbf{X}_{\text{nob}}) dt_{\dot{X},\text{total}}\right] & \\ p(t_\star, \mathbf{X}_{\text{ob}}, \mathbf{X}_{\text{nob}}) d\mathbf{X}_{\text{nob}} & , V = 0 \\ f_0 \iint_{t_\star}^{\infty} p(t_{\dot{X},\text{total}}|V_0, \mathbf{X}_{\text{nob}}) & \\ p(t_\star, \mathbf{X}_{\text{ob}}, \mathbf{X}_{\text{nob}}) dt_{\dot{X},\text{total}} d\mathbf{X}_{\text{nob}} & , V = 1, \end{cases} \tag{4.2}$$

where $t_\star$ is the stellar age, V_0 is the initial value of V, and f_0 is the fraction of small, close-in planets that form as sub-Neptunes. The terms $\mathbf{X}_{\text{ob}}$ and $\mathbf{X}_{\text{nob}}$ contain other

observed and unobserved parameters, respectively, that are relevant to the problem.

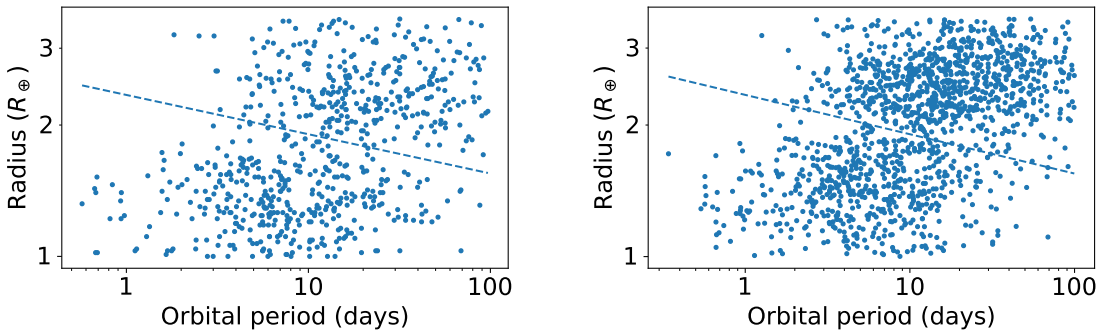

Figure 4.1. Radius vs period for CKS sample (left) and GKTH sample (right). The location of the middle of the radius valley, from the equation of Van Eylen et al. (2018), is shown as a dashed line.

However, $t_{\dot{X},\text{total}}$ is difficult to parameterize, since the mass-loss rate changes over time. Instead, we rewrite the above equation in terms of X_0, the planet's initial atmospheric mass fraction:

$$p(V, t_\star, M_\star, P|f_0) = \begin{cases} (1-f_0) + f_0 \iint_{X_{0,\text{min}}}^{X_{0,\text{crit}}} p(X_0|V_0, M_\text{c}, M_\star, P) \\ p(X_0, t_\star, M_\star, P, M_\text{c}) dX_0 dM_\text{c} & , V=0 \\ f_0 \iint_{X_{0,\text{crit}}}^{X_{0,\text{max}}} p(X_0|V_0, M_\text{c}, M_\star, P) \\ p(X_0, t_\star, M_\star, P, M_\text{c}) dX_0 dM_\text{c} & , V=1, \end{cases} \tag{4.3}$$

$X_{0,\text{crit}}$ represents the initial atmospheric mass fraction such that $t_{\dot{X},\text{total}} = t_\star$. $X_{0,\text{min}}$ and $X_{0,\text{max}}$ represent the lower and upper bounds, respectively, of the prior on X_0. In other words, the top line says that a planet observed to be a super-Earth (V=0) must have formed with no more atmospheric gas than what could be lost during the planet's life up to this point. Similarly, a sub-Neptune (V=1) must have formed with at least the amount of gas that could be lost during its life up to this point, in order for us to observe it having a substantial atmosphere.

In Eqn. 4.3, we have also included the planetary core mass M_c, as this is also an important factor in a planet's mass-loss rate. Both M_c and X_0 are unobserved parameters, so we marginalize over them. Observed parameters that affect the atmospheric loss timescale are the stellar mass $M_\star$ and the planetary orbital period P. Together, $M_\star$ and P determine the amount of energy the planet gets from the star, which is important in both mass-loss processes in setting the temperature and structure of the atmosphere, and

which is additionally important for photoevaporation in determining the high-energy flux the planet receives. We assume that the distributions of $t_\star$, $M_\star$, and P are independent of the other parameters in our models. The priors on $t_\star$, P and $M_\star$ can then be pulled out of the integrals, and they will cancel out when we take the odds ratio, so we do not need to specify their form. We give the initial fraction of sub-Neptunes f_0 a uniform hyperprior from 0 to 1.

In our analysis, the primary difference between core-powered mass loss and photoevaporation comes in the value of $X_{0,\mathrm{crit}}$ for each planet that is required in order for the total mass-loss time $t_{\dot{X},\mathrm{total}}$ to be equal to the age of the star. In the following subsections, we will describe each process and its associated parameters in further detail.

4.2.2 Photoevaporation

The photoevaporation model describes the erosion of planetary atmospheres by extreme ultraviolet and X-ray (XUV) radiation from their host stars. Young stars ($\lesssim$100 Myr old; Jackson et al. 2012), being more active, produce a relatively large amount of these high-energy photons. Over time, exposure to this radiation can imbue a planetary atmosphere with enough energy to cause it to escape from the planet; for close-in planets with hydrogen and helium (H/He) atmospheres, this can strongly, and in some cases completely, erode the atmosphere (see, e.g., Lammer et al. 2003; Baraffe et al. 2004; Murray-Clay et al. 2009; Owen & Jackson 2012). Because some planetary atmospheres are more resistant to photoevaporative erosion than others due to their orbital period, core mass and composition, and host star mass, several studies predicted that photoevaporation would lead to a bimodal radius distribution (e.g. Owen & Wu 2013; Lopez & Fortney 2013; Jin et al. 2014; Chen & Rogers 2016).

The mass-loss timescale is defined as

$$t_{\dot{X}} \equiv \frac{X}{\dot{X}} = \frac{M_{\mathrm{env}}}{\dot{M}_{\mathrm{env}}} \tag{4.4}$$

where $\dot{M}_{\mathrm{env}}$ is the mass-loss rate of the atmosphere. The atmospheric mass fraction of a planet evolves according to the differential equation

$$\frac{dX}{dt} = -\frac{X}{t_{\dot{X}}}. \tag{4.5}$$

We use the equations and assumptions of Owen & Wu (2017) to calculate $\dot{M}_{\mathrm{env}}$ and evolve planetary atmospheres, and we refer the reader to that work for further details.

To determine each planet's $X_{0,\mathrm{crit}}$, we use `scipy.integrate.solve_ivp` to integrate Equation 4.5 backwards from the planet's observed age, with $X{=}10^{-6}$ at the current age as the value of the atmospheric mass fraction at which the planet is considered to be a super-Earth. At this threshold, and given uncertainties in planetary radius, the atmosphere adds a negligible contribution to a planet's radial size. This value is also motivated by Ginzburg et al. (2018), who used this threshold in their Figure 4, and by Owen & Wu (2017), because it is below the range used in the schematic in their Figure 6. As a check, we integrate the differential equation forward from $t = 0$ with initial atmospheric mass fractions of the calculated $X_{0,\mathrm{crit}}$ values and obtain total mass-loss times within 6% of the measured ages for each of the samples we analyze.

The value of $X_{0,\mathrm{crit}}$ depends on the planet's core mass, M_c. This is an unobserved parameter that we must marginalize over. We calculate $X_{0,\mathrm{crit}}$ for a grid of M_c values ranging from 0.5-20 $M_\oplus$, then interpolate between these values to get $X_{0,\mathrm{crit}}$ as a function of M_c.

Since we will marginalize over X_0 and M_c, we need to specify priors for them. We follow Owen & Wu (2017), who used a Rayleigh distribution for the core mass

$$\frac{dN}{dM_\mathrm{c}} \propto M_\mathrm{c} \mathrm{exp}^{-M_\mathrm{c}^2/2\sigma_M^2} \tag{4.6}$$

with a scale parameter $\sigma_M{=}3\ M_\oplus$. This choice of distribution was based on earlier studies (e.g. Howard et al. 2010; Mayor et al. 2011; Marcy et al. 2014) that measured masses for *Kepler* planets. In particular, the planetary masses found by Marcy et al. (2014) could be roughly described by a Rayleigh distribution with $\sigma_M{\sim}5\ M_\oplus$, but Owen & Wu (2017) point out that the sample used was likely biased towards higher masses, which is why they opted for a smaller scale parameter. For the initial atmospheric mass fraction X_0, they used a log-uniform distribution from $X_0{=}0.01$ to $X_0{=}0.3$, which is independent of the core mass. We note that Rogers & Owen (2021) used Bayesian inference and forward models of photoevaporation in an effort to constrain the characteristics of the population of newly formed planets (assuming photoevaporation to be the primary driver of atmospheric loss). They fit the M_c and X_0 distributions that would produce the radius distribution of planets seen today and found the best fit to come from using 5th-order Bernstein polynomials for each; however, they did not report the coefficients that they found provided the best fit, so we use the Owen & Wu (2017) distributions here.

4.2.3 Core-powered mass loss

Under core-powered mass loss, atmospheric escape is driven by internal heat left from a planet's formation. Ginzburg et al. (2016) described what happens to planetary atmospheres after protoplanetary disk dispersal and the consequent rapid loss of gas from the planetary envelope due to the loss of pressure support (see also Owen & Wu 2016). If the atmosphere is light (mass fraction less than $\sim$5%), then the heat capacity of the core dominates that of the envelope, and the cooling core drives the loss of the atmosphere. Heavy atmospheres, on the other hand, cool without losing much mass, so the planet retains a substantial envelope. This leads to a bimodal distribution of final planetary radii. Ginzburg et al. (2018) demonstrated how core-powered mass loss can reproduce the observed radius gap. Subsequent works have shown how this process also leads to the observed orbital period (Gupta & Schlichting, 2019) and stellar mass (Gupta & Schlichting, 2020) dependencies of the radius gap.

The equations for core-powered mass loss (Ginzburg et al., 2016, 2018; Gupta & Schlichting, 2019, 2020) describe how a planet's energy and atmospheric mass evolve over time as the planet cools and its internal energy causes the envelope to lose mass. As in the photoevaporation case, we are interested in the total time it takes a planet to lose its entire atmosphere under core-powered mass loss, leading us to Eqn. 4.2 for the individual system likelihood. We again wish to reparameterize this equation. In the calculations performed by Ginzburg et al. (2018), Gupta & Schlichting (2019), and Gupta & Schlichting (2020), the initial atmospheric mass fraction is assumed to be directly connected to the core mass as follows:

$$X_0 = 0.05(M_c/M_\oplus)^{1/2}. \tag{4.7}$$

This is based on the work of Ginzburg et al. (2016) on the results of planetary gas accretion and gas disk dispersal. This assumption means that every value for $X_{0,\mathrm{crit}}$ directly corresponds to a core mass value. Therefore, instead of reparameterizing in terms of $X_{0,\mathrm{crit}}$, we write Eqn. 4.2 in terms of $M_{c,\mathrm{crit}}$, the core mass that a planet must have in order for its total atmospheric loss time, under core-powered mass loss, to be equal to

the planet's age. This gives the following:

$$p(V, t_\star, M_\star, P|f_0) = \begin{cases} (1-f_0) + f_0 \int_{M_{\rm c,min}}^{M_{\rm c,crit}} p(M_{\rm c}|V_0, M_\star, P) \\ p(t_\star, M_\star, P) dM_{\rm c} & , V = 0 \\ f_0 \int_{M_{\rm c,crit}}^{M_{\rm c,max}} p(M_{\rm c}|V_0, M_\star, P) \\ p(t_\star, M_\star, P) dM_{\rm c} & , V = 1. \end{cases} \tag{4.8}$$

Because of the assumed connection between X_0 and $M_{\rm c}$ in Eqn. 4.7, $M_{\rm c,crit}$ implicitly sets $X_{0,\rm crit}$, and the integral over X_0 is removed.

We use the equations and assumptions of Ginzburg et al. (2018), Gupta & Schlichting (2019), and Gupta & Schlichting (2020) to solve for $M_{\rm c,crit}$ for each planet, and we refer the reader to those works for further details. We do this by calculating total mass-loss times for various values of $M_{\rm c}$ and using a bisection algorithm to find which value of $M_{\rm c}$ gives a total evaporation time equal to the planet's age. As a check, we follow the equations forward with planetary core masses of the calculated $M_{\rm c,crit}$ values. This results in total mass-loss times that are within 5% of the measured ages for the samples we use.

For the prior on core mass, $p(M_{\rm c}|V_0, M_\star, P)$, we use the same distribution as Gupta & Schlichting (2019) and Gupta & Schlichting (2020):

$$\frac{{\rm d}N}{{\rm d}M_{\rm c}} \propto \begin{cases} M_{\rm c} {\rm exp}(-M_{\rm c}^2/(2\sigma_M^2)) & , M_{\rm c} < 5M_\oplus \\ M_{\rm c}^{-2} & , M_{\rm c} > 5M_\oplus, \end{cases} \tag{4.9}$$

This is a Rayleigh distribution for cores less massive than $5M_\oplus$ and an inverse square distribution for cores more massive than this. The Rayleigh scale parameter σ_M is set to $2.7M_\oplus$, similar to that used by Owen & Wu (2017). Ginzburg et al. (2018) point out that the inverse square tail provides a better match to the observed high-mass tail from Marcy et al. (2014) than the Rayleigh distribution does. In Section 4.3, we will explore how the different core mass assumptions affect our results.

4.2.4 Chance (independent of observed parameters)

The comparison of the photoevaporation and core-powered mass loss hypotheses with each other will indicate which one does a better job describing the observed data, given our prior knowledge and assumptions. We also compare each of those with a Chance hypothesis, in which whether a planet forms as a super-Earth or sub-Neptune is independent of observed properties, and the planets do not experience any evolution over

time. The comparison of core-powered mass loss and photoevaporation with Chance will indicate whether each evolutionary hypothesis does a better job describing the data than an age-independent hypothesis.

Under the Chance hypothesis, whether a planet is observed to be a super-Earth or a sub-Neptune is not related to any other observed parameters. It is only governed by the hyperparameter f, the overall fraction of small, close-in planets that are sub-Neptunes. This gives the following equation for the individual system likelihood:

$$p(V, t_\star, M_\star, P|f) = \begin{cases} (1-f)p(t_\star, M_\star, P) & , V = 0 \\ f_0 p(t_\star, M_\star, P) & , V = 1. \end{cases} \tag{4.10}$$

We give f a uniform hyperprior from 0 to 1.

In Figure 4.2, we display a graphical representation of our models. Observed parameters are displayed in gray circles, and unobserved parameters, which we marginalize over, are shown in white circles. We show the relationships between relevant parameters under each hypothesis, using a solid blue arrow for photoevaporation, a dashed red arrow for core-powered mass loss, and a dotted green arrow for Chance.

4.3 Results

Here we compute the odds ratios for different variations of the photoevaporation, core powered mass loss, and Chance hypotheses. In interpreting the odds ratios, we follow a scale similar to that of Jeffreys (1961) and Kass & Raftery (1995): we consider a ratio of $\sim$1-10 to be inconclusive, $\sim$10-100 to be moderately supportive but not decisive, and $\sim$100 and above to be strongly supportive.

We begin by using the CKS sample of planets and stellar ages, a sample derived from high-precision spectroscopy of *Kepler* planet hosts which enabled precise determination of planet properties (Petigura et al., 2017; Johnson et al., 2017; Fulton et al., 2017). This is the data to which both the photoevaporation (Owen & Wu, 2017) and core-powered mass loss (Ginzburg et al., 2018; Gupta & Schlichting, 2019, 2020) studies compared their models. From the full CKS dataset, the sample contains 900 planets after removing false positives (as determined by Petigura et al. 2017), stars with a *Kepler* magnitude Kp>14.2 (eliminating a few fainter hosts of interesting planetary systems that supplemented the main, magnitude-limited CKS sample), planets with impact parameter b>0.7, stars with $T_\star$<4700 K or $T_\star$>6500 K, evolved stars, and planets with orbital period beyond P=100

days. The application of these filters results in a sample of sun-like main sequence stars with well-determined properties, hosting planets with well-determined radii. We further pare down the sample to super-Earths and sub-Neptunes by removing planets with $R_{\rm p}$<1 $R_{\oplus}$ or $R_{\rm p}$>3.5 $R_{\oplus}$, the cuts used by Berger et al. (2020a). This leaves us with 683 planets.

To determine whether a given planet in the sample should be considered as a sub-Neptune (V=1) or a super-Earth (V=0), we use the period-dependent relation for the location of the radius valley calculated by Van Eylen et al. (2018). If a planet's observed radius and period put it above this line, we classify it as a sub-Neptune; if it is below this line, we classify it as a super-Earth (see Figure 4.1).

We obtain the following odds ratios for the CKS sample, where $p(H_{\rm cpml})$, $p(H_{\rm pe})$, and $p(H_{\rm ch})$ are the probabilities for the core-powered mass loss, photoevaporation, and Chance hypotheses, respectively:

$$\frac{p(H_{\rm cpml})}{p(H_{\rm pe})} = 102$$
$$\frac{p(H_{\rm pe})}{p(H_{\rm ch})} = 1.65 \times 10^{36}$$
$$\frac{p(H_{\rm cpml})}{p(H_{\rm ch})} = 1.69 \times 10^{38}.$$

We find strong support for core-powered mass loss over photoevaporation as the dominant mechanism shaping the radius distribution of super-Earths and sub-Neptunes. We note, though, that this conclusion is dependent on the model assumptions and sample cuts we use. We explore the impact of these factors in Sections 4.3.1 and 4.3.2. Additionally, both mechanisms are overwhelmingly favored over a chance relation.

Second, we use the *Gaia-Kepler-TESS*-Host Stellar Properties Catalog (GKTH; Berger et al. 2023a), an updated version of the GKS (Berger et al., 2020b,a) catalog, which used *Gaia* DR3 data along with isochrone fitting to derive homogeneous parameters for *Kepler*, *K2*, and *TESS* stars and planets. We calculate the odds ratios for the confirmed *Kepler* planets in this data, applying the same period, planetary radius, stellar temperature, and stellar evolution criteria as before and removing planets with grazing transits, which leaves us with 1433 planets. This gives the following:

$$\frac{p(H_{\rm cpml})}{p(H_{\rm pe})} = 8.02 \times 10^{30}$$
$$\frac{p(H_{\rm pe})}{p(H_{\rm ch})} = 1.57 \times 10^{65}$$

$$\frac{p(H_{\rm cpml})}{p(H_{\rm ch})} = 1.26 \times 10^{96}.$$

The data once again clearly support core-powered mass loss over photoevaporation, as well as both evolutionary processes over chance. We also ran the calculations with the GKS sample and reached the same conclusions.

Part of the reason for these strong odds ratios is the sizes of each of our samples. The CKS sample has 683 planets, and the GKTH sample is more than twice as large. If every planet in the sample has a small preference for one hypothesis, this could turn into a strong preference when taken all together. Considering the approximate nature of our models, this means that these large ratios may not be as impactful as if we had obtained the same result with a much smaller sample. We examine this more in Section 4.3.1.

In Figures 4.3 and 4.4, we show plots of the individual system likelihoods as a function of orbital period, colored by stellar age and stellar mass respectively, for the CKS data under the photoevaporation and core-powered mass loss hypotheses, with $f_0 = 1$. Figures 4.5 and 4.6 show the same thing for the GKTH sample. Planets classified as sub-Neptunes are shown as triangles, and those classified as super-Earths are shown as circles. It is these probabilities which are multiplied together in the product in Eqn. 4.1 (for a given value of f_0). For both mechanisms, we see the clear preference of super-Earths close to the star as well as the significant weakening of the mass loss by orbital periods of 30 days. Both of these effects seem to be more pronounced for photoevaporation than for core-powered mass loss. We can also see the dependence on stellar mass. Sub-Neptunes around higher mass stars have slightly lower probability than those that orbit less massive hosts, because in both processes a more massive (and therefore hotter) star provides more energy to the atmosphere, accelerating its escape. This is also likely the cause of the less-prominent age dependence, in which sub-Neptunes around younger stars have slightly lower probabilities, because more massive stars have shorter lifetimes. An analogous trend is seen with the super-Earths.

4.3.1 Variation of Priors

We test the sensitivity of our results to the priors assumed for the core mass and initial atmospheric mass fraction. The original models for photoevaporation and core-powered mass loss make different assumptions about the planet formation process; namely, core-powered mass loss assumes a connection between the core mass and the initial atmospheric mass fraction (leading us to use $M_{\rm c,crit}$ for the individual likelihoods),

but photoevaporation assumes they are independent (leading us instead to use $X_{0,\mathrm{crit}}$ for the individual likelihoods). Each model also assumes a different core mass distribution. We have followed these original prescriptions for our first calculations. Next, we compute the odds ratios where both photoevaporation and core-powered mass loss assume a link between core mass and initial atmospheric mass fraction and where the core masses are distributed according to Eqn. 4.9, i.e., the assumptions made by the core-powered mass loss studies. We will refer to this as Variation 1. We also compute the odds ratios where both models assume that the core mass and initial atmospheric mass fraction are independent, and that the core mass distribution is given by Eqn. 4.6, i.e., the assumptions made by the photoevaporation study. We will call this Variation 2.

In both Variations 1 and 2, the GKTH sample still very strongly supports core-powered mass loss over photoevaporation. However, the CKS sample instead strongly favors photoevaporation in both variations.

To get a sense of the influence of the core mass distribution versus the assumed connection between M_c and X_0, we use Eqn. 4.9 as the core mass distribution for both core-powered mass loss and photoevaporation, but keep the original assumptions about the link between M_c and X_0 (i.e. assuming a link in the core-powered mass loss hypothesis, but not in the photoevaporation hypothesis). We call this version Variation 3. For the CKS sample, the odds ratio again favors photoevaporation, but only moderately so. The GKTH sample still strongly supports core-powered mass loss. Similarly, we use Eqn. 4.6 as the core mass distribution while keeping the original assumptions about the link between M_c and X_0. We call this final version Variation 4. For the CKS sample, the resulting odds ratio for core-powered mass loss and photoevaporation is of order unity, which does not allow us to favor one hypothesis over the other. The GKTH data again very strongly favor core-powered mass loss.

In deriving the critical initial atmospheric mass fractions and critical core masses, we assumed that a planet was considered a super-Earth if it had an atmospheric mass fraction of $<10^{-6}$. We also computed the odds ratios for the CKS sample with a super-Earth threshold of $X = 10^{-4}$ and found very little difference in the results. This is not surprising. Mass loss proceeds rapidly for very small atmospheres, so it would not take long for the mass fraction to go from 10^{-4} to 10^{-6}, and there is little difference to the total atmospheric loss time.

These variations indicate that the conclusions we draw from the CKS data depend on the prior we use for M_c as well as the assumed link between M_c and X_0. Both assumptions appear to play an important role, because in Variations 3 and 4, the odds

ratios do not strongly favor either hypothesis, while the original calculations strongly support core-powered mass loss and Variations 1 and 2 strongly favor photoevaporation. The results from the larger GKTH dataset, though, are more robust. While the actual values of the GKTH odds ratios vary substantially with different assumptions (ranging from $\sim 10^8$ to $\sim 10^{30}$), they are all strongly in favor of core-powered mass loss.

4.3.2 Variation of Sample Cuts

We also test the sensitivity of our results to the stellar temperature, planetary radius, and orbital period cuts used. First, we include all stars with $T_\star < 7900$ K (used by Berger et al. 2020a), which increases the GKTH sample size to 1739. (This temperature cut includes everything in the refined CKS data of Fulton et al. 2017, so there is no change to those results.) In the original calculation and Variations 2 and 4, the odds ratio for the GKTH sample strongly supports core-powered mass loss. Variations 3 is inconclusive, and Variation 1 strongly favors photoevaporation. Since both Variations 1 and 3 use some of the assumptions from the original core-powered mass loss calculations for both hypotheses, these results may indicate that such assumptions are more valid for photoevaporation around hotter stars than cooler stars. It could also suggest that the evolution of atmospheres for planets around hotter stars is different than for those with more Sun-like hosts.

Second, we expand the planetary radius limits and exclude planets with $R_\mathrm{p} < 0.8$ $\mathrm{R}_\oplus$ or $R_\mathrm{p} < 5$ $\mathrm{R}_\oplus$. This increases the CKS sample size to 794 planets and the GKTH sample size to 1574. For the GKTH sample, core-powered mass loss still has the strongest support with the original models as well as all variations, as does the CKS data with the original models. In Variations 1, 2, and 3, the CKS data strongly favors photoevaporation, and Variation 4 is inconclusive.

Owen & Wu (2017) posited that rocky planets beyond $\sim$30 days may constitute a separate population from those that undergo photoevaporation. Since the efficacy of photoevaporation drops significantly beyond this point (Owen & Jackson, 2012), rocky planets at these longer orbital periods may belong to a group that is born without extended envelopes. Core powered mass loss is also weak beyond orbital periods of 30 days (see, e.g. Figure 2 in Gupta & Schlichting 2019). As a third variation in the sample cuts, we only use planets with $P < 30$ days, since more distant planets may primarily reflect their formation conditions rather than the results of atmospheric evolution. This cut reduces the CKS sample to 552 planets and the GKTH sample to 1172 planets. For the CKS data, the original models again strongly support core-powered mass loss, as

does Variation 4. Variations 1 and 3 moderately support core-powered mass loss, but Variation 2 gives an odds ratio of order unity, meaning the result is inconclusive. However, core-powered mass loss always dominates with the GKTH sample.

In all versions of our calculations – varying the M_c distribution, changing the assumption about the link between M_c and X_0, and varying the parameter cuts for sample inclusion – both photoevaporation and core-powered mass loss are very strongly favored over the Chance hypothesis for all of our samples. This shows that regardless of the variations we explore, the data always strongly supports an age trend in the numbers of super-Earths and sub-Neptunes over a chance relation.

As mentioned earlier, the large sample sizes we have mean that a slight preference for one hypothesis from every planet could translate to a strongly supportive odds ratio all together. To get a sense of the effect of sample size on the conclusions, we divide each sample into several period and stellar temperature bins. The bins in period space are 0-10 days, 10-30 days, and 30-100 days. For the CKS sample, the stellar temperature bins are 4700-5200 K, 5200-5800 K, and 5800-6500 K, while for the GKTH sample we use these same bins as well as <4700 K, 6500-7200 K, and 7200-7900 K. We recompute the odds ratio for each bin. The results are displayed in Figure 4.7.

The bins that moderately or strongly favor one hypothesis tend to be those with more than 100 planets, but this is not the rule. There are several bins that have less than 100 planets but do favor one hypothesis over the other. This strengthens our confidence that the preference is indeed significant, rather than merely the accumulation of many marginal preferences. These figures also give a sense of how the dominant mass-loss process changes over parameter space. It appears that core-powered mass loss is strongly favored at very short orbital periods (<10 days). Photoevaporation seems to be preferred at longer orbital periods for stellar temperatures of 5800-6500 K in the GKTH sample, and more weakly so in the CKS sample. Most of the bins, though, have inconclusive results. In many cases, this may be attributable to the small number of planets in the bin. There are bins with more than 100 planets that have inconclusive odds ratios, and these may represent regions of parameter space where core-powered mass loss and photoevaporation are indeed more evenly matched. We will continue to investigate these parameter dependencies in future work.

4.3.3 Uncertainties in Planetary Radius

Even though we do not formally incorporate measurement uncertainties in our calculations here, we wish to explore the impact that uncertainties in planetary radius may have

on our results. If a planet observed to be close to the radius valley line has a large radius uncertainty, there is a reasonable chance the planet is actually on the other side of the valley than where we observe it to be. For each planet in each of the samples, we randomly redraw radius values from a Gaussian distribution with a mean of the measured radius and standard deviation of the reported radius uncertainty. We do this 100 times. This gives us a distribution of odds ratios. For the GKTH sample, the odds ratios always strongly favor core-powered mass loss, save for some instances in Variation 2 in which the odds ratio is only moderately in favor of core-powered mass loss, inconclusive, or moderately in favor of photoevaporation.

With the CKS sample using the original models, most of the ratios strongly or moderately support core-powered mass loss, with a few that are inconclusive and a few that support photoevaporation. The ratios for Variations 1 and 3 are mostly of order unity or moderately supportive of one of the hypotheses. Variation 2 strongly supports photoevaporation, with only a few instances that favor core-powered mass loss. Variation 4 strongly favors core-powered mass loss in most of its instances, but there are some ratios that are inconclusive or supportive of photoevaporation. All of these ratio distributions encompass the conclusions reached using actual data alone. This underscores the sensitivity that the odds ratio results can have on the priors and model assumptions used. It also emphasizes the importance of precise measurements of planetary parameters.

4.3.4 Histograms

In Figures 4.8 and 4.9, we display posterior histograms of f_0, the initial fraction of sub-Neptunes, for each sample under the core-powered mass loss and photoevaporation hypotheses, along with the posterior for f, the overall fraction of sub-Neptunes, under the Chance hypothesis. The curves have been normalized to have the same area. We show the f_0 posteriors for just the original calculations for each mass-loss model. For the CKS sample, we find an initial sub-Neptune fraction of $\sim$85%. With the GKTH sample, we find that essentially all the planets started as sub-Neptunes. For both samples, the f_0 histograms for the different variations overlap significantly, except for the one for core-powered mass loss in Variation 2, which peaks around 62% and 87% for the CKS and GKTH samples, respectively.

4.4 Discussion

The odds ratios obtained with the CKS data are sensitive to the exact sample cuts used and the assumptions made about the planet formation process, namely in regard to the core mass distribution and the connection between core mass and initial atmospheric mass fraction. This leads to the question of which, if any, of the versions of the calculations may be the most accurate reflection of reality. Core-powered mass loss is favored when each mechanism follows the prescriptions of their corresponding papers; it is when we use the same formation assumptions for each model that the odds ratios give a different conclusion. However, we have no a priori reason to believe that the prescriptions of Owen & Wu (2017) used with the core-powered mass loss model of Gupta & Schlichting (2019), or that the prescriptions of Gupta & Schlichting (2019) used with the photoevaporation model of Owen & Wu (2017), would provide a good match to the CKS data. In principle, numerically evolving simulated planets under either mechanism with a different core mass distribution or a different assumption about the link between initial atmospheric mass fraction and core mass could result in poor matches to the data. We need a better understanding of the planet formation process in order to know which prescriptions to use for planetary core masses and initial atmospheric mass fractions.

On the other hand, the evidence for core-powered mass loss is much stronger than that for photoevaporation in nearly every single variation on the odds ratios that we try with the GKTH *Kepler* planets as a whole. This leads us to conclude that core-powered mass loss dominates over photoevaporation in shaping the evolution of super-Earths and sub-Neptunes in this sample. Our result agrees with that of Berger et al. (2023b), who reached their conclusion through fitting radius valley parameters in 3D radius-stellar-mass-incident bolometric flux space.

However, as Figure 4.7 shows, the dominant mechanism seems to vary across parameter space. In many of the period-stellar temperature bins, the result is inconclusive. In some cases, this may simply be due to a small number of planets in the bin. In other cases, an inconclusive result may indicate that both mass-loss mechanisms are comparably effective in that bin. In reality, we expect planets to experience both photoevaporation and core-powered mass loss; what we have done here is try to determine which of these two mechanisms is more likely to be the primary sculptor of the radius valley around FGK stars, which one is more influential in shaping the radii of super-Earths and sub-Neptunes. It is certainly possible that different processes dominate at different stellar temperatures and orbital periods, as Figure 4.7 indicates. We will delve deeper into this finding in

the future. We will also consider other mechanisms that might sculpt the radius valley. This may be particularly important for planets beyond 30 days, where both core-powered mass loss and photoevaporation significantly decrease in efficacy.

In each version of our calculations, both the CKS and GKTH data as a whole very strongly support both mass-loss hypotheses over the Chance hypothesis. We are therefore confident in saying that the radius distribution of *Kepler* super-Earths and sub-Neptunes evolves with stellar age, in agreement with other works that have found age-dependent trends (David et al., 2021; Sandoval et al., 2021; Berger et al., 2020a).

Finally, the f_0 histograms (Figures 4.8 and 4.9) suggest that most short-period Earth- to Neptune-sized planets (around FGK stars) form as sub-Neptunes. This means such planets must have formed somewhere in the disk where sufficient gas was present so that they could accrete substantial atmospheres, and that they needed to form before gas disk dispersal (thought to occur by 10 million years or so). Both Owen & Wu (2017) and Gupta & Schlichting (2019) find that the planetary cores of sub-Neptunes and super-Earths are likely to be Earth-like, with a low ice fraction. This indicates that these planets formed within the ice line, rather than forming farther out and migrating inward. If the majority of these small planets were able to obtain large gaseous envelopes at or near their current locations, this can help place constraints on the structure and evolution of protoplanetary disks.

4.5 Conclusion

In this work, we have used the framework of Safsten et al. (2020) to examine the radius valley around FGK stars and to assess whether the available data is more supportive of photoevaporation or core-powered mass loss as the primary sculptor of the valley. The conclusion we draw using the CKS data as a whole is sensitive to the exact assumptions about planet formation used, but when we use the same assumptions for each mechanism as described in their corresponding papers, we find the most support for core-powered mass loss. The posterior histogram for f_0 – the fraction of close-in Earth- to Neptune-size planets orbiting FGK stars that form as sub-Neptunes – for this sample peaks around 85%. With the parameters for *Kepler* planets from the larger GKTH sample, the evidence overwhelmingly favors core-powered mass loss over photoevaporation for nearly every variation of assumptions we try. For this sample, the peaks in the f_0 posterior histogram occur around 1, meaning nearly all close-in planets in this radius regime ($\sim$1-4 $R_\oplus$) around FGK stars are formed with substantial atmospheres.

When we look at the odds ratios in bins in stellar temperature-period space, however, we see that the conclusion we draw depends on orbital period and stellar temperature. Core-powered mass loss tends to be favored at very short (<10 days) orbital periods, while photoevaporation tends to be favored farther out for stars of about 5200-6500 K. Elsewhere, the results are inconclusive, reflecting either a lack of planets in that region of parameter space, or comparable efficacy of the two mass-loss mechanisms. We will explore this apparent parameter dependence more in future work.

We stress that these results may only be accurate as far as the assumptions we have used are correct. While we have tried a couple different assumptions about planet formation regarding the initial atmospheric mass fraction and planetary core mass distribution, there are other assumptions that we have not varied. These include the evaporation efficiency, the core composition and heat capacity, and the composition of the planetary atmosphere, among others. We have followed the prescriptions of Gupta & Schlichting (2019) and Owen & Wu (2017) for their respective models. However, if it is found that these assumptions are poor reflections of reality, the results obtained here may need to be re-examined.

Another potential inaccuracy is the stellar saturation time assumed in the photoevaporation model and how the stellar X-ray/EUV output changes over time. We have used Owen & Wu (2017)'s saturation time of 100 Myr and the subsequent exponential decline in high-energy stellar output. However, recent work has shown that strong high-energy radiation may persist beyond this time, over Gyr timescales (King & Wheatley, 2021). If true, this could make it more difficult to distinguish between photoevaporation and core-powered mass loss because the mass-loss timescales would be more similar.

There are also likely selection effects at work that we have not taken into account. For instance, it is more difficult to detect smaller planets around hotter stars because they produce a smaller transit depth. Since stellar temperature is an important factor in determining planetary radius through atmospheric mass loss, this could be biasing our results. This bias may be looked at in future work.

In this work, we have compared core-powered mass loss and photoevaporation because those are the two most popular theories for the origin of the radius valley. However, other ideas have also been proposed, such as that the valley is formed primordially during gas accretion (e.g. Lee & Connors 2021; Lee et al. 2022), created from the effects of planetary migration and resonant chain disruption (Izidoro et al., 2022), or shaped by stellar clustering (Kruijssen et al., 2020). These alternative explanations can be explored in future work using this framework, perhaps by describing each as a Nature hypothesis

and comparing them with photoevaporation and core-powered mass loss.

Acknowledgments

Computations for this research were performed on the Pennsylvania State University's Institute for Computational and Data Sciences' Roar supercomputer. This content is solely the responsibility of the authors and does not necessarily represent the views of the Institute for Computational and Data Sciences.

This research made use of the following software: SciPy (Virtanen et al., 2020), NumPy (Harris et al., 2020), Matplotlib (Hunter, 2007), Pandas (McKinney, 2010, 2011).

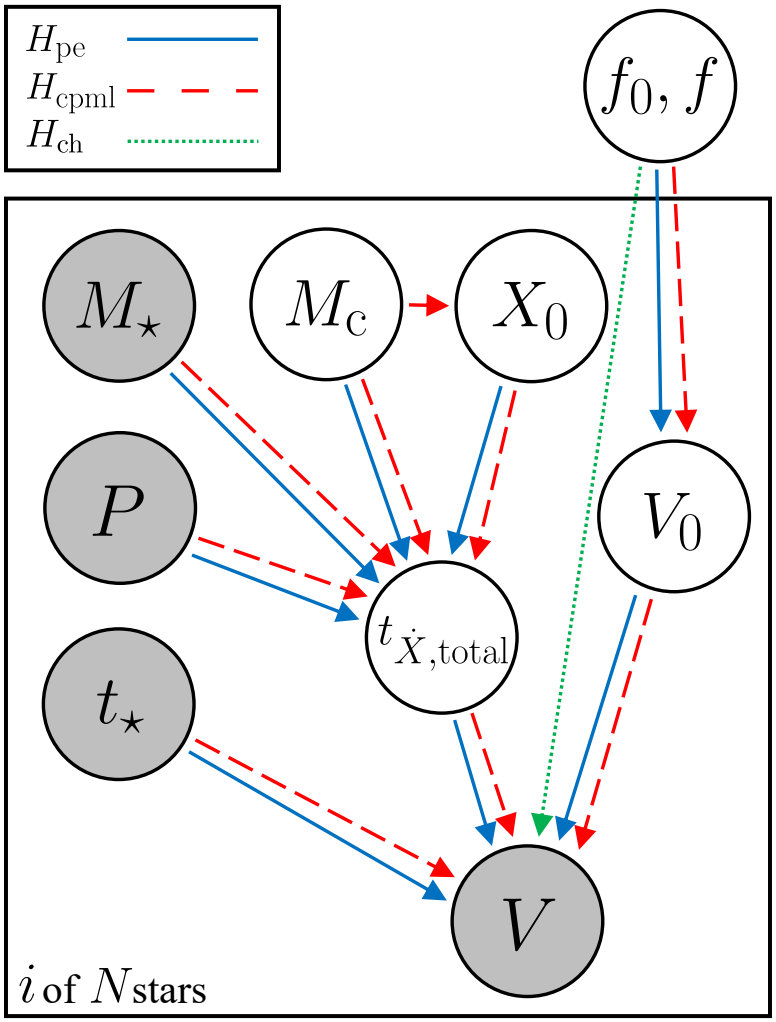

Figure 4.2. Graphical representation of our model, showing the relationships between parameters under different hypotheses. Relationships under the photoevaporation hypothesis are shown with a solid blue arrow, relationships under the core-powered mass loss hypothesis are shown with a dashed red arrow, and those under the Chance hypothesis are shown with a dotted green arrow. Gray circles represent observed parameters: the radius state V (indicating whether a planet is above or below the radius valley), the stellar age $t_\star$, the planetary orbital period P, and the stellar mass $M_\star$. White circles represent unobserved individual system parameters (on the plate) – the total mass-loss time $t_{\dot{X},\rm total}$, the initial radius state V_0, the planetary core mass $M_{\rm c}$, and the initial atmospheric mass fraction X_0 – and hyperparameters – the fraction of small, close-in planets that start out as sub-Neptunes f_0, and the fraction of small, close-in planets observed to be sub-Neptunes f. We put f_0 (relevant for both mass-loss hypotheses) and f (relevant for the Chance hypothesis) in the same circle because, mathematically, they behave the same way under each hypothesis. The "i of N stars" is to indicate that the plate is iterated over each of the N planets in the sample.

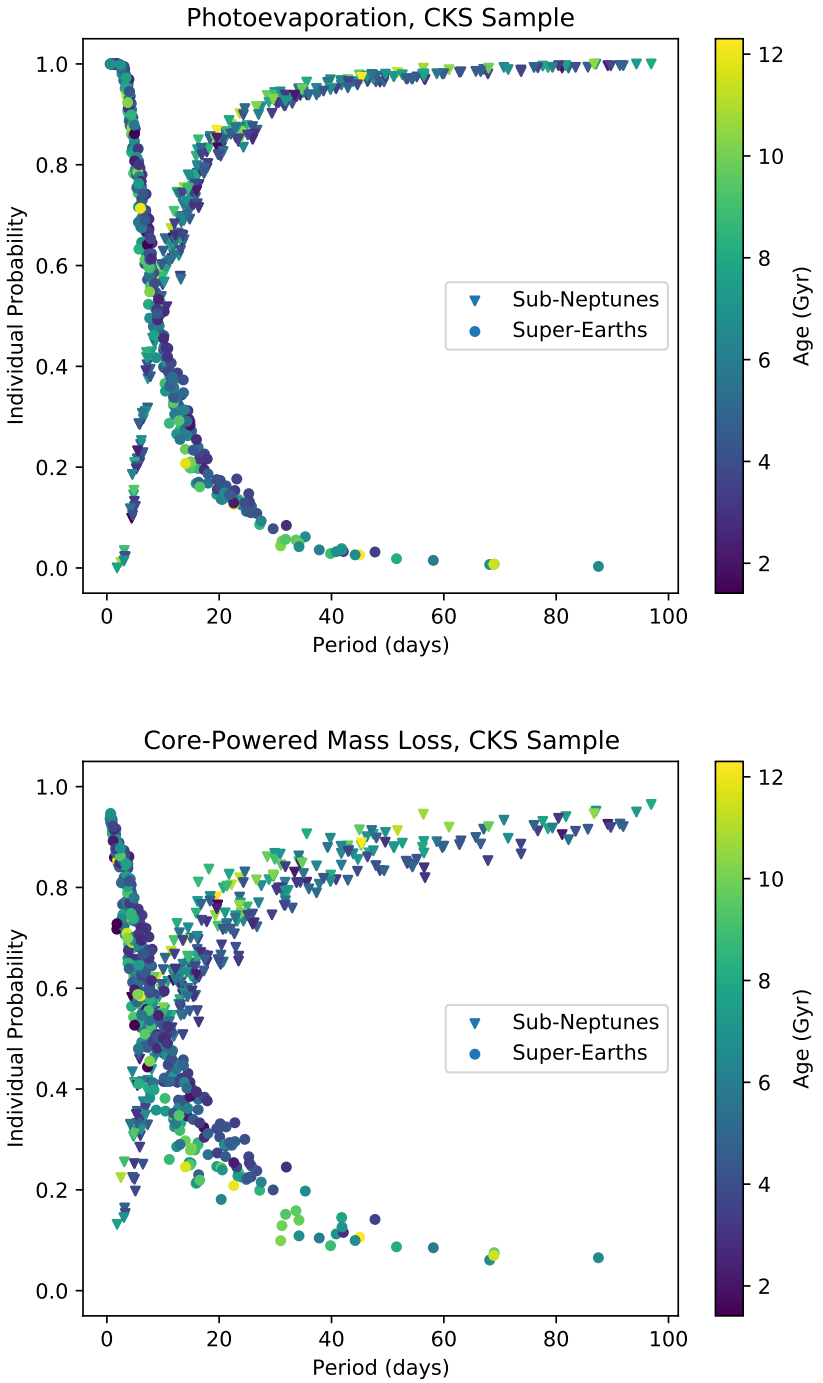

Figure 4.3. Individual likelihood as a function of orbital period for planets in the CKS sample under the original photoevaporation (top) and core-powered mass loss (bottom) hypotheses, with the initial fraction of sub-Neptunes $f_0 = 1$. Planets classified as sub-Neptunes are shown as triangles, and those classified as super-Earths are shown as circles. Markers are colored according to stellar age.

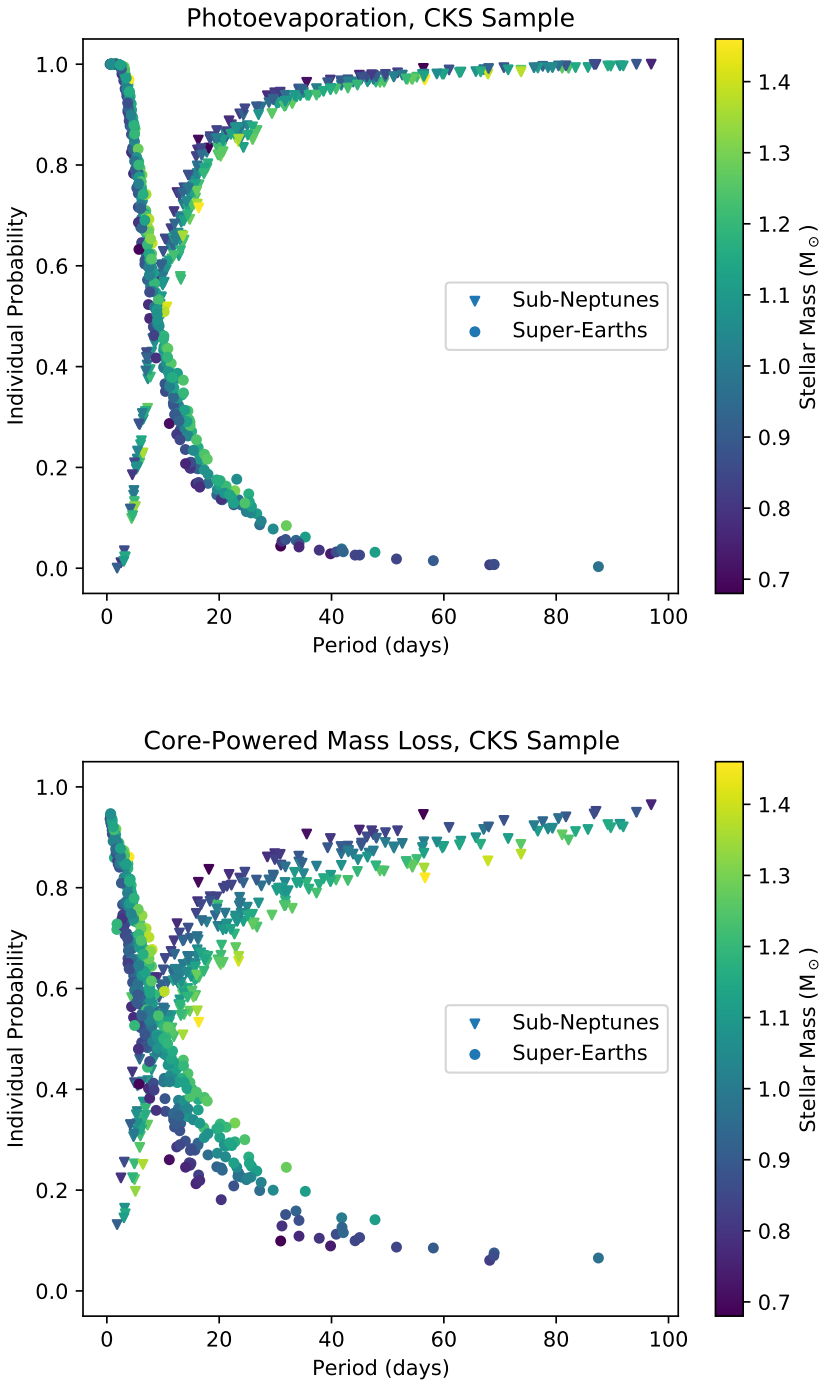

Figure 4.4. Same as Figure 4.3 but colored according to stellar mass.

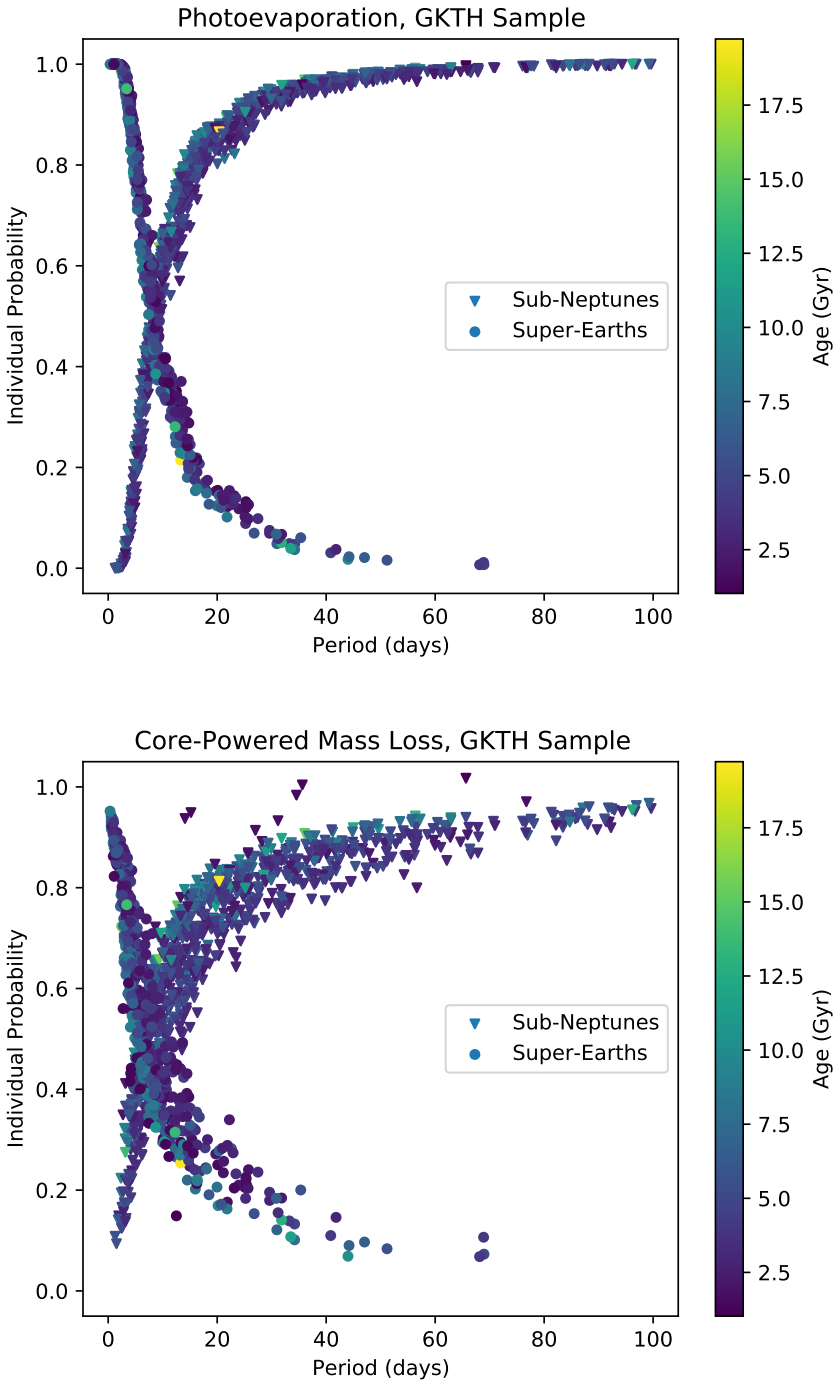

Figure 4.5. Same as Figure 4.3 but for the GKTH sample.

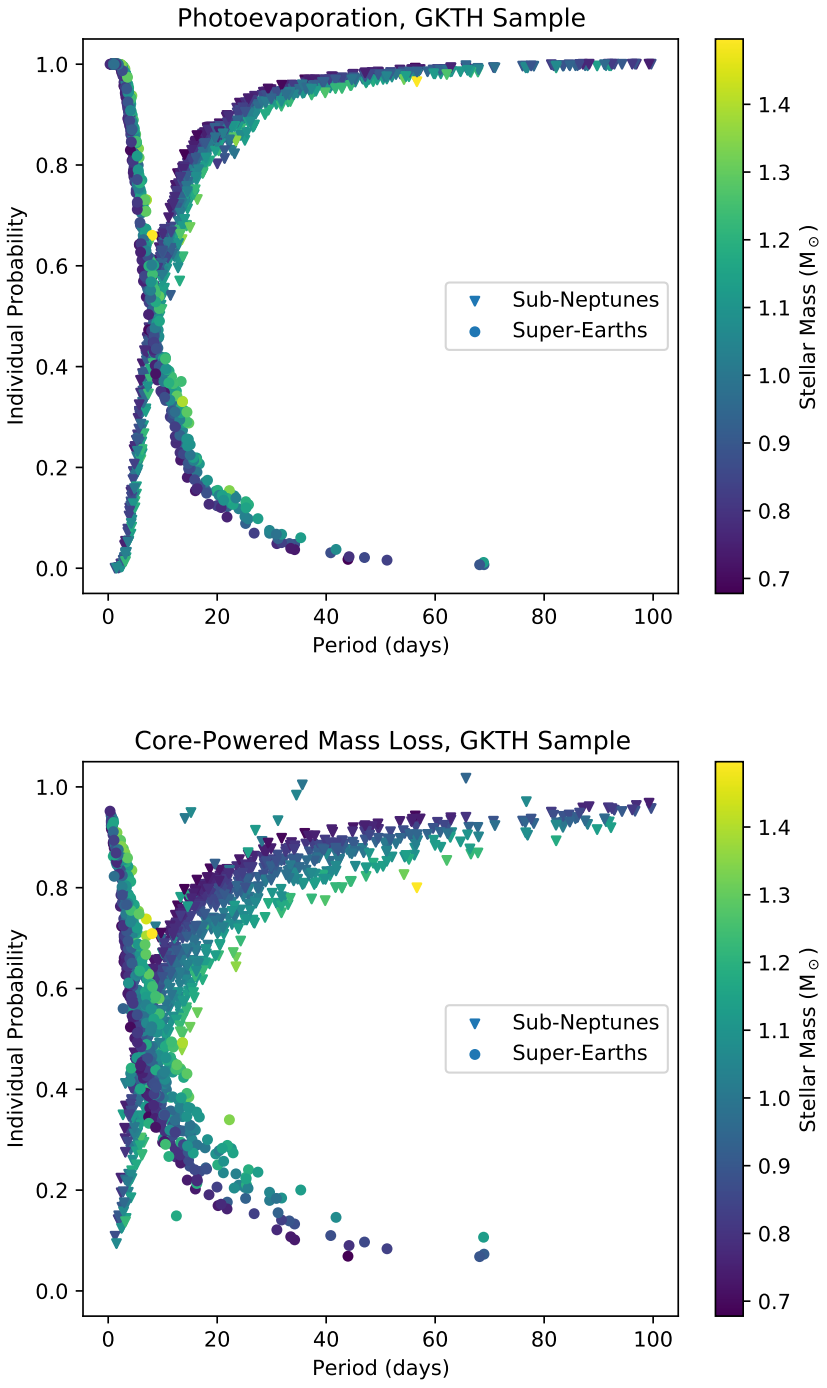

Figure 4.6. Same as Figure 4.5 but colored according to stellar mass.

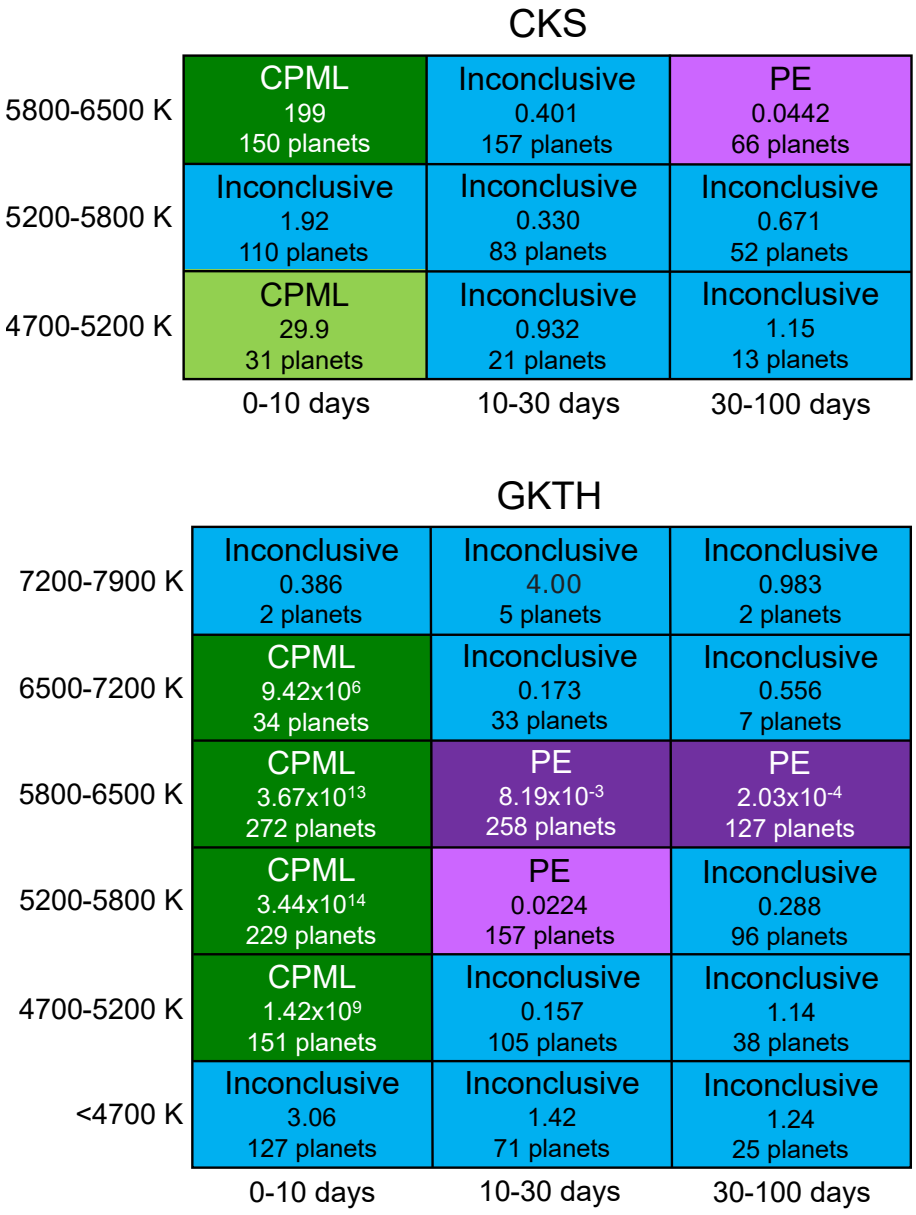

Figure 4.7. Results of computing odds ratios in different period and stellar temperature bins for the CKS sample (top) and the GKTH sample (bottom). Each bin contains the conclusion drawn from the odds ratio and is colored accordingly: photoevaporation (PE; dark purple if strongly favored, light purple if moderately favored), core-powered mass loss (CPML; dark green if strongly favored, light green if moderately favored), or inconclusive (blue). The $p(H_{\rm cpml})/p(H_{\rm pe})$ odds ratio is also listed, along with the number of planets in each bin.

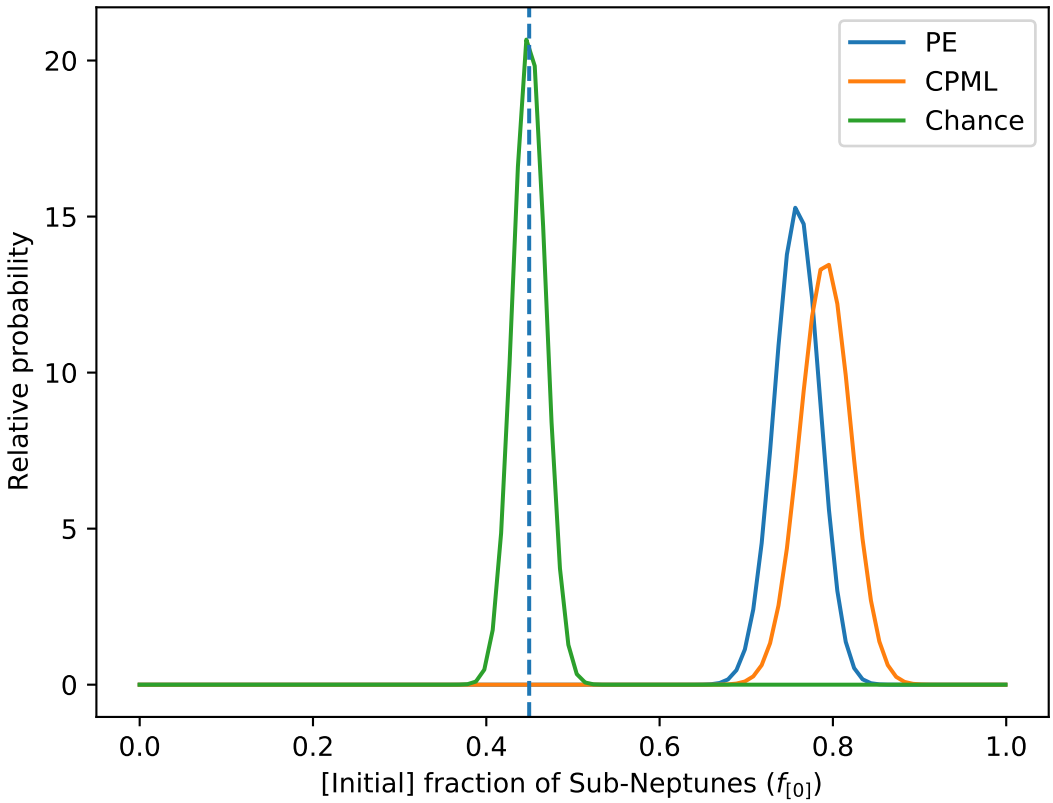

Figure 4.8. Posterior histograms of the initial fraction of close-in sub-Neptunes f_0, or, in the case of the Chance hypothesis f, the overall close-in fraction of sub-Neptunes, under each hypothesis for the CKS sample. The observed sub-Neptune fraction is shown as a dashed line. For photoevaporation and core-powered mass loss, we show the f_0 posterior for just the original calculations. The curves have been normalized to have the same area.

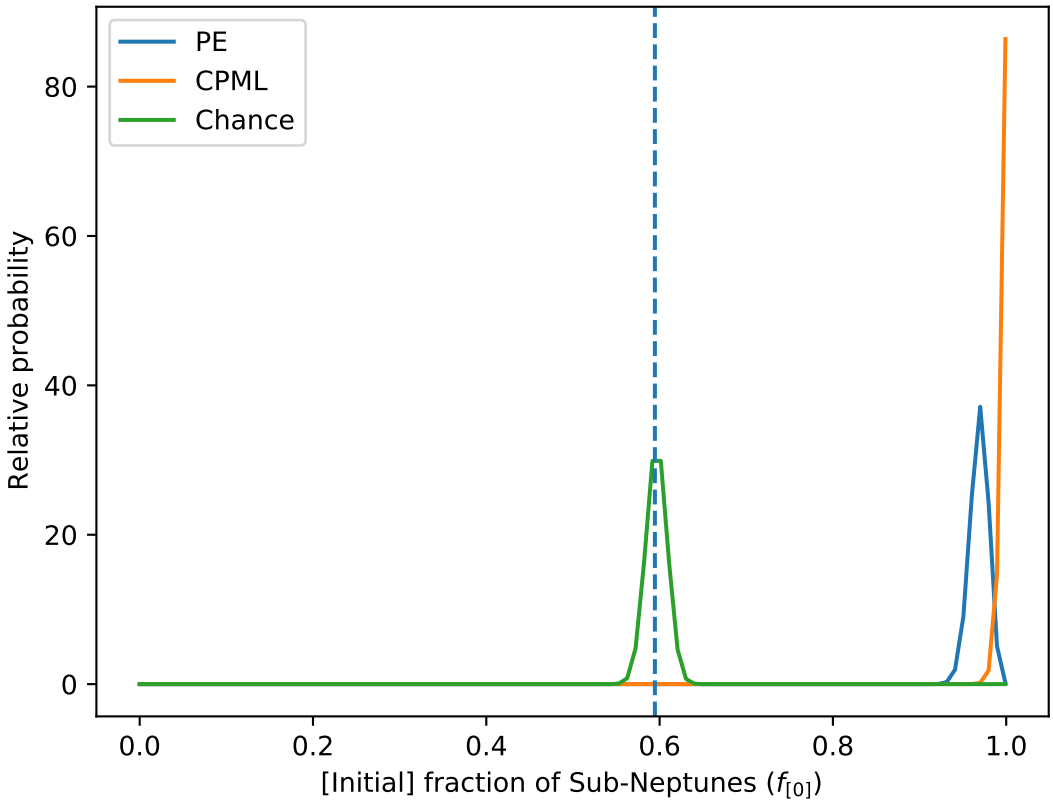

Figure 4.9. Same as Figure 4.8 but for the GKTH sample.

Chapter 5
Conclusion

In this work, we have developed a method to help understand the causes of observed trends of planetary properties with other system parameters. We can use the available data to compute the evidence for a given hypothesis, representing a possible source of an observed trend. We can then use an odds ratio to compare the evidence for two competing hypotheses, letting us know which one the data better supports. We have applied this statistical framework to several trends proposed in the literature.

The formation and stability of orbital resonances is still an open question. Determining the initial frequency of 2:1 resonances will help us better understand planet formation processes, while a knowledge of how that frequency changes with age will help us understand the long-term stability of planetary systems. We were not able to draw a firm conclusion about whether 2:1 orbital resonances get disrupted over time. Part of the reason for this is the wide range of possible resonance disruption timescales, which leads us to use wide, uninformative priors for timescale parameters. With such a large possible parameter space, the available data is insufficient for robustly detecting most possible age trends. A larger dataset of 2:1 resonant systems that span a wider age range may eventually be able to resolve this question in the future.

We have shown that the data on stellar obliquities of hot Jupiter hosts better support a trend due to stellar effective temperature rather than age. We reached this conclusion using two different samples and regardless of whether or not we include measurement uncertainties. This trend suggests that different misaligning mechanisms operate around stars of different temperatures. Alternatively, it could indicate that whatever process realigns stars with planetary orbits primarily occurs in cooler stars over very short timescales.

The formation of hot Jupiters has been a topic of much study since the early days of exoplanet discoveries, and the eccentricity distribution of these planets provides important

clues. We have shown that a trend of hot Jupiter eccentricities due to stellar age, under a tidal circularization model, is strongly preferred over a trend due to semimajor axis, showing that the orbits circularize over time. This supports high-eccentricity migration as a dominant formation mechanism for hot Jupiters. This conclusion is also robust against accounting for measurement uncertainties.

Finally, we used our framework to analyze the radius valley of super-Earths and sub-Neptunes. We compared the evidence for photoevaporation versus core-powered mass loss as the primary sculptor of the valley using two different datsets. Though the results with the CKS data are dependent on the assumptions we use for core mass and initial atmospheric mass fraction, the GKTH data more robustly support core-powered mass loss over photoevaporation. The GKTH data only favor photoevaporation in a few variations of the calculations when we include hot stars in the sample, suggesting that assumptions for initial atmospheric mass fraction and core mass may have different validity around stars of different temperatures, or possibly that photoevaporation may become more important around hotter stars. Both mass-loss hypotheses are very strongly favored over a chance relation in every variation to our calculations, supporting the existence of an age trend in the numbers of super-Earths and sub-Neptunes.

The strongly supportive odds ratios we have obtained in this work do not definitively determine a hypothesis as the absolute best descriptor of the data. Rather, they say which one is better out of two hypotheses of interest. If another trend is observed or another model proposed, the odds ratios can be calculated with the new model to see if it does a better job of describing the data than the previously most-favored hypothesis. In the radius valley case, for example, we have only considered core-powered mass loss and photoevaporation, so we can only say how those hypotheses compare with each other and cannot rule out other mechanisms. In future work, we can test other theories, such as the primordial formation of the radius valley, and compare them with core-powered mass loss and photoevaporation.

The ever-increasing set of known and well-characterized exoplanets will provide better samples with which to test these and other age trends. Additionally, a better understanding of the processes proposed to shape planetary formation and evolution will help in the odds ratio calculations, because our results are also only valid insofar as the assumptions we have made are correct. In the future, it may be worthwhile to revisit some of the trends we have analyzed here – particularly 2:1 resonances – with an improved dataset. We can also use our framework to examine other trends that may appear. Additionally, this framework could be used in designing future surveys. If a

trend is suspected or predicted, simulated planetary systems could be used to determine what sort of dataset would be needed to detect it with a strong odds ratio, if the trend truly exists. This could provide useful information on not just sample size, but also the requisite measurement precision and type of stars or planets that would need to be observed.

Bibliography

Adams, F. C., & Laughlin, G. 2006, ApJ, 649, 1004, doi: 10.1086/506145

Albrecht, S., Winn, J. N., Johnson, J. A., et al. 2012, ApJ, 757, 18, doi: 10.1088/0004-637X/757/1/18

Albrecht, S. H., Dawson, R. I., & Winn, J. N. 2022, PASP, 134, 082001, doi: 10.1088/1538-3873/ac6c09

Arakaki, T., Bolewski, J., Deits, R., et al. 2020, JuliaPy/pyjulia: PyJulia v0.5.6, v0.5.6, Zenodo, doi: 10.5281/zenodo.4294939

Ballard, S., & Johnson, J. A. 2016, ApJ, 816, 66, doi: 10.3847/0004-637X/816/2/66

Baraffe, I., Selsis, F., Chabrier, G., et al. 2004, A&A, 419, L13, doi: 10.1051/0004-6361:20040129

Batygin, K., Bodenheimer, P. H., & Laughlin, G. P. 2016, ApJ, 829, 114, doi: 10.3847/0004-637X/829/2/114

Beck, J. G., & Giles, P. 2005, ApJ, 621, L153, doi: 10.1086/429224

Behnel, S., Bradshaw, R., Citro, C., et al. 2011, Computing in Science & Engineering, 13, 31

Berger, T. A., Huber, D., Gaidos, E., & van Saders, J. L. 2018, ApJ, 866, 99, doi: 10.3847/1538-4357/aada83

Berger, T. A., Huber, D., Gaidos, E., van Saders, J. L., & Weiss, L. M. 2020a, AJ, 160, 108, doi: 10.3847/1538-3881/aba18a

Berger, T. A., Huber, D., van Saders, J. L., et al. 2020b, AJ, 159, 280, doi: 10.3847/1538-3881/159/6/280

Berger, T. A., Schlieder, J. E., & Huber, D. 2023a, arXiv e-prints, arXiv:2301.11338, doi: 10.48550/arXiv.2301.11338

Berger, T. A., Schlieder, J. E., Huber, D., & Barclay, T. 2023b, arXiv e-prints, arXiv:2302.00009, doi: 10.48550/arXiv.2302.00009

Bezanson, J., Edelman, A., Karpinski, S., & Shah, V. B. 2017, SIAM review, 59, 65. https://doi.org/10.1137/141000671

Boley, A. C., Granados Contreras, A. P., & Gladman, B. 2016, ApJ, 817, L17, doi: 10.3847/2041-8205/817/2/L17

Borucki, W. J., Koch, D., Basri, G., et al. 2010, Science, 327, 977, doi: 10.1126/science.1185402

Buchhave, L. A., Bizzarro, M., Latham, D. W., et al. 2014, Nature, 509, 593, doi: 10.1038/nature13254

Chen, H., & Rogers, L. A. 2016, ApJ, 831, 180, doi: 10.3847/0004-637X/831/2/180

Christiansen, J., Beichman, C., Ciardi, D. R., & Huber, D. 2019a, BAAS, 51, 312. https://arxiv.org/abs/1903.09110

Christiansen, J. L., Beichman, C., Ciardi, D. R., Huber, D., & Marley, M. S. 2019b, arXiv e-prints, arXiv:1903.09110. https://arxiv.org/abs/1903.09110

David, T. J., Contardo, G., Sandoval, A., et al. 2021, AJ, 161, 265, doi: 10.3847/1538-3881/abf439

Dawson, R. I., Chiang, E., & Lee, E. J. 2015, MNRAS, 453, 1471, doi: 10.1093/mnras/stv1639

Dawson, R. I., & Johnson, J. A. 2018, ARA&A, 56, 175, doi: 10.1146/annurev-astro-081817-051853

Dawson, R. I., & Murray-Clay, R. A. 2013, ApJ, 767, L24, doi: 10.1088/2041-8205/767/2/L24

Dong, R., & Dawson, R. 2016, ApJ, 825, 77, doi: 10.3847/0004-637X/825/1/77

Duffell, P. C., & Chiang, E. 2015, ApJ, 812, 94, doi: 10.1088/0004-637X/812/2/94

Fischer, D. A., & Valenti, J. 2005, ApJ, 622, 1102, doi: 10.1086/428383

Fulton, B. J., & Petigura, E. A. 2018, AJ, 156, 264, doi: 10.3847/1538-3881/aae828

Fulton, B. J., Petigura, E. A., Howard, A. W., et al. 2017, AJ, 154, 109, doi: 10.3847/1538-3881/aa80eb

Furlan, E., Ciardi, D. R., Cochran, W. D., et al. 2018, ApJ, 861, 149, doi: 10.3847/1538-4357/aaca34

Gaia Collaboration, Prusti, T., de Bruijne, J. H. J., et al. 2016, A&A, 595, A1, doi: 10.1051/0004-6361/201629272

Genz, A., & Malik, A. 1980, Journal of Computational and Applied Mathematics, 6, 295, doi: https://doi.org/10.1016/0771-050X(80)90039-X

Ginzburg, S., Schlichting, H. E., & Sari, R. 2016, ApJ, 825, 29, doi: 10.3847/0004-637X/825/1/29

—. 2018, MNRAS, 476, 759, doi: 10.1093/mnras/sty290

Goldreich, P., & Schlichting, H. E. 2014, AJ, 147, 32, doi: 10.1088/0004-6256/147/2/32

Goldreich, P., & Tremaine, S. 1980, ApJ, 241, 425, doi: 10.1086/158356

Gomes, R., Deienno, R., & Morbidelli, A. 2017, AJ, 153, 27, doi: 10.3847/1538-3881/153/1/27

Gupta, A., & Schlichting, H. E. 2019, MNRAS, 487, 24, doi: 10.1093/mnras/stz1230

—. 2020, MNRAS, 493, 792, doi: 10.1093/mnras/staa315

Harris, C. R., Millman, K. J., van der Walt, S. J., et al. 2020, Nature, 585, 357, doi: 10.1038/s41586-020-2649-2

Hébrard, G., Ehrenreich, D., Bouchy, F., et al. 2011, A&A, 527, L11, doi: 10.1051/0004-6361/201016331

Howard, A. W., Marcy, G. W., Johnson, J. A., et al. 2010, Science, 330, 653, doi: 10.1126/science.1194854

Hunter, J. D. 2007, Computing In Science & Engineering, 9, 90

Izidoro, A., Ogihara, M., Raymond, S. N., et al. 2017, MNRAS, 470, 1750, doi: 10.1093/mnras/stx1232

Izidoro, A., Schlichting, H. E., Isella, A., et al. 2022, ApJ, 939, L19, doi: 10.3847/2041-8213/ac990d

Jackson, A. P., Davis, T. A., & Wheatley, P. J. 2012, MNRAS, 422, 2024, doi: 10.1111/j.1365-2966.2012.20657.x

Jackson, B., Greenberg, R., & Barnes, R. 2008, ApJ, 678, 1396, doi: 10.1086/529187

Jeffreys, H. 1961, Theory of probability, 3rd edn. (Oxford: Clarendon Press)

Jin, S., Mordasini, C., Parmentier, V., et al. 2014, ApJ, 795, 65, doi: 10.1088/0004-637X/795/1/65

Johnson, J. A., Winn, J. N., Bakos, G. Á., et al. 2011, ApJ, 735, 24, doi: 10.1088/0004-637X/735/1/24

Johnson, J. A., Petigura, E. A., Fulton, B. J., et al. 2017, AJ, 154, 108, doi: 10.3847/1538-3881/aa80e7

Jørgensen, B. R., & Lindegren, L. 2005, A&A, 436, 127, doi: 10.1051/0004-6361:20042185

Kass, R. E., & Raftery, A. E. 1995, Journal of the American Statistical Association, 90, 773. http://www.jstor.org/stable/2291091

King, G. W., & Wheatley, P. J. 2021, MNRAS, 501, L28, doi: 10.1093/mnrasl/slaa186

Koriski, S., & Zucker, S. 2011, ApJ, 741, L23, doi: 10.1088/2041-8205/741/1/L23

Kraft, R. P. 1967, ApJ, 150, 551, doi: 10.1086/149359

Kruijssen, J. M. D., Longmore, S. N., & Chevance, M. 2020, ApJ, 905, L18, doi: 10.3847/2041-8213/abccc3

Lammer, H., Selsis, F., Ribas, I., et al. 2003, ApJ, 598, L121, doi: 10.1086/380815

Lee, E. J., & Connors, N. J. 2021, ApJ, 908, 32, doi: 10.3847/1538-4357/abd6c7

Lee, E. J., Karalis, A., & Thorngren, D. P. 2022, ApJ, 941, 186, doi: 10.3847/1538-4357/ac9c66

Lee, M. H., & Peale, S. J. 2002, ApJ, 567, 596, doi: 10.1086/338504

Lin, D. N. C., & Papaloizou, J. 1986, ApJ, 309, 846, doi: 10.1086/164653

Lopez, E. D., & Fortney, J. J. 2013, ApJ, 776, 2, doi: 10.1088/0004-637X/776/1/2

MacDonald, M. G., & Dawson, R. I. 2018, AJ, 156, 228, doi: 10.3847/1538-3881/aae266

Malhotra, R. 1993, Nature, 365, 819, doi: 10.1038/365819a0

—. 2012, EOLSS, 6.119.55

Mamajek, E. E., & Hillenbrand, L. A. 2008, ApJ, 687, 1264, doi: 10.1086/591785

Marcy, G. W., Isaacson, H., Howard, A. W., et al. 2014, ApJS, 210, 20, doi: 10.1088/0067-0049/210/2/20

Martinez, C. F., Cunha, K., Ghezzi, L., & Smith, V. V. 2019, ApJ, 875, 29, doi: 10.3847/1538-4357/ab0d93

Mayor, M., & Queloz, D. 1995, Nature, 378, 355, doi: 10.1038/378355a0

Mayor, M., Marmier, M., Lovis, C., et al. 2011, arXiv e-prints, arXiv:1109.2497, doi: 10.48550/arXiv.1109.2497

McKinney, W. 2010, in Proceedings of the 9th Python in Science Conference, Vol. 445, Austin, TX, 51–56

McKinney, W. 2011, Python for High Performance and Scientific Computing, 14

Morton, T. D. 2015, isochrones: Stellar model grid package. http://ascl.net/1503.010

Murray-Clay, R. A., Chiang, E. I., & Murray, N. 2009, ApJ, 693, 23, doi: 10.1088/0004-637X/693/1/23

NASA Exoplanet Archive. 2021a, Planetary Systems, Version: 2021-08-26 12:07, NExScI-Caltech/IPAC, doi: 10.26133/NEA12

—. 2021b, Planetary Systems, Version: 2021-11-12 13:11, NExScI-Caltech/IPAC, doi: 10.26133/NEA12

Ogilvie, G. I., & Lin, D. N. C. 2004, ApJ, 610, 477, doi: 10.1086/421454

Owen, J. E., & Jackson, A. P. 2012, MNRAS, 425, 2931, doi: 10.1111/j.1365-2966.2012.21481.x

Owen, J. E., & Wu, Y. 2013, ApJ, 775, 105, doi: 10.1088/0004-637X/775/2/105

—. 2016, ApJ, 817, 107, doi: 10.3847/0004-637X/817/2/107

—. 2017, ApJ, 847, 29, doi: 10.3847/1538-4357/aa890a

Petigura, E. A., Howard, A. W., Marcy, G. W., et al. 2017, AJ, 154, 107, doi: 10.3847/1538-3881/aa80de

Petigura, E. A., Rogers, J. G., Isaacson, H., et al. 2022, AJ, 163, 179, doi: 10.3847/1538-3881/ac51e3

Petrovich, C., Tremaine, S., & Rafikov, R. 2014, ApJ, 786, 101, doi: 10.1088/0004-637X/786/2/101

Pont, F., & Eyer, L. 2004, MNRAS, 351, 487, doi: 10.1111/j.1365-2966.2004.07780.x

Pu, B., & Wu, Y. 2015, ApJ, 807, 44, doi: 10.1088/0004-637X/807/1/44

Quinn, S. N., White, R. J., Latham, D. W., et al. 2014, ApJ, 787, 27, doi: 10.1088/0004-637X/787/1/27

Rasio, F. A., & Ford, E. B. 1996, Science, 274, 954, doi: 10.1126/science.274.5289.954

Rogers, J. G., Gupta, A., Owen, J. E., & Schlichting, H. E. 2021, MNRAS, 508, 5886, doi: 10.1093/mnras/stab2897

Rogers, J. G., & Owen, J. E. 2021, MNRAS, 503, 1526, doi: 10.1093/mnras/stab529

Safsten, E. D., & Dawson, R. I. 2022, AJ, 163, 188, doi: 10.3847/1538-3881/ac573a

Safsten, E. D., Dawson, R. I., & Wolfgang, A. 2020, AJ, 160, 214, doi: 10.3847/1538-3881/abb536

Sandoval, A., Contardo, G., & David, T. J. 2021, ApJ, 911, 117, doi: 10.3847/1538-4357/abea9e

Schlaufman, K. C. 2010, ApJ, 719, 602, doi: 10.1088/0004-637X/719/1/602

Schneider, J., Dedieu, C., Le Sidaner, P., Savalle, R., & Zolotukhin, I. 2011a, A&A, 532, A79, doi: 10.1051/0004-6361/201116713

—. 2011b, A&A, 532, A79, doi: 10.1051/0004-6361/201116713

Skumanich, A. 1972, ApJ, 171, 565, doi: 10.1086/151310

Socrates, A., Katz, B., & Dong, S. 2012, arXiv e-prints, arXiv:1209.5724. https://arxiv.org/abs/1209.5724

Soderblom, D. R. 2010, ARA&A, 48, 581, doi: 10.1146/annurev-astro-081309-130806

Southworth, J. 2011, MNRAS, 417, 2166, doi: 10.1111/j.1365-2966.2011.19399.x

Takeda, G., Ford, E. B., Sills, A., et al. 2007, ApJS, 168, 297, doi: 10.1086/509763

Thommes, E. W., Bryden, G., Wu, Y., & Rasio, F. A. 2008, ApJ, 675, 1538, doi: 10.1086/525244

Triaud, A. H. M. J. 2011, A&A, 534, L6, doi: 10.1051/0004-6361/201117713

Van Eylen, V., Agentoft, C., Lundkvist, M. S., et al. 2018, MNRAS, 479, 4786, doi: 10.1093/mnras/sty1783

Veras, D., Brown, D. J. A., Mustill, A. J., & Pollacco, D. 2015, MNRAS, 453, 67, doi: 10.1093/mnras/stv1615

Virtanen, P., Gommers, R., Oliphant, T. E., et al. 2020, Nature Methods, 17, 261, doi: https://doi.org/10.1038/s41592-019-0686-2

Wang, J., & Fischer, D. A. 2015, AJ, 149, 14, doi: 10.1088/0004-6256/149/1/14

Weiss, L. M., Marcy, G. W., Rowe, J. F., et al. 2013, ApJ, 768, 14, doi: 10.1088/0004-637X/768/1/14

Winn, J. N., Fabrycky, D., Albrecht, S., & Johnson, J. A. 2010, ApJ, 718, L145, doi: 10.1088/2041-8205/718/2/L145

Winn, J. N., & Fabrycky, D. C. 2015, ARA&A, 53, 409, doi: 10.1146/annurev-astro-082214-122246

Wolszczan, A., & Frail, D. A. 1992, Nature, 355, 145, doi: 10.1038/355145a0

Wu, Y. 2019, ApJ, 874, 91, doi: 10.3847/1538-4357/ab06f8

Wyatt, M. C., Kral, Q., & Sinclair, C. A. 2020, MNRAS, 491, 782, doi: 10.1093/mnras/stz3052

Yoder, C. F. 1979, Nature, 279, 767, doi: 10.1038/279767a0

Yoder, C. F., & Peale, S. J. 1981, Icarus, 47, 1, doi: 10.1016/0019-1035(81)90088-9

Vita

Emily Safsten

Education

- Ph.D. in Astronomy & Astrophysics – Pennsylvania State University – 2023 (anticipated)
- M.S. in Physics – Brigham Young University – 2017
- B.S. in Physics-Astronomy – Brigham Young University – 2014

Refereed Publications

1. Safsten, E. D. and Dawson, R. I., "Comparing Core-Powered Mass Loss and Photoevaporation as the Primary Sculptor of the Radius Valley with a Bayesian Statistical Framework", *in preparation.*
2. Safsten, E. D. and Dawson, R. I., "Nature versus Nurture: Investigating the Effects of Measurement Uncertainties in the Assessment of Potential Trends between Planetary and Stellar Properties", 2022, AJ, 163, 4.
3. Safsten, E. D., Dawson, R. I., and Wolfgang, A., "Nature Versus Nurture: A Bayesian Framework for Assessing Apparent Correlations between Planetary Orbital Properties and Stellar Ages", 2020, AJ, 160, 5.
4. Safsten, E. D., Lara, P., Joner, M. D., Stephens, D. C., and Rawlins, J., "A new contact eclipsing binary in the field of KOI 1152", 2015, IBVS, 6147, 1.